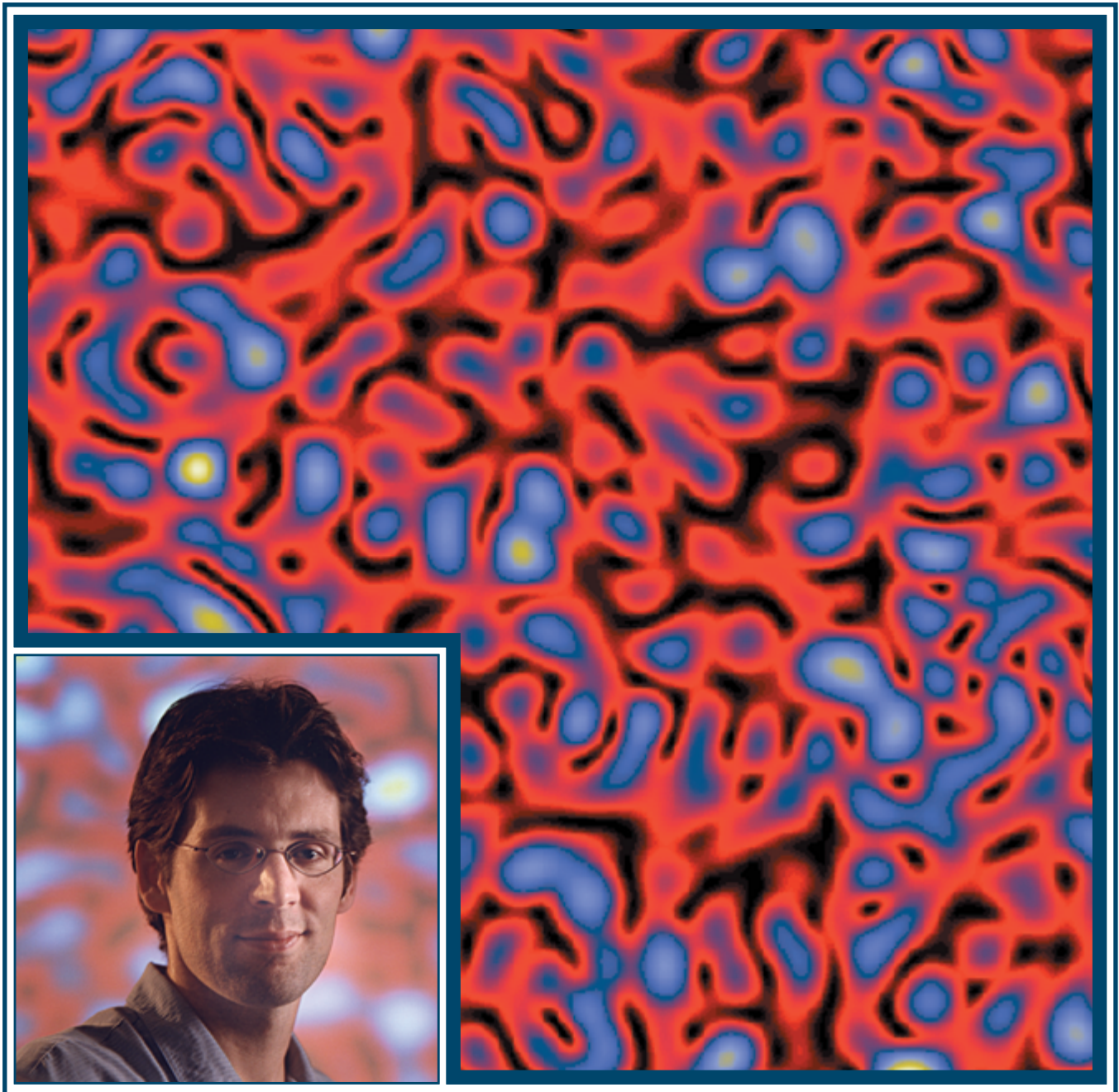


LLE Review

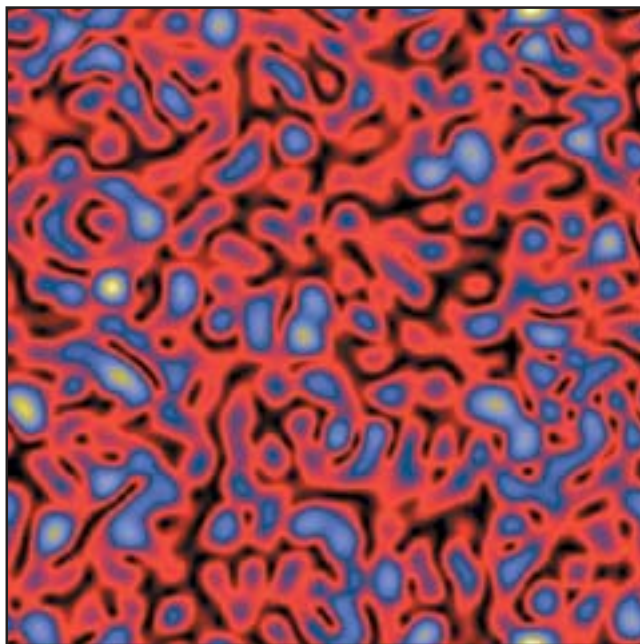


Quarterly Report



About the Cover:

The cover photo shows an image of the laser electric-field intensity taken from the parallel, three-dimensional, laser-plasma interaction (LPI) code pF3D. The pF3D code was developed by Lawrence Livermore National Laboratory (LLNL) primarily for modeling LPI in hohlraum plasmas. The article entitled "Modeling Laser-Plasma Interaction Physics Under Direct-Drive Inertial Confinement Fusion Conditions" (p. 93) describes how scientists at LLE, including Scientist Jason Myatt (shown in the inset), are adapting pF3D for use in direct-drive conditions.



The electric-field intensity shown in the figure displays the characteristic speckle pattern in the transverse plane to the laser axis as a result of beam smoothing using distributed phase plates (DPP's). In the statistical distribution of electric-field maxima, there are individual maxima (or "hot spots") that can exceed the average incident intensity by several times. Laser-driven parametric scattering instabilities such as stimulated Brillouin scattering (SBS) or decay instabilities like the two-plasmon decay (TPD) are preferentially driven in these hot spots due to the elevated light intensities.

This report was prepared as an account of work conducted by the Laboratory for Laser Energetics and sponsored by New York State Energy Research and Development Authority, the University of Rochester, the U.S. Department of Energy, and other agencies. Neither the above named sponsors, nor any of their employees, makes any warranty, expressed or implied, or assumes any legal liability or responsibility for the accuracy, completeness, or usefulness of any information, apparatus, product, or process disclosed, or represents that its use would not infringe privately owned rights. Reference herein to any specific commercial product, process, or service by trade name, mark, manufacturer, or otherwise, does not necessarily constitute or imply its endorsement, recommendation, or favoring by

the United States Government or any agency thereof or any other sponsor. Results reported in the LLE Review should not be taken as necessarily final results as they represent active research. The views and opinions of authors expressed herein do not necessarily state or reflect those of any of the above sponsoring entities.

The work described in this volume includes current research at the Laboratory for Laser Energetics, which is supported by New York State Energy Research and Development Authority, the University of Rochester, the U.S. Department of Energy Office of Inertial Confinement Fusion under Cooperative Agreement No. DE-FC03-92SF19460, and other agencies.

Printed in the United States of America
Available from
National Technical Information Services
U.S. Department of Commerce
5285 Port Royal Road
Springfield, VA 22161

For questions or comments, contact Timothy J. B. Collins, *Editor*, Laboratory for Laser Energetics, 250 East River Road, Rochester, NY 14623-1299, (585) 275-8245.

Price codes: Printed Copy A04
Microfiche A01

Worldwide-Web Home Page: <http://www.lle.rochester.edu/>

LLE Review



Quarterly Report

Contents

In Brief	iii
Modeling Laser–Plasma Interaction Physics Under Direct-Drive Inertial Confinement Fusion Conditions	93
Highly Stable, Diode-Pumped, Cavity-Dumped Nd:YLF Regenerative Amplifier for the OMEGA Laser Fusion Facility	103
Improved Performance of Direct-Drive Implosions with a Laser-Shaped Adiabatic	108
Direct-Drive Implosion Experiments with Enhanced Beam Balance on OMEGA	116
Effects of Textures on Hydrogen Diffusion in Nickel	125
Superconducting Properties of MgB ₂ Thin Films Prepared on Flexible Plastic Substrates	130
Time-Resolved Areal-Density Measurements with Proton Spectroscopy in Spherical Implosions	133
Multipolar Interband Absorption in a Semiconductor Quantum Dot: Electric Quadrupole Enhancement	139
Publications and Conference Presentations	

In Brief

This volume of the LLE Review, covering the period April–June 2002, features “Modeling Laser–Plasma Interaction Physics Under Direct-Drive Inertial Confinement Fusion Conditions” by J. Myatt, A. V. Maximov, and R. W. Short (p. 93). They report on pF3D, a parallel, three-dimensional laser–plasma interaction (LPI) code developed at LLNL for modeling indirect-drive plasmas, which recently has been modified for use under direct-drive conditions. Unlike indirect drive, modeling direct drive requires simulation of inhomogeneous supersonic flows and density profiles that include a critical surface. The treatment of the critical surface is particularly problematic in codes employing the paraxial approximation for the light waves. Myatt *et al.* describe the first results of the modified code: realistic simulations motivated by long-scale-length exploding-foil experiments conducted on LLE’s 30-kJ, 351-nm, 60-beam OMEGA laser system and intended to represent future NIF direct-drive conditions.

Additional highlights of research presented in this issue are

- A. V. Okishev, D. Battaglia, I. A. Begishev, and J. D. Zuegel (p. 103) have developed a new highly stable, diode-pumped, cavity-dumped, compact Nd:YLF regenerative amplifier (regen) of continuously shaped nanosecond pulses with a gain of $\sim 10^9$ for the front-end laser system of OMEGA. High output energy, long-term energy and temporal pulse shape stability, and high-quality beam profile have been demonstrated. Reliability, simplicity, modular design, and compactness are key features of this new diode-pumped regenerative amplifier.
- An experiment recently completed by J. P. Knauer and V. N. Goncharov (p. 108) has tested the ability of a direct-drive ICF laser pulse shape to vary the adiabat within a target shell. A picket pulse was added to a pulse shape designed to implode a cryogenic shell of D_2 with a ratio α of internal pressure to Fermi-degenerate pressure of 5. The effect of a picket is to strengthen the shock in the outer portion of the shell so that the ablation interface has a large α and the fuel maintains its $\alpha = 5$, resulting in increased stability and improved capsule performance.
- F. J. Marshall, J. A. Delettrez, R. L. Keck, J. H. Kelly, P. B. Radha, and L. J. Waxer (p. 116) describe implosion experiments with enhanced beam balance. Marshall *et al.* have implemented a new technique that determines the beam peak intensities at target chamber center on a full-power target shot by simultaneously measuring the x-ray flux produced by all 60 beams seen separated on a 4-mm-diam, Au-coated spherical target. Up to nine x-ray pinhole camera images are electronically recorded per shot from which beam-to-beam variations in peak intensity are determined, taking into account view angle and x-ray conversion efficiency. The observed variations are then used to correct the beam energies to produce a more-uniform irradiation. The authors present the results of implosion experiments with enhanced beam balance and comparisons to experiments with standard beam balance.
- W. T. Shmayda, Y. Cao, and J. A. Szpunar (p. 125) present the effects of textures on hydrogen diffusion in nickel. Deuterium and tritium— isotopes of hydrogen—are the primary fuels for inertial confinement fusion (ICF), so determining and controlling their rate of diffusion through containment materials are important to the design of ICF facilities. When polycrystalline metals have texture, the preferential orientation of the metals affects hydrogen absorption and diffusion. Hydrogen permeation results

show that there are significant differences among the three main textures of nickel membranes. Plating current density has a strong influence on texture development of nickel deposits. The texture of deposits can be easily manipulated by controlling plating conditions. In the experiments performed by Shmayda *et al.*, textured Ni membranes were prepared using electrodeposition, and the effects of fabrication on their diffusion rates were determined.

- A great deal of interest has been generated by the discovery of superconductivity in hexagonal magnesium borides not only because of MgB_2 's high critical temperature and current density but also its lower anisotropy, larger coherence length, and higher transparency of grain boundaries to current flow. R. Sobolewski, P. Kús, A. Plecenik, L. Satrapinsky, and Y. Xu (p. 130) have for the first time fabricated MgB_2 superconducting films on flexible substrates. They describe their process, by which these films could be deposited on large-area foils (up to 400 cm^2) and, after processing, cut into any shapes (e.g., stripes) with scissors or bent multiple times, without any observed degradation of their superconducting properties.
- V. A. Smalyuk, P. B. Radha, J. A. Delettrez, V. Yu. Glebov, V. N. Goncharov, D. D. Meyerhofer, S. P. Regan, S. Roberts, T. C. Sangster, J. M. Soures, and C. Stoeckl (p. 133) have inferred the growth of target areal density near peak compression in direct-drive spherical target implosions with 14.7-MeV deuterium–helium³ (D^3He) proton spectroscopy on the OMEGA laser system. The target areal density grows by a factor of ~ 8 during the time of neutron production ($\sim 400 \text{ ps}$) before reaching $123 \pm 16 \text{ mg cm}^{-2}$ at peak compression in an implosion of a $20\text{-}\mu\text{m}$ -thick plastic CH target filled with 4 atm of D^3He fuel.
- J. R. Zurita-Sanchez and L. Novotny (p. 139) have performed a theoretical investigation of a semiconductor quantum dot interacting with a strongly localized optical field, as encountered in high-resolution, near-field optical microscopy. The strong gradients of these localized fields suggest that higher-order multipolar interactions will affect the standard electric dipole transition rates and selection rules. For a semiconductor quantum dot in the strong confinement limit, Zurita-Sanchez and Novotny have calculated the interband electric quadrupole absorption rate and the associated selection rules, finding that the electric quadrupole absorption rate is comparable with the absorption rate calculated in the electric dipole approximation.

Timothy J. B. Collins
Editor

Modeling Laser–Plasma Interaction Physics Under Direct-Drive Inertial Confinement Fusion Conditions

Introduction

Laser–plasma interaction (LPI) processes taking place in indirect- and direct-drive targets differ significantly in several ways. Plasma electron densities n_e in hohlraum targets are typically a few percent of the critical density $n_c = m_e \omega_0^2 / 4\pi e^2$, so that the main instability mechanisms are stimulated Raman and stimulated Brillouin scattering (SRS and SBS, respectively), which typically have very large predicted linear gains due to the long scale lengths of near-uniform plasma.¹ The theoretical challenge here is to understand the nonlinear saturation mechanisms that are responsible for the small, observed reflectivities. In direct-drive targets the plasma is inhomogeneous, with the linear gain for parametric instabilities often limited by the inhomogeneity of the plasma, rather than by damping of the unstable waves. In direct-drive targets, all electron densities up to critical ($n_e \sim 8 \times 10^{21} \text{ cm}^{-3}$ for 0.351- μm light) can be accessed by the laser. As a consequence of the dispersion relations of the participating waves, SBS can take place anywhere in the underdense region $n_e < n_c$, and SRS can take place anywhere below the quarter-critical surface $n_e \leq n_c/4$. At the quarter-critical surface SRS is in competition with two-plasmon decay (TPD), a particularly dangerous instability because of its low threshold and its ability to produce hot electrons that preheat the target. Complicated physics is expected at the critical surface itself, including but not limited to resonance absorption, profile modification, instability, and surface rippling.² Interactions in the underdense plasma corona are further complicated by the crossing of multiple beams. These beams can interact parametrically via common decay waves, excited simultaneously by several beams, or via electromagnetic seeding involving specular or parametric reflections at or near the critical-density surface. The need to take into account such complications means that simple theoretical models are of rather limited use. One must adopt multidimensional simulation tools that are able to model the necessary physical processes on a large scale in order to have a hope of interpreting current experimental data and making predictions for future experiments.

While modeling LPI in *indirect-drive*-relevant plasmas has received a great deal of attention, and several semipredictive simulation codes have been developed,^{3,4–6} the same cannot be said for direct drive. Recently pF3D, a three-dimensional, parallel LPI interaction code developed by LLNL, has been modified at LLE for use in direct-drive conditions. The significant advantage of pF3D³ over the code *HARMONHY*⁴ is its efficient parallelization using message passing, which has been exploited using Hydra, a 64-processor SGI Origin. This article describes recent developments in this regard, and in addition to some background on pF3D and similar codes, shows some of the first results that have modeled long-scale-length OMEGA multibeam experiments.

This article is organized as follows: The next section gives the background behind the modeling of large-scale LPI experiments and includes a discussion of the physical effects that make such simulations especially challenging. The section on **Simulations** gives details specific to the simulation of OMEGA experiments, including the treatment of the expanding plasma, the critical surface, and collisional absorption. It also contains the first pF3D results in direct-drive geometry, including simulations of SBS backscatter for a range of laser intensities. Simulations exhibiting self-smoothing of laser light are also presented. The final section explains the relevance of these simulations not only to present, but also to future OMEGA and National Ignition Facility (NIF) experiments. Further advances expected in the near future are also explored.

The Physics of Large-Scale Modeling

One of the reasons for the complexity of LPI, and indeed plasma physics in general, is the mixing between disparate length scales. In LPI, the plasma response at scales around a fraction of the laser wavelength λ_0 is generally not independent of those taking place at the much larger hydrodynamic scale length of the target, l_h . For NIF-scale targets irradiated by 0.351- μm light, this ratio can be very large:

$l_h/\lambda_0 \sim 10^3$ to 10^4 (an example of this is the onset of large-scale flow due to SBS momentum deposition⁷). In recent years one advance in simulations that has made large-scale simulations possible has been the use of wave-envelope methods^{3,4,8} that attempt to surmount these problems.

Another major complication for LPI is the complexity of the plasma response. Typical experimental scales of interest to laser fusion (both direct and indirect drive) are lengths of the order of 1 mm and times of 1 ns. It is quite impossible to model the plasma over these scales using any first principles model, such as particle-in-cell (PIC), Vlasov, or Fokker-Planck. One must necessarily deal with a reduced description, the simplest being the plasma fluid, where the only information retained from the single particle distribution function is its hydrodynamic moments. Although fluid models are the simplest (though still containing a host of nonlinearities), one cannot often neglect linear and nonlinear kinetic effects. Advances have been made in combining both linear wave-particle interaction (Landau damping),⁹ electron kinetic effects such as nonlocal electron transport,⁴ and nonlinear frequency shifts¹⁰ into fluid codes.

1. Wave-Envelope Methods and the Paraxial Approximation

The basic idea in wave-envelope methods is to take advantage of the fact that it is often possible to write the transverse electric field of the laser as a sum of components that are each well characterized by a given frequency and wave number and also well separated from one another (spectrally). By enveloping around, and hence explicitly removing, the characteristic spatial and temporal frequency of each component, one arrives at equations where only the slow variation of the envelope needs to be followed. This leads to a relaxation of numerical constraints, coarser grids, and larger simulation volumes. An example of this is the paraxial approximation where one needs only to resolve the Rayleigh length and not the wavelength of the light. In the paraxial approximation, the constraint that the envelope function be slowly varying in space restricts the model to describe only light propagating within a range of wave numbers and frequencies not too far from the characteristic frequencies. Experience shows that an angular $\pm 30^\circ$ can be tolerated, but this is often good enough for practical purposes.¹¹ Complications are that the plasma responds to the ponderomotive force and ohmic heating, which are quadratic in the electric field. Hence there are ponderomotive and thermal sources at the beat frequencies, both spatial and temporal, of all the transverse components. To retain the advantage, the plasma response must likewise be harmonically decomposed around each frequency present, taking into ac-

count nonlinear couplings between each,⁷ as is done in both pF3D³ and *HARMONHY*,⁴ i.e., it is through the plasma response that the transverse electromagnetic components are nonlinearly coupled.

To make these general statements more concrete, we will describe how the above procedure applies to SBS (both near-backward and near-forward) in the simulation codes pF3D and *HARMONHY* (although the algorithms differ between the two codes, the general approach is essentially the same in each). Raman scattering can be treated in a similar way, but for simplicity we will consider only Brillouin here. Consider a transverse electromagnetic wave characterized by its amplitude $\tilde{\mathbf{E}}$. The time-enveloped amplitude \mathbf{E} is defined by the equation $\tilde{\mathbf{E}} = \mathbf{E} \exp(-i\omega_0 t) + \text{c.c.}$, and it satisfies the time-enveloped Maxwell equation:

$$\left\{ 2i\partial_t + \frac{c^2}{\omega_0} \nabla^2 + \omega_0 \left[1 - \frac{n_e}{N_c} (1 - i\nu_{ei}/\omega_0) \right] \right\} \mathbf{E} = 0, \quad (1)$$

where \mathbf{E} is assumed to vary on time scales much greater than ω_0^{-1} . We have ignored here the term proportional to $\nabla(\nabla \cdot \mathbf{E})$, but we have retained the damping of electromagnetic waves, usually neglected in underdense plasma, since it is important close to the critical surface in direct-drive plasmas. Motivated by physical arguments, we expect the electric field to contain two spectral features, one corresponding to transverse waves propagating in the general direction of the laser axis and another propagating in the near-backward direction (SBS in the underdense region is expected to be reasonably well collimated in the backward direction as the longitudinal correlation length of the laser is greater than in the transverse direction by a large multiple of the f number). Hence, we write

$$\begin{aligned} \mathbf{E}(\mathbf{x}, t) = & \mathbf{E}_+(\mathbf{x}, t) \exp \left[i \int_0^z k_0(z') dz' \right] \\ & + \mathbf{E}_-(\mathbf{x}, t) \exp \left[i \int_z^L k_0(z') dz' \right]. \end{aligned} \quad (2)$$

Here the axially dependent wave number $k_0(z)$ must satisfy the linear dispersion relation for transverse waves $k_0(z) = \omega_0/c \sqrt{1 - N_{e,\text{sec}}/N_c}$, and the electron density $N_{e,\text{sec}}$ is defined later in Eqs. (4) and (6). The slowly varying envelopes then satisfy the equations

$$\begin{aligned} & \left(\partial_t + V_g \partial_z + \frac{1}{2} \partial_z V_g + \frac{v_{ei}}{2} \right) \mathbf{E}_+ - \frac{ic^2}{2\omega_0} \left(\varepsilon_{\text{par}} \partial_z^2 + \nabla_{\perp}^2 \right) \mathbf{E}_+ \\ & = -i \frac{\omega_0}{2N_c} (n_0 \mathbf{E}_+ + n_1 \mathbf{E}_-), \end{aligned} \quad (3a)$$

$$\begin{aligned} & \left(\partial_t - V_g \partial_z - \frac{1}{2} \partial_z V_g + \frac{v_{ei}}{2} \right) \mathbf{E}_- - \frac{ic^2}{2\omega_0} \left(\varepsilon_{\text{par}} \partial_z^2 + \nabla_{\perp}^2 \right) \mathbf{E}_- \\ & = -i \frac{\omega_0}{2N_c} (n_0 \mathbf{E}_- + n_1^* \mathbf{E}_+), \end{aligned} \quad (3b)$$

where $V_g = c^2 k_0(z)/\omega_0$ is the magnitude of the group velocity of the light and $v_{ei} = 4/3\sqrt{2\pi} \ln \lambda e^4 Z n_e m_e^{-1/2} T_e^{-3/2}$ is the electron-ion collision frequency, which is responsible for the collisional damping of the electromagnetic waves. The parameter ε_{par} has been introduced, and it takes on the values $\varepsilon_{\text{par}} = 0$ or 1 , corresponding to the paraxial approximation and the unapproximated wave equation, respectively. Notice that the paraxial approximation assumes that $\partial/\partial z \ll k_0$.

2. Plasma Response

The presence of the high-frequency beat terms between E_+ and E_- in the ponderomotive force,

$$F_{\text{pond}} = \nabla U = e^2 / (4m_e \omega_0^2) \nabla |\mathbf{E}|^2,$$

motivates a decomposition of all the fluid variables in the same fashion as outlined here for the electron density n_e :

$$n_e = N_0 + [n_1 \exp i\psi(z) + \text{c.c.}]. \quad (4)$$

In this decomposition, n_1 is the (complex) amplitude of the ion-acoustic wave (IAW) driven by the backward SBS process, whose phase $\psi(z)$ is given by

$$\psi(z) = \int_0^z k_0(z') dz' - \int_z^L k_0(z') dz',$$

so that $\partial_z \psi(z) = k_{\text{IAW}}(z)$, where $k_{\text{IAW}} = 2k_0$ denotes the local wave number of the SBS-driven IAW. The amplitude satisfies

$$\begin{aligned} & \left(\frac{d}{dt} + 2ik_0 u_z + v_{\text{ia}} \right)^2 n_1 + \left(\omega_a - 2ik_0 C_a^2 \frac{\partial}{\partial z} - C_a^2 \nabla^2 \right) n_1 \\ & = -k_0^2 \frac{Zm_e}{m_i} N_0 E_+ E_-^* + S_a, \end{aligned} \quad (5)$$

where

$$d/dt = \partial/\partial t + \mathbf{u} \cdot \nabla$$

is the convective derivative, $C_a = \sqrt{(ZT_e + 3T_i)/m_i}$ is the IAW sound speed, v_{ia} is the ion-acoustic damping rate, and S_a is the thermal Cherenkov source of ion waves. (We have changed the notation slightly from Ref. 3.) In Eq. (4), N_0 denotes the slowly varying part of the electron density for which the quasi-neutral limit is correct. For use in Eqs. (3), the slowly varying part N_0 must itself be decomposed into a sum of a secular piece, $N_{e,\text{sec}}$, and a quasi-static, large-scale perturbation n_0 ,

$$N_0 = N_{e,\text{sec}} + n_0. \quad (6)$$

The secular piece of the background equilibrium electron density is the part that varies over the interaction region, due to hydrodynamic expansion of the target, and whose phase has been taken into account by allowing k_0 to be a function of z in the usual WKB (Wentzel, Kramers, Brillouin) manner. Its value at a particular axial location is equal to the transverse spatial average of N_0 . The quasi-static, large-scale perturbation n_0 is related to flow generation caused by momentum transfer, self-focusing/filamentation, and forward-scattering processes.

The slowly varying plasma-hydrodynamic quantities satisfy a nonlinear set of equations,

$$\partial_t \rho + \nabla \cdot (\rho \mathbf{u}_i) = 0, \quad (7a)$$

$$\begin{aligned} & \partial_t (\rho \mathbf{u}_i) + \nabla \cdot (\rho \mathbf{u}_i \mathbf{u}_i) \\ & = -\nabla (P_i + P_e) - \langle \rho \nabla U \rangle_0 - 2v_{Fp} \rho \mathbf{u}_i, \end{aligned} \quad (7b)$$

$$\frac{3}{2}[\partial_t P_i + \nabla \cdot (\mathbf{u}_i P_i)] + P_i \cdot \mathbf{u}_i = \nabla_{\perp} \cdot (\kappa_i \nabla_{\perp} T_i) + Q_i, \quad (7c)$$

$$\begin{aligned} & \frac{3}{2}[\partial_t \delta T_e + \nabla \cdot (\mathbf{u}_i \delta T_e)] + \delta T_e \nabla \cdot \mathbf{u}_i \\ & = \nabla_{\perp} \cdot (\kappa_{e,NL} \nabla_{\perp} T_e) + Q_e. \end{aligned} \quad (7d)$$

Here, $\rho = m_i N_0 / Z$ is the ion mass density, Z is the average ion charge, $P_e = N_0 T_e$ and $P_i = (\rho / m_i) T_i$ are the electron and ion pressures, respectively, Q_e and Q_i are the electron and ion heating rates, κ_i and $\kappa_{e,NL}$ are the ion and (possibly nonlocal) electron thermal conductivities, and the quantity ν_F denotes the damping operator describing Landau damping and ion-ion collisions (see Ref. 12).

Most efforts have concentrated on hohlraum conditions, where no critical surface is present, but we are now applying pF3D, solving Eqs. (3), (5), and (7) to OMEGA direct-drive experiments.

Simulations of Long-Scale-Length OMEGA Experiments

Experimental OMEGA campaigns have addressed LPI conditions that closely resemble NIF direct-drive ignition targets at the start of the main pulse using single, staggered multiple-beam irradiation of solid, planar CH targets. Full-aperture backscatter stations (FABS) have measured the time-integrated, time-resolved SBS as well as SRS backscatter energy and spectra. In the present work, we discuss SBS and make comments about TPD only. In general terms, the level of observed SBS backscatter for single-beam, normal incidence increases exponentially with laser intensity up to intensities of about 2×10^{14} W/cm², with corresponding reflectivities of ~1%, after which it begins to saturate with reflectivities greater than, or around, 10%. This level can be reduced significantly by the addition of SSD (smoothing by spectral dispersion) bandwidth (0.5 or 1 THz experimentally) and by polarization smoothing (PS), both of which seem to be more efficient at removing the frequency upshifted (blue) part of the backscattered spectrum than the downshifted (red), and leads to reflectivities of a fraction of a percent. Similar behavior is also seen in the case of multiple-beam irradiation.

The SBS spectra (features near $\lambda_0 \sim 351$ nm) consistently show two distinct features. One feature (referred to as the

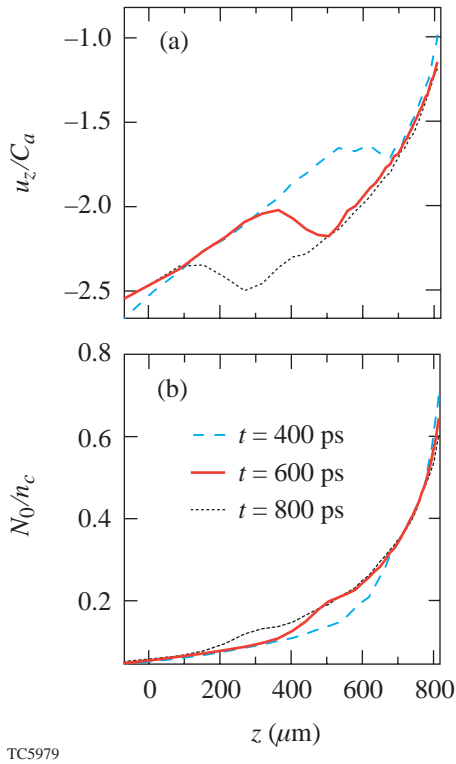
“blue feature”) has a shift to shorter wavelengths that increases in time up to a maximum experimentally observed spectral shift of $\delta\lambda = \lambda_0^2 / (2\pi c) \delta\omega \sim 1$ nm. This is due to SBS in the underdense plasma corona where the flow velocity due to target expansion is supersonic and $|\mathbf{u}_i| > C_a$. The other spectral feature is shifted to longer wavelengths (the “red feature”) and is seen predominantly in the specular direction, i.e., if the beam is not normally incident and there is no opposing beam that could specularly reflect light into the FABS, then this feature is absent. This feature must arise from interactions very close (tens of microns) to the critical surface and is presumably seeded by specular reflection. The blue component is observed only in the backscatter direction and is seen regardless of the angle between the laser axis and the target normal. The temporal duration of the blue feature also differs between multibeam and single-beam irradiation, but this is likely due to the different hydrodynamics between the two targets. It then seems that the two spectral features have their origins in two well-separated regions in the plasma. Based on the expected hydrodynamic profile, from *SAGE* simulations,¹³ the red feature must come from a region separated by only tens of microns from the critical surface, whereas the blue feature comes from a region hundreds of microns out into the corona. The critical region is not currently modeled in a self-consistent manner in pF3D and will not be addressed in detail here. (The actual details on how the critical surface is presently treated will be detailed below.) Work is under way to study this region separately using a full-wave code that does not assume the paraxial approximation and uses the pF3D simulations to provide the necessary boundary conditions.

Detailed understanding of the experiment is necessary for confident predictions and future NIF/OMEGA experiments. Before proceeding with our simulations relevant to the current OMEGA experiments, we will discuss in detail the modeling of both the inhomogeneous plasma profile and the critical surface.

1. Modeling the Hydrodynamic Expansion of the Target

Hydrodynamic evolution of the target during the nanosecond laser pulse is significant, and previous experience with experiments conducted at LULI has shown that this must be modeled accurately for close agreement with experimental data.¹⁴ The predictive value of *SAGE* has been verified over several experimental campaigns, so we have chosen to initialize our plasma hydrodynamics using data provided by *SAGE*. Figure 91.1 shows the initial conditions, taken from *SAGE*, corresponding to the z component of the expansion velocity \mathbf{u}_i and the plasma electron density N_0 for various times relative

to the start of the interaction pulse. This flow velocity gives a spatially dependent Doppler shift to IAW, and its gradient localizes the three-wave SBS interaction, which are all essential features of the experiment.



TC5979

Figure 91.1

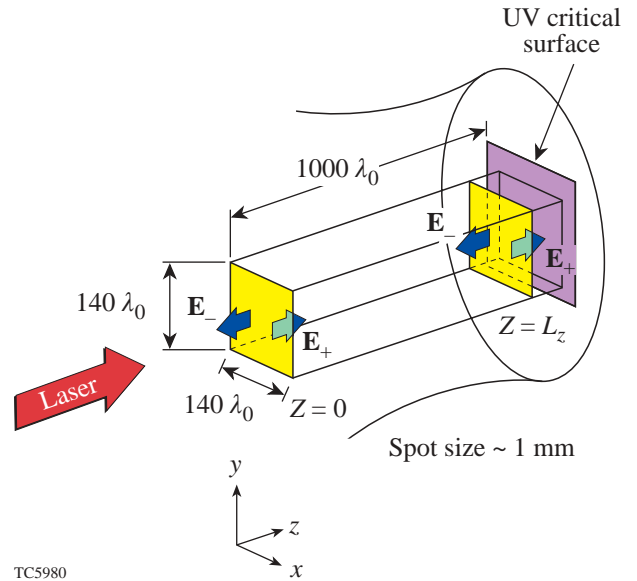
The component of the plasma expansion velocity (normalized to C_a for hydrogen at 1 keV) in the direction of the target normal, and electron plasma density as a function of the axial coordinate z . The gradient in the expansion velocity limits the resonance region for backward stimulated Brillouin scattering due to the detuning of the three-wave coupling via a flow-induced Doppler shift in the IAW frequency. The important feature is the plateau that provides a more-favorable region for SBS growth, which moves outward toward the laser and lower electron plasma densities in time. The three curves (dashed, solid, dotted) correspond to the times 400, 600, and 800 ps after the start of the interaction pulse, respectively.

2. Modeling the Critical Surface

To relax the numerical constraints in the electromagnetic part of the problem, we previously used the paraxial approximation by setting $\epsilon_{\text{par}} = 0$ in Eq. (3). This causes difficulty near the critical surface, however, since the local wave vector $k_0(z)$ there is smaller and vanishes, $k_0(z_t) = 0$, at the turning point $z = z_t$, invalidating our approximation. One approach is to retain the second derivative in Eqs. (3) in a region surrounding the critical surface. We currently adopt a simpler method: Fig. 91.2 shows a typical simulation volume having its z axis

along the target normal and with the plasma density increasing with the axial coordinate due to target expansion. The length of the simulation box is chosen so that $n_e(z = 0) \sim 0.1 n_c$ and $n_e(L_z) \sim 0.7\text{--}0.8 n_c$, which implies a standoff of approximately $10 \mu\text{m}$ from the end of the simulation volume and the UV critical surface. Appropriate DPP boundary conditions must be provided for E_+ at $z = 0$ (see Fig. 91.3). The boundary conditions for E_- at $z = L_z$ are obtained by treating the end of the simulation volume as a partially reflecting mirror by setting

$$E_-(\vec{x}_\perp, L_z) = \sqrt{R(t)} E_+(\vec{x}_\perp, L_z),$$



TC5980

Figure 91.2

The typical geometry used in simulating direct-drive LPI experiments. The solid target is assumed to have its outward normal along the z axis (pointing to the left), with the UV critical surface as indicated. The laser is incident from the left. The simulation volume is smaller than the envelope of the beam as indicated; DPP and SSD are modeled by applying the appropriate boundary condition (i.e., amplitude and phase) for the complex electric-field envelope E_+ at $z = 0$ (see Fig. 91.3). This gives rise to the characteristic speckle pattern in the box as it propagates to the end of the box at $z = L_z$. The region between $z = L_z$ and the UV critical surface is not modeled in pF3D, but the reflection from the critical surface is accounted for by setting $E_- = \sqrt{R} E_+$ at $z = L_z$, where R is the reflectivity arising from the stand-off region as calculated from the *SAGE* hydrodynamic profile. The envelope E_- then propagates backward through the box, exiting at $z = 0$, where the plasma reflectivity can be measured. Typically, the simulation volume is reduced to two dimensions with backward SBS present due to numerical constraints.

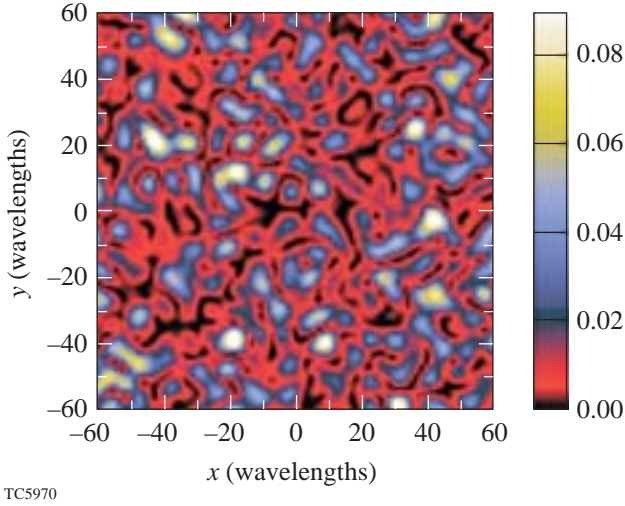


Figure 91.3

An example of the electric-field density, normalized to the average intensity, taken on the entrance plane of the box $z = 0$. This was created assuming the cylindrical top-hat model (in three dimensions)²¹ corresponding to an $f/6$ DPP.

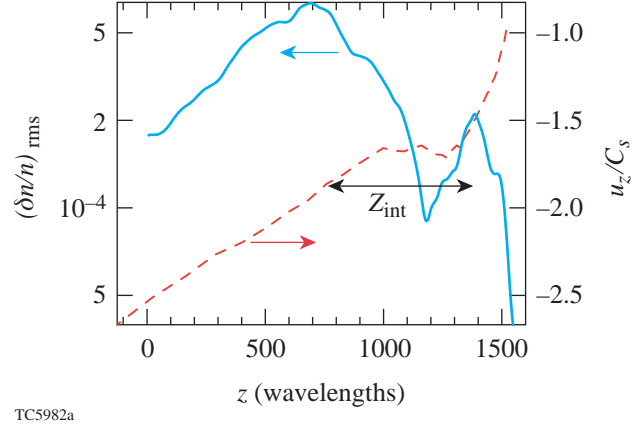


Figure 91.4

IAW amplitudes n_1 [see Eq. (5)] averaged over the transverse extent of the simulation box, and plasma expansion velocity as a function of the axial coordinate z . Notice that there are two regions of significant IAW amplitude, one around the sonic point, where IAW's are resonantly driven by specularly reflected light, and the other corresponding to the shelf in plasma expansion velocity, where backward SBS gain is high.

with the reflectivity coefficient given by

$$R = \exp \left[2 \int_{L_z}^{z_t} \kappa_{ab}(z', t) dz' \right],$$

where $\kappa_{ab} = v_{ei}/V_g$. Typical values near the peak of the interaction pulse are $R \sim 0.6$. In this way, the electromagnetic (EM) backscatter seed has at least the proper intensity for the corresponding SAGE profile (if nonlinear interactions are negligible). The phase is not correct, although this is not expected to be important. Changes to this model will be made as our understanding regarding the nonlinear interactions near critical is improved. Angular and frequency broadening will be modeled if it is found to be important. We will incorporate a full-wave solver near the turning point if necessary.

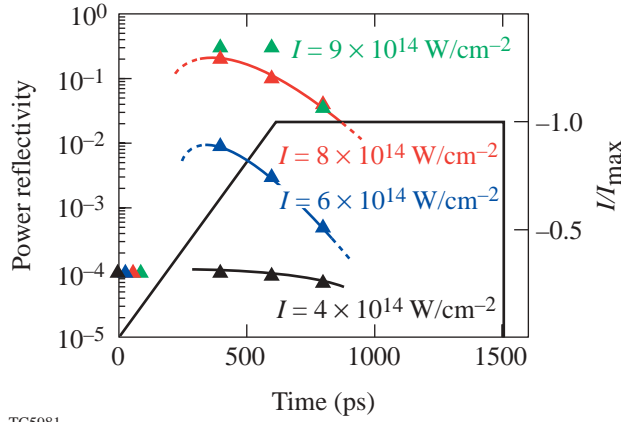
3. SBS Backscatter Signal in Simulation and Experiment

As in the experiment, simulations show a blue feature in the spectrum of backscattered light due to SBS coming from a flat region of expansion velocity. Indeed, examination of the plasma expansion velocity profile (Figs. 91.1 and 91.4) shows that there is a preferred location for SBS growth, the flat “shelf” of uniform velocity, which has a characteristic size of $\sim 200 \mu\text{m}$. In all other parts of the profile, the inhomogeneity scale length is short. This shelf is swept further downstream (toward the laser) with time, so that at later times the local

plasma density at the shelf falls rapidly (see Fig. 91.1). Based on an estimate of the expected SBS intensity gain in the shelf region, we may also be able to explain simply the early “quenching” of the SBS signal seen in the multibeam experiments.¹⁵ Assuming the strong damping limit, and a uniform expansion velocity, the convective intensity gain in practical units is given by $I_{\text{SBS}} = I_{\text{seed}} \exp(G)$, with $G = z_{\text{int}}/L_G$, and

$$L_G^{-1} = 0.045 \frac{1}{v_i} \frac{\omega_0}{c} \frac{n_e/n_c}{\sqrt{1-n_e/n_c}} I_{15} \lambda_{\mu\text{m}} \frac{1}{T_{\text{keV}}}. \quad (8)$$

Taking z_{int} to be $\sim 200 \mu\text{m}$ (as Fig. 91.1 shows to be the length of the shelf), $v_{ia}/2k_0 C_a = 0.1$, $I_{15} = 0.4$, $\lambda_{\mu\text{m}} = 0.351$, and $T_{\text{keV}} = 2.2$, we arrive at a gain G that as a function of the plasma density, $G \sim 100(n_e/n_c)/\sqrt{1-n_e/n_c}$, drops from a value of $G = 30$ to 10 as the plasma density drops from $n_e/n_c = 0.25$ to 0.1. This factor-of-3 reduction in the gain as the shelf moves to lower density (Fig. 91.1) explains why the SBS signal drops when the laser intensity is at its peak. This gain will be achieved after a time, τ_{SBS} given approximately by $\tau_{\text{SBS}} \sim G/v_{ia}(2k_0) < 30$ ps. Figure 91.5 shows actual power reflectivities, taken from recent pF3D simulations, at various times in the pulse (to gain a picture of the interaction over the whole laser pulse, some approximations have been made¹⁶).



TC5981

Figure 91.5

Laser power reflectivity, as a function of time, taken from simulations corresponding to a range of maximum average laser intensities between $I = 4 \times 10^{14} \text{ W/cm}^2$ and $I = 9 \times 10^{14} \text{ W/cm}^2$. The laser pulse was turned on at $t = 0$ and then ramped linearly to maximum intensity in 500 ps after which it was held fixed for an additional 1 ns, as in typical OMEGA experiments. Notice that the reflectivity peaks early in the pulse.

Currently we are investigating the more complicated, and less easily predicted, effects of EM seeding from the critical surface and the effects of multiple-beam irradiation and quantifying the ability of SSD bandwidth to suppress SBS.

a. EM seeding of backward SBS. The EM seeding of Brillouin backscatter in the strongly underdense region is affected by the plasma inhomogeneity. Each frequency component of the backscattered light can be resonant with ion waves only in a spatially narrow region such that the frequency-matching conditions are satisfied locally and $\omega_0 - \omega_1 = \omega_{\text{IAW}}[1 - M_{\parallel}(z)]$, where ω_1 is the frequency of the backscattered radiation and $\omega_{\text{IAW}} = |\mathbf{k}_{\text{IAW}}|C_a$ is the IAW frequency for a sound wave with wave number \mathbf{k}_{IAW} . The spatial extent of this resonance region is determined by the width of the ion-acoustic resonance $\sim v_{\text{ia}}^{-1}$ and the scale length of the flow Mach number \mathbf{M} . The wave-number-matching conditions $\mathbf{k}_0 = \mathbf{k}_1 + \mathbf{k}_{\text{IAW}}$ are determined by the scattering geometry only since the magnitude of the wave vector of scattered light is essentially unchanged, $|\mathbf{k}_1| \approx |\mathbf{k}_0| = \omega_0/c\sqrt{1 - n_e/n_c}$, because the shift by the ion-acoustic frequency $\omega_0 - \omega_1$ is very small compared to ω_0 .

It has been suggested that the sonic point is of special importance because light specularly reflected by the critical surface with little or no spectral shift¹⁷ will be resonant with the IAW at this point and may drive them to large amplitude.

This effect is evident in Fig. 91.4. The resonance may be less important, however, if the reflected light is not monochromatic and is spread in angle and frequency due to nonlinear interactions near the critical surface. In addition, experimental evidence indicates that the absorption is much greater than predicted by Eq. (10), and the backscattering seed at the sonic point may be substantially less than is shown in Fig. 91.4. We would not expect specularly reflected light to provide an efficient seed for SBS occurring in the supersonic region due to the large frequency mismatch.

In summary, the parametric reflections from other beams (in multibeam geometries) are expected to be more important than specular reflection for seeding the blue part of the scattered light spectrum, and there is much experimental evidence for synergy between the beams, while interactions near the sonic point are influenced by both specular and parametric reflections in both single and multibeam geometries. The region near the critical surface associated with the red feature in the spectrum of reflected light is the most complicated and best investigated with a code capable of solving the full wave equation.

b. Anomalous absorption. In the absence of parametric reflections, at low intensity, one would expect the laser absorption η to be due to classical inverse Bremsstrahlung only. Integrating the equations for laser intensity [obtained from Eq. (3)],

$$\frac{\partial}{\partial z} (V_g |E_{\pm}|^2) = \mp \frac{V_{ei}}{V_g} (V_g |E_{\pm}|^2), \quad (9)$$

over *SAGE* density and temperature profiles, one obtains the reflectivity $R = 1 - \eta$, where

$$R = \exp \left[-2 \int_0^{z_t} \kappa_{ab}(z') dz' \right], \quad (10)$$

$\kappa_{ab} = v_{ei}/V_g$ is a function that depends on the density and temperature, and z_t is the turning point for the transverse waves, defined by $1 - n_e(z_t)/n_c - \sin^2(\theta) = 0$. For a *SAGE* profile at $t = 400$ ps, the above formula predicts $R = 0.025$ (for $\theta = 0^\circ$). This lower bound on the reflectivity is larger than the experimentally observed reflectivity by approximately two orders of magnitude.

Possible explanations for this serious discrepancy include inaccuracies in the *SAGE* profiles near the critical surface, where most of the absorption occurs, and where it is especially sensitive to temperature through the electron-ion collision frequency,

$$v_{ei} \sim 8.16 \frac{\ln \Lambda}{10} Z_{\text{eff}} \frac{n_e}{n_c} \left(\frac{0.351}{\lambda_{0,\mu\text{m}}} \right)^2 T_{e,\text{keV}}^{-3/2} \text{ ps}^{-1}, \quad (11)$$

a factor that appears in the exponent of the equation for the reflectivity, Eq. (10). Other possible explanations are the geometric effect of diffuse scattering through a rough critical surface (although a scattering into 2π radians would be required, and this can be ruled out experimentally) and increased collisionality brought about by ion turbulence. A close investigation of the backscatter spectrum, together with pF3D simulations, might be the best route to resolving this outstanding problem and offers the possibility of providing a diagnostic for laser absorption.

4. Self-Focusing Instability and Self-Smoothing

Another area where pF3D simulations are expected to provide insight is the investigation of so-called plasma-induced self-smoothing of laser light. This is a mechanism in which the spatial and temporal correlation length of the laser can be dramatically reduced, as a result of nonlinear plasma response related to the self-focusing (SF) instability and forward SBS. Although this is presently a very active area of research, with strong experimental evidence showing its importance to backward SBS in underdense plasmas,^{18–20} effects likely of importance to direct drive such as laser imprint and saturation of TPD have not been investigated either experimentally or theoretically (including through simulation).

The onset of self-smoothing is related to the SF instability and has a threshold which, in practical units, is given by

$$p \sim 0.39 \frac{I_{15} \lambda_{\mu\text{m}}^2}{T_{e,\text{keV}}} f_{\#}^2 \left(\frac{n_e}{n_c} \right) > 1, \quad (12)$$

where the factor of order unity (0.39 here) comes from assuming a cylindrical top-hat DPP (distributed phase plate) spectrum in 3-D.²¹ For relevant parameters, it is seen that SF might become important at higher intensities, nearing $1 \times 10^{15} \text{ W/cm}^2$. This is demonstrated in Fig. 91.6, which shows

a longitudinal slice of the electric-field intensity of a DPP beam. Notice the reduction in the size of the laser speckle pattern, which is also associated with a reduction in the laser coherence time.

The increased incoherence of the laser beam can disrupt and reduce the level of coherent parametric instabilities, which is beneficial for inertial confinement fusion (ICF). Regarding SBS, the shelf in the expansion velocity makes the OMEGA experiments quite different from previous investigations of SBS in inhomogeneous plasmas, where there was no preferential region for growth. Competition between self-smoothing and SBS can be revealed by the spatial location of SBS ion waves, as reported for LULI experiments using a Thomson-scattering diagnostic.¹⁸ A close examination of

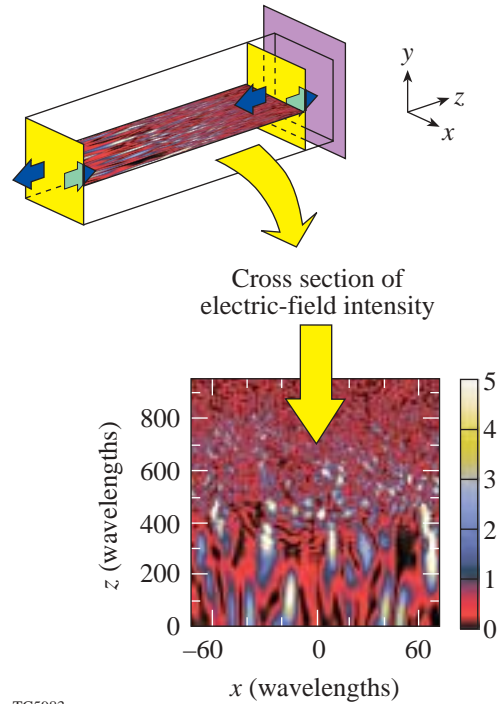


Figure 91.6

At laser intensities nearing $I = 1 \times 10^{15} \text{ W/cm}^2$, the threshold for the self-focusing instability [Eq. (12)] is exceeded in the intense laser speckles. This leads to a reduction in the transverse correlation length of the laser light and frequency broadening. This effect, which has become known as plasma self-induced smoothing, could have an impact on parametric processes such as the two-plasmon-decay instability. This figure illustrates this by showing a longitudinal cross section of the laser intensity (in real space), normalized to the average intensity. The light propagates along the z axis, from bottom to top in the figure. The quarter-critical surface is just beyond the region where the self-smoothing has set in. This could have a saturating effect on the two-plasmon-decay instability.

the SBS signal at high laser intensity may then give valuable information on self-smoothing. This is of broad significance because the incoherence generated by filament instability that is responsible for self-smoothing will affect all resonant parametric processes.

Self-smoothing could have important consequences for the TPD instability since the observed behavior of TPD electrons seems to suggest saturation near 10^{15} W/cm², which is similar to the threshold of SF. The TPD instability, as inferred from fast electrons, is also dependent on SSD bandwidth. This dependence seems consistent with a reduction of filamentation at higher SSD bandwidth. The addition of SSD bandwidth is assumed to suppress SF/filamentation,^{22,23} but this has not been studied in the present context.

Discussion

We began by discussing the importance of large-scale simulations in the interpretation and understanding of LPI in ICF fusion experiments and the differences between the indirect- and direct-drive approaches. We also outlined the difficulties and challenges that these types of simulations present and indicated that LPI in direct-drive plasmas has received comparatively little attention. We have set out to remedy this situation and have, in collaboration with LLNL, begun to modify the interaction code pF3D for use in modeling direct-drive plasmas.

The first pF3D results of backward SBS scattering using a realistic inhomogeneous plasma profile, as predicted by the code *SAGE* for recent LPI interaction experiments, have been presented. These simulation results have been used to interpret the experimental backscatter data and have reproduced the behavior of the blue spectral feature observed. Future work will carefully examine the effect of SSD bandwidth and polarization smoothing.

The narrow region near critical is currently treated in a rather simple way. This region is being studied with a separate code for solving the full wave equation. These two codes could be integrated in the future if necessary.

A large discrepancy was found in the level of absorption due to inverse bremsstrahlung between that calculated from *SAGE* and the value obtained experimentally. The level of ion-acoustic fluctuations near the sonic point is dependent on the plasma reflectivity and may potentially be used as a diagnostic for absorption. The pF3D code may be used in conjunction with experiments to resolve this problem.

Finally, it was demonstrated that self-smoothing will become important at higher laser intensities, which will impact all parametric processes including SBS, SRS, and TPD. It will also modify the laser imprint. Due to the potential importance of all these processes, the newly modified pF3D will be used to address these issues in the very near future.

ACKNOWLEDGMENT

This work was supported by the U.S. Department of Energy Office of Inertial Confinement Fusion under Cooperative Agreement No. DE-FC03-92SF19460 and the University of Rochester. The support of DOE does not constitute an endorsement by DOE of the views expressed in this article. The author also thanks C. H. Still and R. L. Berger for their assistance.

REFERENCES

1. J. D. Lindl, *Phys. Plasmas* **2**, 3933 (1995).
2. E. J. Valeo and K. G. Estabrook, *Phys. Rev. Lett.* **34**, 1008 (1975).
3. R. L. Berger *et al.*, *Phys. Plasmas* **5**, 4337 (1998).
4. J. Myatt, D. Pesme, S. Huller, A. Maximov, W. Rozmus, and C. E. Capjack, *Phys. Rev. Lett.* **87**, 255003 (2001).
5. V. V. Eliseev *et al.*, *Phys. Plasmas* **3**, 3754 (1996).
6. S. Huller, Ph. Mounaix, and V. T. Tikhonchuk, *Phys. Plasmas* **5**, 2706 (1998).
7. D. Pesme, presented at the LLNL Workshop on Saturation of Simulated Raman and Brillouin Instabilities, Livermore, CA, 3–5 April 2002.
8. H. A. Rose, *Phys. Plasmas* **4**, 437 (1997).
9. H. A. Rose, *Phys. Plasmas* **3**, 1709 (1996).
10. L. Divol *et al.*, *Bull. Am. Phys. Soc.* **46**, 293 (2001).
11. A. Maximov, Laboratory for Laser Energetics, private communication (2001).
12. H. A. Rose, *Phys. Plasmas* **3**, 1709 (1996).
13. R. S. Craxton and R. L. McCrory, *J. Appl. Phys.* **56**, 108 (1984).
14. V. T. Tikhonchuk, J. Fuchs, C. Labaune, S. Depierreaux, S. Huller, J. Myatt, and H. A. Baldis, *Phys. Plasmas* **8**, 1636 (2001).
15. Laboratory for Laser Energetics LLE Review **87**, 128, NTIS document No. DOE/SF/19460-397 (2001). Copies may be obtained from the National Technical Information Service, Springfield, VA 22161.
16. We have adopted the following methodology that assumes that there are no correlations that live longer than several tens of picoseconds. To put this in perspective, the damping time of an ion wave with wave number given by $2\omega_0/c$ is approximately 1 ps, and only ten times larger for forward SBS at 5°. The time for SBS to reach its asymptotic state, τ_{SBS} can be crudely approximated as $\tau_{\text{SBS}} \sim G/v_{\text{ia}}(2k_0)$, which is less than 10 ps. At the chosen starting time the

hydrodynamic profile is initialized with *SAGE* and the laser turned over a few picoseconds to the appropriate intensity. When an asymptotic state is reached, the SBS is expected to be representative of that occurring.

17. The linear phase modulation due the motion of the critical surface imparts a negligible frequency shift.
18. C. Labaune, presented at the LLNL Workshop on Saturation of Simulated Raman and Brillouin Instabilities, Livermore, CA.
19. A. J. Schmitt and B. B. Afeyan, *Phys. Plasmas* **5**, 503 (1998).
20. A. V. Maximov *et al.*, *Phys. Plasmas* **8**, 1319 (2001).
21. H. A. Rose, *Phys. Plasmas* **2**, 2216 (1995).
22. R. L. Berger *et al.*, *Phys. Rev. Lett.* **75**, 1078 (1995).
23. R. L. Berger *et al.*, *Phys. Plasmas* **6**, 1043 (1999).

Highly Stable, Diode-Pumped, Cavity-Dumped Nd:YLF Regenerative Amplifier for the OMEGA Laser Fusion Facility

Introduction

The OMEGA facility is LLE's 60-beam, 30-kJ (UV) laser system for performing inertial confinement fusion (ICF) experiments. One of the main features of the OMEGA laser is a flexible optical pulse-shaping system¹ that produces 0.1- to 5-ns, complex-shaped, low-energy pulses that must be amplified to ~1-mJ level before being injected into power amplifiers. Regenerative amplifiers (regens) are well suited for this application, which requires high energy stability and output-beam quality, including low (<1%) beam ellipticity.

High output-pulse-energy stability was achieved on OMEGA with a negative-feedback system in a flashlamp-pumped regen.² This system establishes a stable prelude before the energy in the cavity starts to build up; however, this feedback system can cause dramatic pulse-shape distortion,³ which is difficult to compensate for. A sophisticated negative-feedback system that does not distort the input-pulse shape was developed for the flashlamp-pumped OMEGA regen.^{4,5} The only pulse-shape distortion in this regen results from gain saturation in the regen's active element.

This article presents the design and test results of a new highly stable, diode-pumped, cavity-dumped, compact Nd:YLF regenerative amplifier that does not use a negative-feedback system and thus has reduced system complexity.

Regenerative Amplifier Concept

The regenerative amplifier is the key component of the OMEGA laser driver line. The following tight requirements on regen stability and beam quality must be met:

- output-pulse energy > 0.2 mJ,
- high long-term energy stability (<1% rms fluctuation),
- high temporal pulse shape stability (<1% rms deviation),
- high beam quality (TEM₀₀; ellipticity <1%),
- wavelength tunability to match gain peak to seed-pulse wavelength, and
- OMEGA operational availability >90% with reliability and compactness.

Two major factors affect regen output-pulse-energy stability: gain fluctuations and injected-pulse-energy fluctuations.

Gain fluctuations change the energy and timing of the intracavity peak pulse; hence, they dramatically affect the regen's output-pulse energy when cavity dumping occurs at a given time. Diode pumping, due to its high stability, makes gain fluctuations negligible, contributing to output-pulse-energy stability. Stable gain also provides high temporal pulse-shape stability because the distortion caused by gain saturation is constant. The end-pump geometry of diode pumping significantly improves beam quality.

Injected-pulse-energy fluctuations primarily change the intracavity peak pulse timing, which causes output-pulse-energy variations when the regen is cavity dumped at a fixed time. In our case, the injected pulse energy changes because of (1) fluctuations in the pulse-shaping system and (2) different input-pulse shapes that present significantly different input-pulse energies. Earlier studies^{6,7} have shown that output-pulse-energy fluctuations due to injected-pulse-energy fluctuations are minimized when the gain-over-loss ratio is high. We have developed a fast and simple regen simulation model that corresponds very well to our experimental results. The rate-equation regen model described in Ref. 6 has been simplified by treating the regen's active element as a thin gain layer. The input pulse is sliced in time. Gain and level populations in the active element are recalculated after each slice propagation using recurrence relations for fluence, gain coefficient, and gain-recovery coefficient. According to our calculations, the energy of the regen intracavity peak pulse depends weakly on the injected pulse energy for a broad range of injected energies, which is in agreement with results obtained in Ref. 7. Also, our calculations show that the peak of the intracavity energy dynamics is relatively flat and the peak pulse energy for different injected energies stays constant for several round-trips. These considerations make the concept of building a highly stable regen without a negative-feedback system viable.

Regenerative Amplifier Design

A cavity-dumped Nd:YLF regen with a 220-cm-long linear cavity has been developed to accommodate shaped pulses of up to 7-ns duration. The regen layout is shown in Fig. 91.7.

The choice of Nd:YLF as an active medium is required to match the gain peak of the Nd:phosphate-glass OMEGA amplifiers. The regen cavity is semiconfocal, formed by high-reflective mirrors—one flat and the other with a 4-m radius of curvature. An $8 \times 8 \times 20$ -mm Nd:YLF active element was placed near the middle of the cavity to avoid pulse-overlap effects during long-pulse amplification. The regen gain center wavelength can be tuned to the injected-pulse wavelength by adjusting the temperature of an active element placed on the Peltier element.

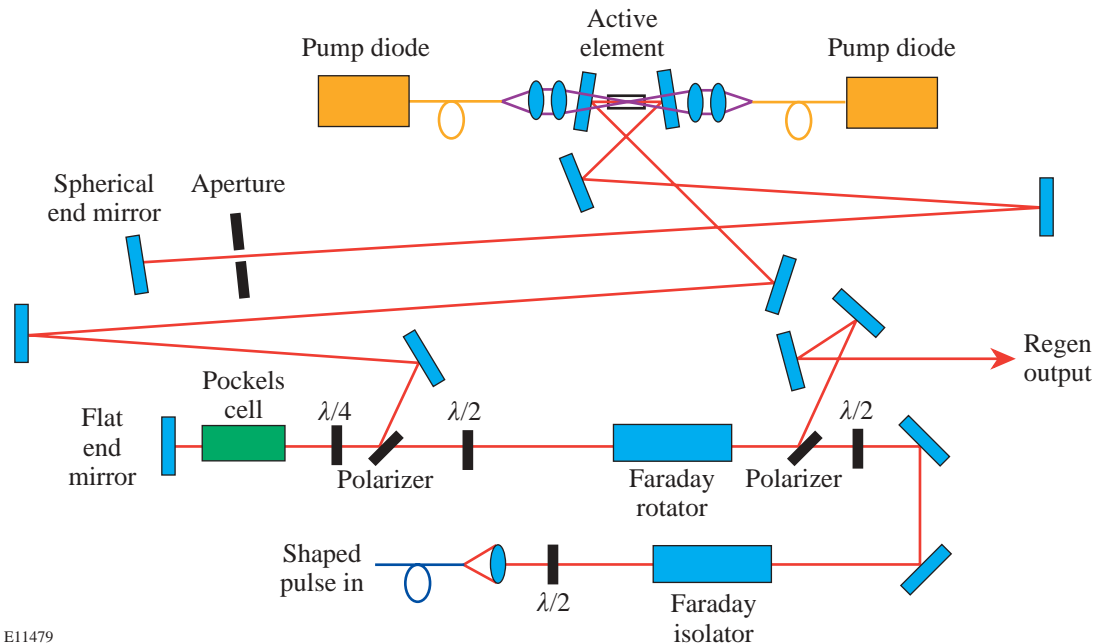
Two 25-W, fiber-coupled diode arrays operating at 805 nm were used for regen pumping. The regen was pumped at a 5-Hz repetition rate, although a higher repetition rate should be possible. An 800- μ s pump-pulse duration was found to be optimal. The 0.6-mm pump fiber core was re-imaged into a 0.9-mm spot in the center of the active element. The cavity mode diameter inside the active element was calculated to be ~ 1 mm, so the pumped volume diameter was smaller than the

mode diameter, allowing it to serve as an intracavity gain aperture. An additional intracavity aperture was installed for tighter beam-quality control.

Regen reliability is provided by a simple cavity design: a no-feedback-system, cavity-dumped linear resonator. A small, 15-in. \times 38-in. regen footprint is provided by folding the cavity. A high gain/loss ratio in the cavity-dumping regime provides output-pulse-energy stability, while a thermostabilized solid-aluminum block design contributes to the overall regen parameter stability (Fig. 91.8).

Experimental Results

To test the regen performance, square optical pulses of various durations and energies produced by our pulse-shaping system¹ were used. First of all, we wanted to demonstrate that our regen simulation model adequately describes regen dynamics. We calculated and measured intracavity regen dynamics [Fig. 91.9(a)] and square-pulse distortion of the regen peak pulse [Fig. 91.9(b)] when a 4-ns FWHM, ~ 170 -pJ square pulse was injected. It is evident that our regen model agrees well with experimental results. (In practice, energies of ~ 10 to 100 pJ are used.)



E11479

Figure 91.7

Layout of the diode-pumped, cavity-dumped Nd:YLF regen, which is able to amplify shaped pulses of up to 7-ns duration.

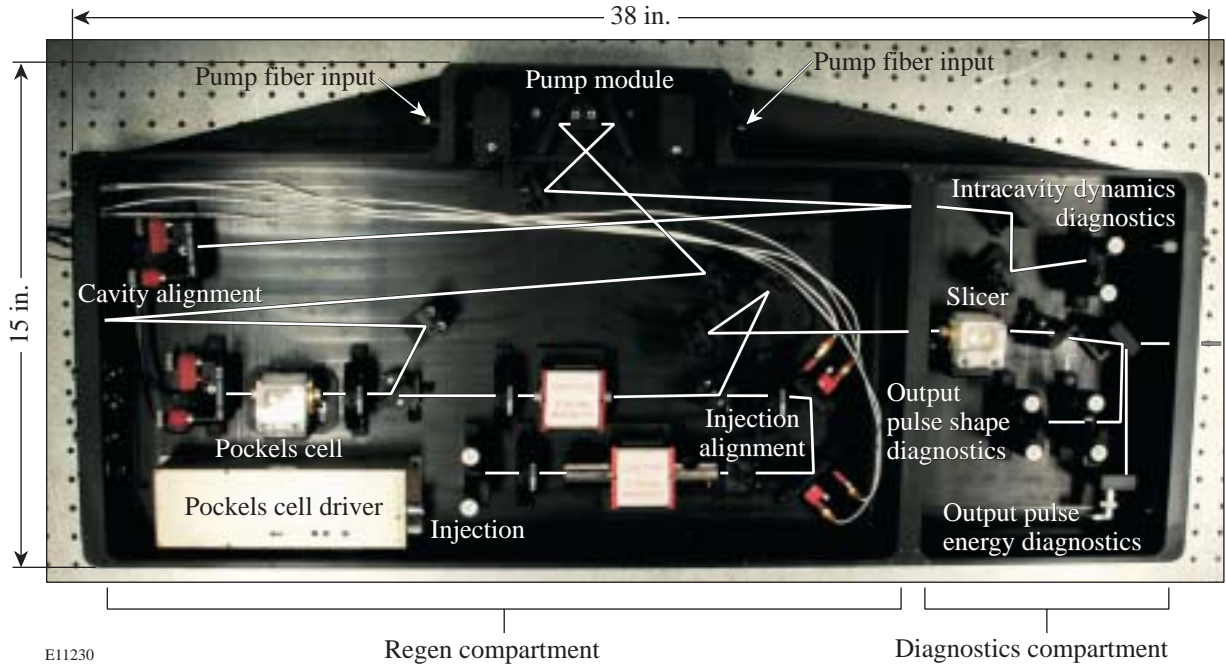
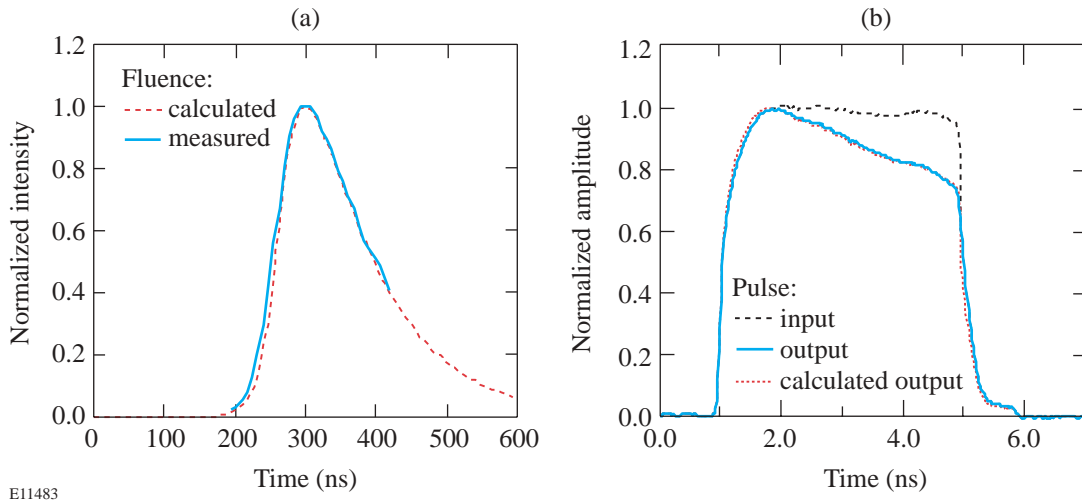


Figure 91.8
 OMEGA diode-pumped regen design. Regen enclosure is made of a solid-aluminum block and includes regen and diagnostics compartments. The regen footprint is 15 in. × 38 in., including an optical diagnostics compartment.



E11483

Figure 91.9
 (a) Regen intracavity dynamics and (b) peak square-pulse distortion calculated and measured for a 4-ns injected square pulse.

To demonstrate regen insensitivity to an injected-pulse energy, we changed the injected square pulse width (energy) and measured the cavity-dumped output-pulse energy [Fig. 91.10(a)]. The output energy stays within a 1% range when injected energy changes by 600%. A decrease in the gain/loss ratio makes the regen more sensitive to injected energy variations [Fig. 91.10(b)].

We were able to inject pulses with energy as low as several picojoules, which yielded an $\sim 10^9$ regen overall gain. Regen energy stability was excellent: $<0.9\%$ rms fluctuations over a 24-h period [Fig. 91.11(a)]. It is worth noting that output-pulse-energy stability is higher at lower output energies [Fig. 91.11(b)].

We also measured the long-term stability of the output temporal pulse shape (Fig. 91.12). Temporal-pulse-shape variations did not exceed 1% rms over 5 h of operation. Temporal-pulse-shape stability is an extremely important driver-line parameter for OMEGA operations.

The regen beam profile was measured with an IR scientific-grade CCD camera with more than 1000:1 dynamic range and corresponded to a TEM₀₀ mode. The beam ellipticity over the beam above the 0.001 level was computed using a second-moment calculation method was 1.5% with no intracavity aperture and $<1\%$ with the intracavity aperture that supported the TEM₀₀ mode.

Conclusion

A highly stable, diode-pumped Nd:YLF regen for use in the OMEGA front-end laser system has been developed. This regen produces shaped optical pulses of up to 7-ns duration with low, $<0.9\%$ rms energy fluctuations for further amplification on OMEGA. Excellent temporal-pulse-shape stability and beam quality are the main advantages in comparison to previous designs.

ACKNOWLEDGMENT

This work was supported by the U.S. Department of Energy Office of Inertial Confinement Fusion under Cooperative Agreement No. DE-FC03-92SF19460 and the University of Rochester. The support of DOE does not constitute an endorsement by DOE of the views expressed in this article.

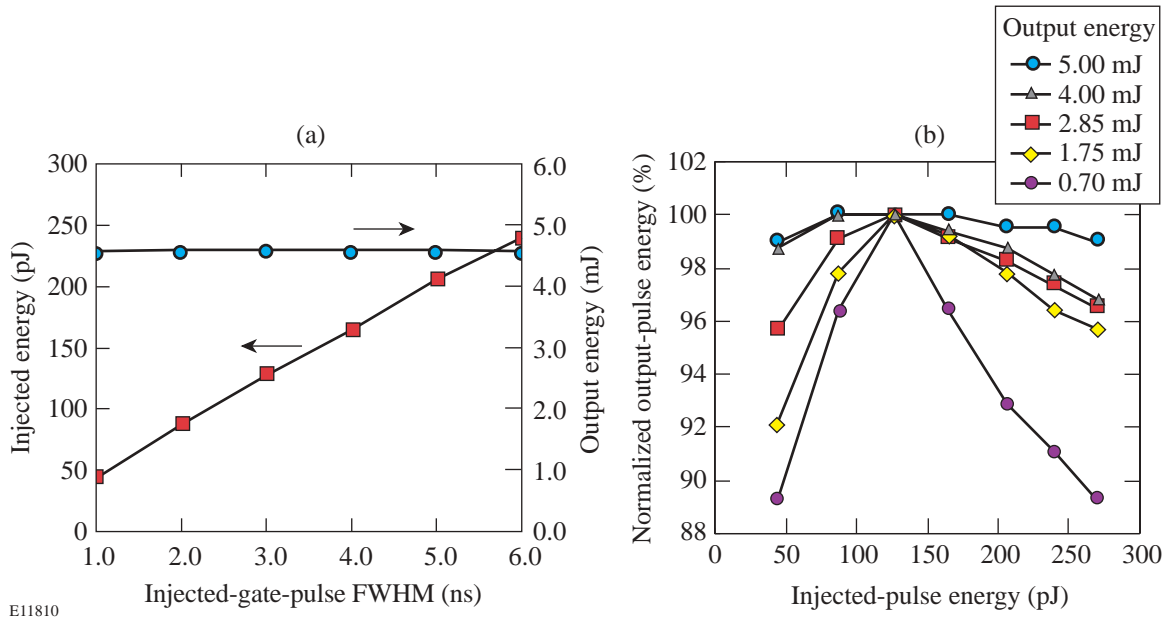


Figure 91.10

Regen output-pulse energy does not change with variations of injected-pulse energy, when (a) gain/loss ratio is high, and (b) becomes more sensitive to injected-pulse energy with decreasing gain/loss ratio. Note that the vertical scale of (b) is expanded to show the variation with input energy.

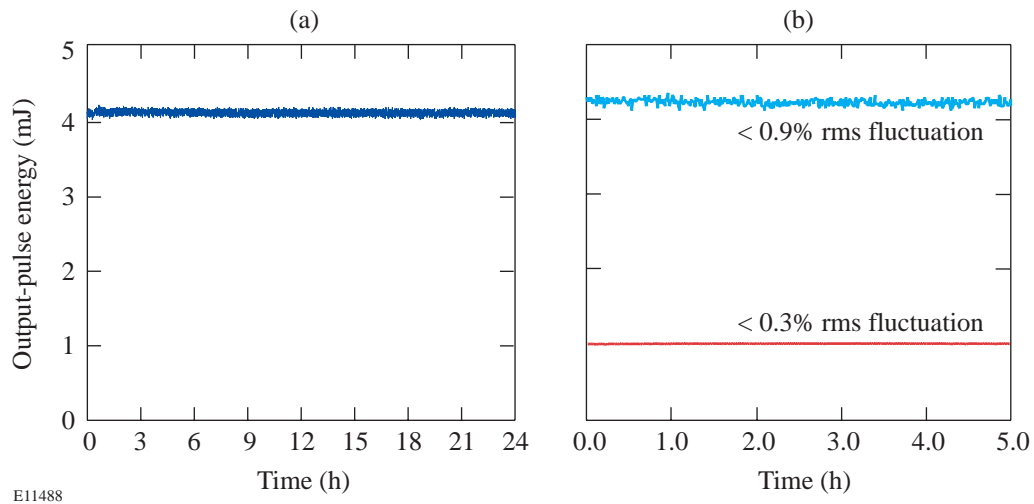


Figure 91.11
 (a) Regen output-pulse-energy stability is $<0.9\%$ rms over 24 h; (b) regen stability is higher at lower output energies.

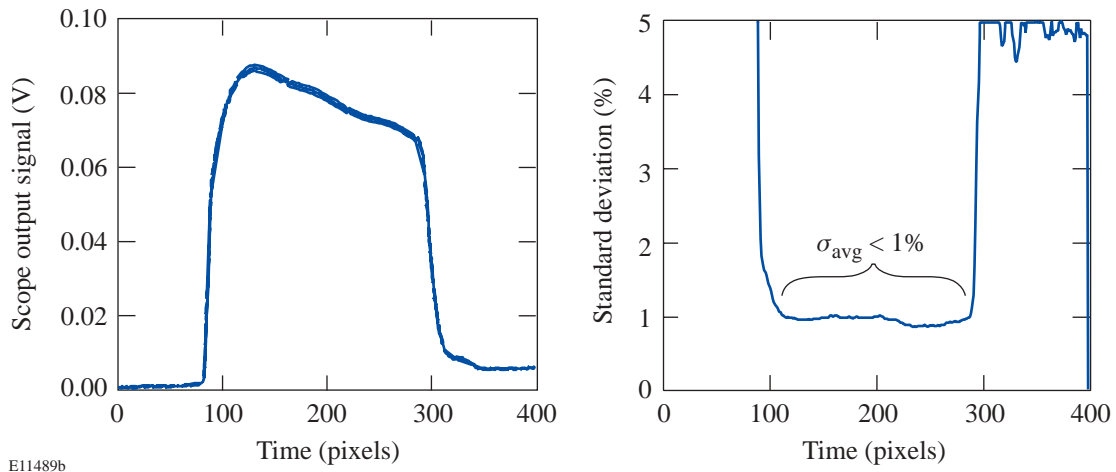


Figure 91.12
 Regen output-temporal-pulse-shape stability is excellent: pulse shape standard deviation is $<1\%$ over 5 h.

REFERENCES

1. A. V. Okishev, M. D. Skeldon, R. L. Keck, and W. Seka, in *Advanced Solid State Lasers*, edited by H. Injeyan, U. Keller, and C. Marshall, OSA Trends in Optics and Photonics Series (Optical Society of America, Washington, DC, 2000), Vol. 34, pp. 112–115.
2. D. L. Brown, I. Will, R. G. Roides, C. K. Merle, M. D. Skeldon, and W. Seka, in *1993 Optical Society of America Annual Meeting*, 1993 OSA Technical Digest Series, Vol. 16 (Optical Society of America, Washington, DC, 1993), p. 250.
3. A. Okishev, M. D. Skeldon, S. A. Letzring, W. Seka, and I. Will, in *OSA Proceedings on Advanced Solid-State Lasers*, edited by B. H. T. Chai and S. A. Payne (Optical Society of America, Washington, DC, 1995), Vol. 24, pp. 274–276.
4. M. D. Skeldon, A. Babushkin, W. Bittle, A. V. Okishev, and W. Seka, *IEEE J. Quantum Electron.* **34**, 286 (1998).
5. A. Babushkin, W. Bittle, S. A. Letzring, M. D. Skeldon, and W. Seka, in *Third International Conference on Solid State Lasers for Application to Inertial Confinement Fusion*, edited by W. H. Lowdermilk (SPIE, Bellingham, WA, 1999), Vol. 3492, pp. 124–130.
6. W. H. Lowdermilk and J. E. Murray, *J. Appl. Phys.* **51**, 2436 (1980).
7. J. E. Murray and W. H. Lowdermilk, *J. Appl. Phys.* **51**, 3548 (1980).

Improved Performance of Direct-Drive Implosions with a Laser-Shaped Adiat

Introduction

The minimum energy required for ignition of the imploding capsule in inertial confinement fusion is a strong function of the fuel adiabat (the ratio of the shell pressure to the Fermi-degenerate pressure) α_{stag} at the time of maximum compression: $E_{\text{min}} \sim \alpha_{\text{stag}}^3$. Thus, to minimize the energy, the shell must be driven on the lowest possible adiabat. The performance of low-adiabat implosions is limited by hydrodynamic instabilities that tend to disrupt the shell during the acceleration phase. The most important instability is the Rayleigh–Taylor^{1,2} (RT) instability seeded by single-beam non-uniformities and surface roughness. The main mechanism that reduces the RT growth is mass ablation from the target surface,³ characterized by the ablation velocity V_a . The ablation velocity, in turn, increases with the adiabat α in the ablation region as $V_a \propto \alpha^{3/5}$. As the shell accelerates, the RT instability takes place at the outer part of the shell, which ablates during the implosion. Thus, one can satisfy the requirements of the lower-adiabat fuel at the maximum compression and the higher-adiabat ablation region by shaping the adiabat inside the shell.

Experiments have been done in both planar^{4–8} and convergent^{9,10} geometries to understand the evolution of perturbations at the ablation surface during acceleration of a planar foil or implosion of a cylinder or hemisphere. The ablation surface and the shell–fuel surface are coupled in that perturbations on the shell–fuel interface can “feed out”¹¹ to the ablation surface and perturbations that grow on the ablation surface can “feed through”¹² to the shell–fuel interface.

Interface perturbations grow exponentially ($a = a_0 e^{\gamma t}$) during the “linear” phase of the RT instability and reach a saturation phase (when $a \sim \lambda/10$) where the growth continues at a reduced rate.¹³ Here, a is the amplitude of the perturbation, a_0 is the initial perturbation amplitude (the seed), γ is the growth rate, and λ is the wavelength of the perturbation.

A great deal of effort has gone into reducing the seeds (a_0) due to illumination nonuniformities (imprinting) and target imperfections. The effect of imprinting has been reduced by a

number of beam-smoothing techniques, including distributed phase plates (DPP’s),¹⁴ polarization smoothing (PS) with birefringent wedges,^{15,16} smoothing by spectral dispersion (SSD),¹⁷ and induced spatial incoherence (ISI).¹⁸ The effect of the RT instability can also be reduced by lowering the RT growth rate. It has been shown that the ablation-surface RT growth rate is reduced by the ablation process.³ Subsequent theoretical work that includes the effect of thermal transport¹⁹ and experiments with planar targets⁸ shows that the dispersion formula for a CH target is given by

$$\gamma = 0.98 \sqrt{\frac{kg}{1+kL}} - 1.7 \cdot kv_a,$$

where k is the perturbation spatial wave number, g is acceleration, L is density scale length, and V_a is ablation velocity.

The ablation velocity term not only reduces the growth rate but stabilizes the interface for perturbation wavelengths shorter than the cutoff wavelength λ_c , where

$$\lambda_c = \frac{4\pi L}{\sqrt{1 + 4 \left(\frac{0.98}{1.7}\right)^2 \times \frac{Lg}{V_a^2}}},$$

which, in the limit that $k \times L \ll 1$, is

$$\lambda_c = 2\pi \left(\frac{1.7}{0.98}\right)^2 \times \frac{V_a^2}{g}.$$

The ℓ mode of a perturbation on a spherical target is given approximately by the circumference of the target ($2\pi r$) divided by the perturbation wavelength, so that the cutoff ℓ mode $\ell_c \sim 2\pi r/\lambda_c$. A capsule is stable for modes equal to or larger than ℓ_c .

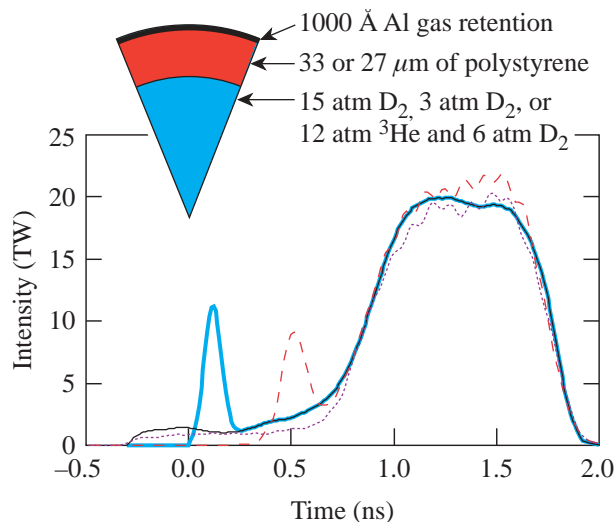
The ablation velocity is defined as the velocity at which the ablation surface moves into the target. This is given by the mass

ablation rate (the rate at which material is removed from the ablation surface) divided by the density of the same material. The mass ablation rate is determined by the intensity of the incident radiation onto the target; therefore, decreasing the density of material at the ablation surface can increase the ablation velocity.

Two techniques—radiation preheat²⁰ and driving a decaying shock wave²¹—have been proposed to decrease the density at the ablation surface by raising its temperature and causing the shell to decompress. Decreasing the density at the ablation surface increases the ablation velocity, the entropy of the ablation surface, and thus the adiabat. One must be careful, however, to increase the shell adiabat at the ablation surface only and not the whole shell or the fuel. The entropy of the fuel must be minimally affected by these techniques so that the target will continue to be compressed efficiently.

Adiabat Shaping in Spherical Implosions

An experiment was designed to test the technique of launching a decaying shock wave into a spherical shell, setting the adiabat of the shell high at the ablation surface and low at the fuel–shell interface. This was accomplished by adding a narrow picket pulse to the beginning of a laser pulse shape designed to implode a target with a low shell adiabat as shown by the thick solid curve of Fig. 91.13. The picket pulse initiates a shock wave in the shell that becomes unsupported in that the pressure at the ablation surface is decreased, resulting in the generation of a rarefaction wave that propagates toward the shock wave. The rarefaction wave overtakes the shock wave, and the resultant shock wave decays as it propagates through the shell. The laser-irradiation pulse shape is designed



E11794

so that the shock wave affects the ablation interface with minimal change at the shell–fuel interface.

The experiment was designed around a D₂-filled polystyrene shell, 33 μm thick and 905 μm in diameter filled to a pressure of 15 atm. Two pulse shapes (shown in Fig. 91.13) were used to compress this shell with a low adiabat ($\alpha = 2$) at the fuel–shell interface. The main drive pulse, shown as the thin solid curve, has a 2-TW, 700-ps-long foot followed by a power law rise²² to a peak intensity of 20 TW on target. The foot pulse drives a shock wave that is fully supported throughout the implosion and changes the entropy of the shell and fuel. The dotted curve in Fig. 91.13 shows an actual pulse shape used during the experiments.

The optimum picket pulse is one that will raise the adiabat of the ablation surface without affecting, or minimally affecting, the fuel–shell interface adiabat. It was found by one-dimensional (1-D) hydrodynamic simulations that this optimum pulse for the implosions with a picket pulse was comprised of a narrow, 100-ps-FWHM (full width at half maximum), Gaussian picket combined with the main drive pulse described above. This combined pulse, shown as the thick solid curve in Fig. 91.13, has a picket 750 ps before the half-maximum intensity point of the power-law rise of the drive pulse. The narrowest picket pulse available on OMEGA for these experiments had a FWHM of 120 ps. The experiment was designed with a pulse using a 120-ps picket placed at 340 ps before the half-maximum point of the compression pulse shown as the dashed curve in Fig. 91.13. The total laser energy on target is 19 kJ with 0.9 kJ in the picket pulse.

Figure 91.13

(Inset: Types of targets used to study the effect of a picket pulse on the implosion of a spherical gas-filled shell. Targets with either a 33-μm- or 27-μm-thick polystyrene shell were filled with either 15 atm of D₂, 3 atm of D₂, or a mixture of 12 atm of ³He and 6 atm of D₂.) Pulse shape used to measure the effect of a picket pulse before a drive pulse on the performance of an implosion. The drive pulse was designed to implode a spherical cryogenic DT target on an isentrope. This pulse shape implodes a gas-filled CH shell as an $\alpha = 2$ isentrope. This pulse shape is shown as the thin solid curve (which is covered by the thick solid curve after 0.25 ns). The actual pulse shape delivered by the laser is shown as the dotted curve. The optimum picket pulse has an intensity of 55% of the drive pulse intensity, is 100 ps wide between the half-intensity points, and precedes the compression pulse by 750 ps. This pulse shape is shown as the thick solid curve. The actual picket was 120 ps wide so it had to be positioned 340 ps ahead of the drive pulse with an amplitude of 40% of the drive pulse. The actual picket and drive pulse combination used is shown as the dashed curve.

The effect of the picket on the implosions is shown in Figs. 91.14 and 91.15. Stability was calculated using the output from the 1-D hydrodynamics simulation code *LILAC*.²³ The calculation uses *LILAC* output to determine values for the shell's physical quantities, an assumed initial perturbation spectrum at the ablation surface, and a model for RT growth¹² to determine the amplitude of perturbations at the ablation surface during an implosion. The initial perturbation is a quadrature sum of the illumination nonuniformity as calculated by a two dimensional (2-D) hydrodynamics simulation and the measured target outer-surface roughness.²⁴ The amplitude of the inner peak, or bubble, of the perturbation divided by the shell thickness is shown in Fig. 91.14. It is assumed that the perturbation disrupts the shell when this value is equal to 1. For

the case of the pulse shape without a picket (shown as the thick solid curve), this occurs at the peak of the compression pulse at 1.28 ns. The thin solid curve in Fig. 91.14 shows the result when a picket is added to the beginning of the compression pulse. The bubble-to-shell thickness ratio stays below 1 during the entire time that the laser irradiates the target, reaching a maximum value of 0.7 near the end of the compression pulse. This analysis indicates that the shell driven with a picket pulse is more stable during the acceleration phase of the implosion than one driven without a picket.

Figure 91.15 shows the simulated shell density and adiabat as functions of radius at the time of maximum acceleration for two separate implosions. Densities are plotted as solid curves,

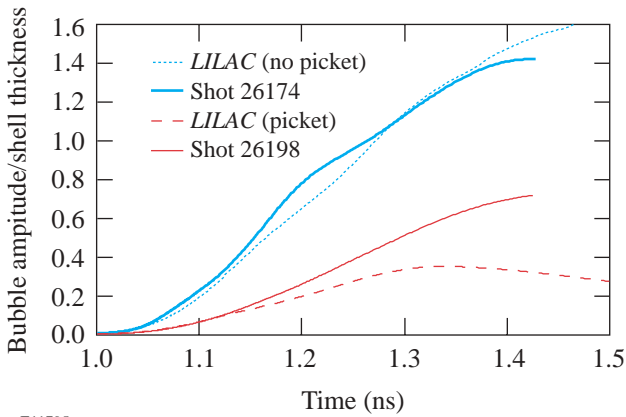


Figure 91.14
Bubble amplitude divided by the shell thickness calculated by a stability postprocessor applied to the output from the 1-D hydrodynamic simulation *LILAC*. The thick and dotted curves indicate the laser pulse without a picket. The thin and dashed curves indicate pulse shapes with a picket. The dashed and dotted curves indicate the ideal pulse shape for a 15-atm-D₂-filled, 33- μ m-thick polystyrene shell. The thick and thin curves are calculated for the actual pulse shapes delivered onto the target.

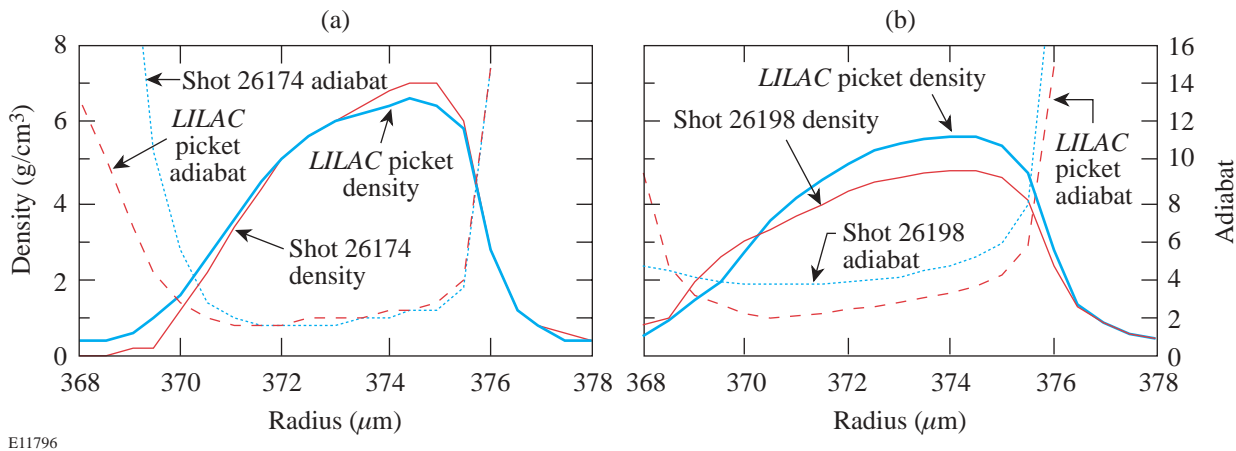


Figure 91.15
The density and adiabat versus position at the time of peak acceleration calculated from *LILAC*. In (a) with the drive pulse only, the density is plotted as solid lines, and the adiabat is plotted as broken lines. In (b) the density and adiabat are plotted with a picket pulse added to the compression pulse. The thick and dashed lines in both (a) and (b) are calculated from *LILAC* for the optimum laser pulse shapes. The thin and dotted lines are calculated for the pulse shape used in the experiment.

and the adiabats are plotted as dashed curves. Figure 91.15(a) shows the results for illumination without a picket for both the ideal and actual pulse shapes, and Fig. 91.15(b) shows the results for pulses with a picket, again for both the ideal and actual pulse shapes. The ablation surface is at the position of $376\ \mu\text{m}$, where the density is $2.5\ \text{g}/\text{cm}^3$. The value of the adiabat at the ablation surface without a picket is 3.9 and with a picket is 5.6. The fuel-shell interface is at a position of $372\ \mu\text{m}$ for the pulse shape without a picket and $370\ \mu\text{m}$ for illumination with a picket. The value of the adiabat is 1.7 for pulses without a picket and 2.1 for pulses with a picket.

Experimental Results

The OMEGA²⁵ laser system was used to implode spherical targets with the above pulse shapes. Sixty beams of 351-nm radiation were incident onto the target. All beams had polarization smoothing, 1-THz bandwidth, 2-D SSD, and DPP's with an intensity envelope given by a third-order super-Gaussian to minimize the illumination nonuniformities imposed by the laser. The targets used for these measurements are shown as the inset in Fig 91.13. The shells were made of polystyrene either 33 or 27 μm thick and filled with three gas-fill conditions: 15 atm of D_2 ; 3 atm of D_2 ; and a mixture of 12 atm of ^3He and 6 atm of D_2 . All targets had a 1000-Å layer of aluminum to act as a gas-retention barrier. The laser pulse shapes were optimized for an outer diameter of 906 μm , and the delivered targets had diameters that ranged from 901 to 923 μm .

Both x-ray and fusion particle (neutron and proton) diagnostics were used to measure and quantify the implosions. X-ray framing cameras²⁶ were used to measure the time and spatially dependent x-ray emission during the implosion. X-ray microscopes²⁷ were used to study the final core spatial

shapes. Neutron yields and spectra were measured with scintillator time-of-flight counters^{28–30} at 3.5 and 7 m from the center of the target chamber. Protons from fusion processes were detected with range filters³¹ designed to determine both their yield and energy spectrum.

It is important that the 1-D hydrodynamic simulation calculate the implosion dynamics correctly when a model is used to determine the growth of perturbations. Two x-ray framing cameras were used to measure the radius of the imploding shell as a function of time. The data for all 15-atm-gas-filled, 33- μm -thick CH shells are plotted in Fig. 91.16. These data are from 15-atm- D_2 -filled and 12-atm- $^3\text{He}/6\text{-atm-}\text{D}_2$ -filled targets. The experimental data are the value of the peak x-ray emission radius of a two-dimensional image and are plotted as crosses. The *LILAC*-calculated position of the outer and inner shell surfaces are plotted as solid and dashed lines. The inner and outer shell radii are determined by radii at which the density is $1/e$ times the peak density of the shell. Data for laser irradiation without the picket pulse are plotted in Fig. 91.16(a), and data for laser irradiation with the picket are plotted in Fig. 91.16(b). The *LILAC* calculations agree reasonably well with the experimental data. This indicates that the motion of the imploding target is calculated correctly.

X-ray images of the core emission from a Kirkpatrick–Baez (KB) microscope are shown in Fig. 91.17. These images are integrated in time; however, most of the x-ray emission from the core comes during the peak compression of the target. The image from an implosion without a picket pulse is shown in Fig. 91.17(a), and the image from an implosion with a picket pulse is shown in Fig. 91.17(b). The images show a more-intact fuel mass when a picket pulse is added to the main compres-

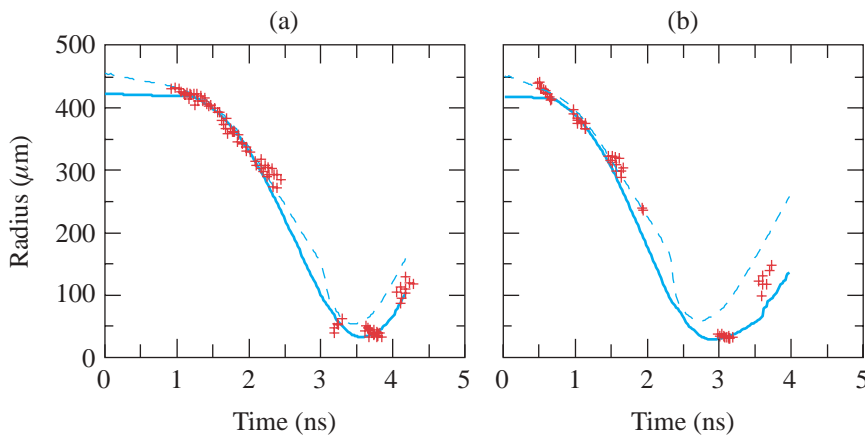


Figure 91.16

Radius versus time for all 15-atm-filled, 33- μm -thick CH shell targets. The plot in (a) shows data for laser irradiation using the compression pulse without a picket pulse. Averages for *LILAC*-calculated position of the inner and outer shell radius are plotted as solid and dashed lines, and the experimental data as measured with two x-ray framing cameras are plotted as crosses. The plot in (b) shows data taken with a picket pulse. The solid and dashed curves are averages of the *LILAC*-calculated positions of the inner and outer shell radius. The experimental data as measured with x-ray framing cameras are plotted as crosses.

E11797

sion pulse. Lineouts along the lines shown in the images are plotted in Fig. 91.17(c). The lineout of the image without a picket pulse is plotted as a dashed curve. Lineout data from the image with a picket pulse are plotted as the solid line. Figure 91.17(c) shows that the lineout from the implosion with a picket is typical of that from a “limb-brightened” image and shows that the implosion was more stable than the implosion without a picket.

Results from the fusion-product-yield measurements for three shots for each target and pulse shape are shown in Table 91.I. It can be seen from the data that for the 15-atm-D₂-filled, 33- μ m-thick shell, there is a factor-of-3 increase in the number of 3-MeV neutrons from the target irradiated with a picket pulse than that from the target without a picket. The experiment was optimized for the 33- μ m-thick shells; the improvement for the 27- μ m-thick shells is only 50%. Both the 3-atm-D₂-filled and the ³He-D₂-filled, 33- μ m-thick shells show an improved fusion yield by a factor of 2. The ratio of the measured primary neutron yield to the neutron yield predicted by the hydrodynamics simulation [usually referred to as yield-over-clean (YOC)] for the 15-atm-D₂-filled, 33- μ m-thick shells improves from 0.03 to 0.19. In all cases, the YOC can be seen to improve significantly.

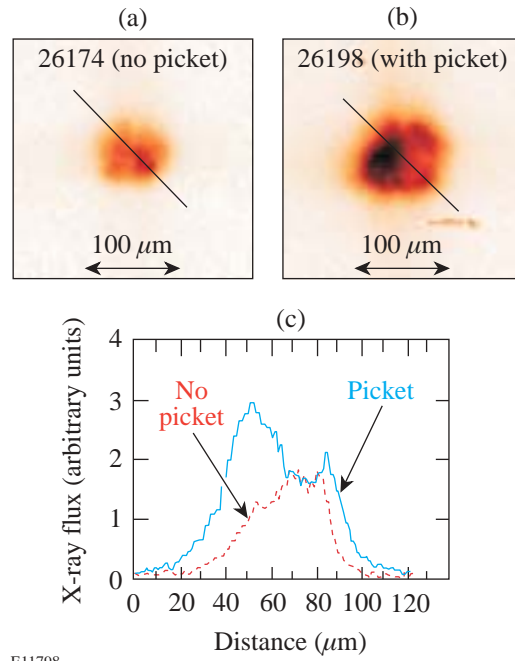


Figure 91.17

X-ray microscope images of target cores formed from a 33- μ m-thick CH shell filled with 15 atm of D₂; (a) with only the main compression pulse used; (b) when a picket pulse was added to the compression pulse. Lineouts through the images are shown in (c). The dashed line is the lineout without a picket pulse; the solid line is the lineout with a picket pulse.

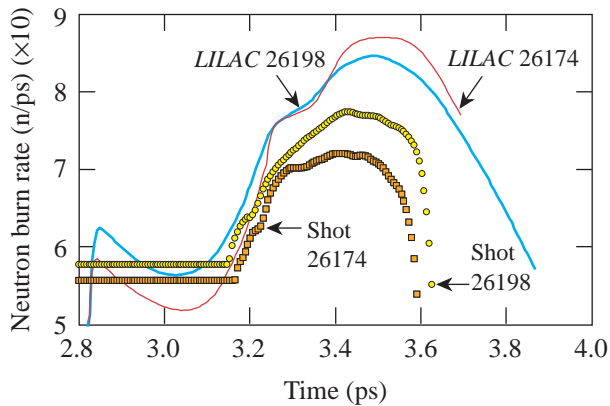
Table 91.I: Summary of fusion-product measurements and simulation output. The first column describes the composition, shell thickness (mm, in square brackets), and fill pressure (atm, in parentheses) of the target.

Target	Experimental Measurements			LILAC Simulation Output		
	Yield (D ₂)	Yield (DT)	Yield (D ³ He)	Yield (D ₂)	Yield (DT)	Yield (D ³ He)
Without picket						
D ₂ (15)CH[33]	4.14 × 10 ⁹	7.99 × 10 ⁶	2.96 × 10 ⁶	1.17 × 10 ¹¹	3.04 × 10 ⁸	1.66 × 10 ⁸
D ₂ (3)CH[33]	1.06 × 10 ⁹	8.00 × 10 ⁵	1.83 × 10 ⁶	4.17 × 10 ¹⁰	9.51 × 10 ⁷	6.34 × 10 ⁷
³ He(12)D ₂ (6)CH[33]	9.32 × 10 ⁸	9.30 × 10 ⁵	2.94 × 10 ⁶	1.54 × 10 ¹⁰		
D ₂ (15)CH[27]	1.98 × 10 ¹⁰	3.89 × 10 ⁷	1.83 × 10 ⁷	2.50 × 10 ¹¹	6.60 × 10 ⁸	4.18 × 10 ⁸
With picket						
D ₂ (15)CH[33]	1.27 × 10 ¹⁰	3.57 × 10 ⁷	7.26 × 10 ⁶	6.60 × 10 ¹⁰	1.20 × 10 ⁸	8.12 × 10 ⁷
D ₂ (3)CH[33]	1.98 × 10 ⁹	1.83 × 10 ⁶	1.88 × 10 ⁶	1.19 × 10 ¹⁰	1.36 × 10 ⁷	1.15 × 10 ⁷
³ He(12)D ₂ (6)CH[33]	1.44 × 10 ⁹	1.77 × 10 ⁶	5.75 × 10 ⁶	8.20 × 10 ⁹		
D ₂ (15)CH[27]	2.96 × 10 ¹⁰	5.22 × 10 ⁷	2.96 × 10 ⁷	1.94 × 10 ¹¹	4.15 × 10 ⁸	3.05 × 10 ⁸

Neutron-production rates for the 15-atm-D₂-filled, 33- μm -thick shell, measured (open symbols) and predicted (solid curves), are shown in Fig. 91.18. The thin curve and open square plots are data from the implosion without a picket. The thick curve and open circle plots are from the matching implosion using a picket. The experimental data were measured with the “neutron temporal diagnostic” (NTD).³² The temporal offsets needed to compare experimental and simulation data were determined by maximizing the cross-correlation of the drive portion of the pulse as a function of a temporal shift relative to the laser pulse without a picket. This aligned the leading edges of the main drive pulse for all of the data. It is assumed that the neutron production is determined by the compression of the target by the drive pulse. An additional time shift was introduced to align the position of the shock neutron production calculated by *LILAC* for shapes without and with the picket pulse. The experimental data and the output from hydrodynamic simulations were processed in this manner so that the timing could be compared for all data. The temporal error for the relative times of emission is estimated to be of the order of 30 ps. The measured neutron burn rate divided by the calculated neutron burn rate from *LILAC* is plotted in Fig. 91.19. The data from implosions without a picket are plotted as open squares, and the data from implosions with a picket are plotted as open circles. The ratio of burn rates peaks

at 0.35 for implosions with a picket pulse, while the ratio without a picket pulse peaks at 0.2. The neutron-burn-rate ratios show that the duration of neutron emission is longer for implosions with a picket pulse. Comparing the experimental data with predictions indicates that the implosions using a picket not only attain higher absolute yields than the implosions without a picket, they also return, as was stated earlier, a larger fraction of the 1-D yield. This suggests more-stable implosions with less mix due to RT growth.

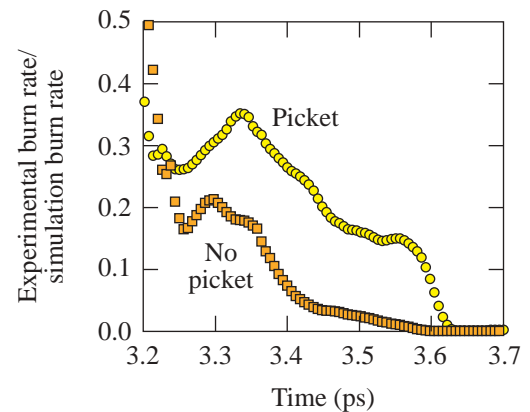
While the experimental results from the neutron diagnostics reported above are encouraging, results from several other diagnostics remain inconclusive. Ion temperatures, inferred from the broadening of the neutron spectra, were reported to be from 2.1 to 2.5 \pm 0.5 keV for the 33- μm -thick shells and from 2.6 to 2.8 \pm 0.5 keV for the 27- μm -thick shells. There were no appreciable differences between implosions using the laser pulses with or without the picket. Additionally, the downshift of the primary proton energy can be used to measure the total ρR of the target integrated over the time of proton emission. The measured mean energy for the compression yield was 11.3 \pm 2.0 MeV for the implosion without a picket and 11.6 \pm 1.8 MeV for the implosion with a picket. The total ρR for both of these targets was inferred to be 106 \pm 8 and 108 \pm 8 mg/cm², respectively.



E11799

Figure 91.18

Neutron-production rates for a 15-atm-D₂-filled, 33- μm thick polystyrene shell. The thin curve and open squares are data for the pulse without a picket pulse. The thick curve and open circles are data for the pulse with a picket in front. Open symbols are the experimental measurements, and the solid curves are from the 1-D hydrodynamic simulation *LILAC*. Note that these points lie very close together before \sim 3.2 ns.



E11800

Figure 91.19

Experimental neutron-production rate divided by the neutron-production rate from a 1-D hydrodynamic simulation *LILAC* for a 15-atm-D₂-filled, 33- μm -thick polystyrene shell. The open square points are data for the pulse without a picket pulse, and the open circle points are data for the pulse with a picket in front.

Finally, results from the measurements of the 14.7-MeV proton emitted from the D^3He reaction are shown in Table 91.II. Targets filled with D^3He allowed for the measurement of the primary proton yield from the shock wave convergence at the center of the capsule. The mean energy for the protons was measured as 14.3 MeV for the laser irradiation both without and with a picket pulse. The number of protons from the shock wave is $7.1 \pm 1.2 \times 10^5$ without a picket pulse and $7.5 \pm 1.1 \times 10^5$ with a picket pulse as shown in column 2 of Table 91.II. Comparison of these measurements infer that the shock strength of the compression pulse is unaffected by the introduction of a picket. This would indicate that the shock created by a picket decayed in the shell before it had a chance to significantly alter the adiabat of the fuel.

Conclusion

An experiment has been performed to measure the effect of a picket pulse on the implosion of a spherical target. The purpose of this pulse was to initiate a decaying shock wave that lowers the density of the shell at the ablation interface but does not significantly affect the entropy of the shell–gas interface. The yields of fusion products are improved both in terms of the absolute value and in terms of the comparison to 1-D hydrodynamic simulation output. The increase in neutron yield for implosions with a picket pulse is not due to the added energy in the picket since both the absolute and relative neutron yields improved.

Between the two pulse shapes there is little change in either the total target ρR or the ion temperature. The neutron temperature measurement is the neutron-weighted ion temperature. It is possible this weighted measurement will be the same for both types of implosions. The ρR as measured with the protons from the D^3He reaction measures the total ρR of the target and not just the fuel ρR . This measurement is dominated by the thick target shells and is less sensitive to the fuel.

The emission rate for the 3-MeV neutrons compared to the simulation output shows that the start of emission calculated by the simulation compares well with the experimental data. The neutron-burn-rate measurements indicate that the 1-D simulation overestimates the duration of the neutron emission, probably due to the multidimensional effects not included in this type of calculation. The neutron emission from implosions using a picket pulse reaches a higher emission rate and a higher ratio of the experimental neutron burn rate to the *LILAC*-calculated neutron burn rate. Comparing the experimental data with predictions indicates that the implosions using a picket not only attain higher absolute yields than the implosions without a picket, they also return, as was stated earlier, a larger fraction of the 1-D yield. This demonstrates that picket pulses stabilize the implosion, resulting in less mix due to the RT growth at the ablation interface.

Table 91.II: Summary of 14-MeV proton measurements. The first column describes the target as in Table 91.I. The second column is the total number of protons emitted during the compression of the target. Column 3 is the number of protons emitted when the shock wave reaches the center of the target. The downshift of the protons is shown in column 4, and the calculated total ρR of the target is shown in column 5.

Target	Proton measurements		ΔE MeV	ρR_{total} mg/cm ²
	Yield (D ³ He) Compression	Yield (D ³ He) Shock		
Without picket				
D ₂ (15)CH[33]	2.96×10^6		3.5 ± 0.3	106 ± 8
He ³ (12)D ₂ (6)CH[33]	2.94×10^6	7.11×10^5	3.4 ± 0.3	104 ± 8
D ₂ (15)CH[27]	1.83×10^7		2.6 ± 0.2	81 ± 6
With picket				
D ₂ (15)CH[33]	7.26×10^6		3.6 ± 0.3	108 ± 8
He ³ (12)D ₂ (6)CH[33]	5.75×10^6	7.51×10^5	3.5 ± 0.2	106 ± 6
D ₂ (15)CH[27]	2.96×10^7		3.0 ± 0.2	92 ± 6

ACKNOWLEDGMENT

This work was supported by the U.S. Department of Energy Office of Inertial Confinement Fusion under Cooperative Agreement No. DE-FC03-92SF19460 and the University of Rochester. The support of DOE does not constitute an endorsement by DOE of the views expressed in this article.

REFERENCES

1. Lord Rayleigh, Proc. London Math Soc. **XIV**, 170 (1883).
2. G. Taylor, Proc. R. Soc. London Ser. A **201**, 192 (1950).
3. S. E. Bodner, Phys. Rev. Lett. **33**, 761 (1974).
4. J. Grun *et al.*, Phys. Rev. Lett. **58**, 2672 (1987).
5. M. Desselberger *et al.*, Phys. Rev. Lett. **65**, 2997 (1990).
6. S. G. Glendinning, S. V. Weber, P. Bell, L. B. Da Silva, S. N. Dixit, M. A. Henesian, D. R. Kania, J. D. Kilkenny, H. T. Powell, R. J. Wallace, P. J. Wegner, J. P. Knauer, and C. P. Verdon, Phys. Rev. Lett. **69**, 1201 (1992).
7. C. J. Pawley *et al.*, Phys. Plasmas **6**, 565 (1999).
8. J. P. Knauer, R. Betti, D. K. Bradley, T. R. Boehly, T. J. B. Collins, V. N. Goncharov, P. W. McKenty, D. D. Meyerhofer, V. A. Smalyuk, C. P. Verdon, S. G. Glendinning, D. H. Kalantar, and R. G. Watt, Phys. Plasmas **7**, 338 (2000).
9. W. W. Hsing *et al.*, Phys. Plasmas **4**, 1832 (1997).
10. C. Cherfils *et al.*, Phys. Rev. Lett. **83**, 5507 (1999).
11. R. Betti, V. Lobatchev, and R. L. McCrory, Phys. Rev. Lett. **81**, 5560 (1998).
12. V. N. Goncharov, P. McKenty, S. Skupsky, R. Betti, R. L. McCrory, and C. Cherfils-Clérouin, Phys. Plasmas **7**, 5118 (2000).
13. S. W. Haan, Phys. Rev. A **39**, 5812 (1989).
14. T. J. Kessler, Y. Lin, J. J. Armstrong, and B. Velazquez, in *Laser Coherence Control: Technology and Applications*, edited by H. T. Powell and T. J. Kessler (SPIE, Bellingham, WA, 1993), Vol. 1870, pp. 95–104.
15. Y. Kato, unpublished notes from work at LLE, 1984.
16. T. R. Boehly, V. A. Smalyuk, D. D. Meyerhofer, J. P. Knauer, D. K. Bradley, R. S. Craxton, M. J. Guardalben, S. Skupsky, and T. J. Kessler, J. Appl. Phys. **85**, 3444 (1999).
17. S. Skupsky, R. W. Short, T. Kessler, R. S. Craxton, S. Letzring, and J. M. Soures, J. Appl. Phys. **66**, 3456 (1989).
18. R. H. Lehmburg and S. P. Obenschain, Opt. Commun. **46**, 27 (1983).
19. R. Betti, V. N. Goncharov, R. L. McCrory, P. Sorotokin, and C. P. Verdon, Phys. Plasmas **3**, 2122 (1996).
20. D. G. Colombant *et al.*, Phys. Plasmas **7**, 2046 (2000).
21. J. D. Lindl and W. C. Mead, Phys. Rev. Lett. **34**, 1273 (1975).
22. R. E. Kidder, Nucl. Fusion **16**, 3 (1976).
23. M. C. Richardson, P. W. McKenty, F. J. Marshall, C. P. Verdon, J. M. Soures, R. L. McCrory, O. Barnouin, R. S. Craxton, J. Delettrez, R. L. Hutchison, P. A. Jaanimagi, R. Keck, T. Kessler, H. Kim, S. A. Letzring, D. M. Roback, W. Seka, S. Skupsky, B. Yaakobi, S. M. Lane, and S. Prussin, in *Laser Interaction and Related Plasma Phenomena*, edited by H. Hora and G. H. Miley (Plenum Publishing, New York, 1986), Vol. 7, pp. 421–448.
24. P. W. McKenty, V. N. Goncharov, R. P. J. Town, S. Skupsky, R. Betti, and R. L. McCrory, Phys. Plasmas **8**, 2315 (2001).
25. T. R. Boehly, D. L. Brown, R. S. Craxton, R. L. Keck, J. P. Knauer, J. H. Kelly, T. J. Kessler, S. A. Kumpan, S. J. Loucks, S. A. Letzring, F. J. Marshall, R. L. McCrory, S. F. B. Morse, W. Seka, J. M. Soures, and C. P. Verdon, Opt. Commun. **133**, 495 (1997).
26. O. L. Landen *et al.*, in *Ultra-high- and High-Speed Photography, Videography, and Photonics '93*, edited by P. W. Roehrenbeck (SPIE, Bellingham, WA, 1993), Vol. 2002, pp. 2–13.
27. F. J. Marshall and Q. Su, Rev. Sci. Instrum. **66**, 725 (1995).
28. T. J. Murphy *et al.*, Rev. Sci. Instrum. **66**, 930 (1995).
29. R. A. Lerche and T. J. Murphy, Rev. Sci. Instrum. **63**, 4880 (1992).
30. V. Yu. Glebov, D. D. Meyerhofer, C. Stoeckl, and J. D. Zuegel, Rev. Sci. Instrum. **72**, 824 (2001).
31. F. H. Séguin, C. K. Li, D. G. Hicks, J. A. Frenje, K. M. Green, R. D. Petrasso, J. M. Soures, D. D. Meyerhofer, V. Yu. Glebov, C. Stoeckl, P. B. Radha, S. Roberts, C. Sorce, T. C. Sangster, M. D. Cable, S. Padalino, and K. Fletcher, Phys. Plasmas **9**, 2725 (2002).
32. R. A. Lerche, D. W. Phillion, and G. L. Tietbohl, Rev. Sci. Instrum. **66**, 933 (1995).

Direct-Drive Implosion Experiments with Enhanced Beam Balance on OMEGA

Introduction

Laser-driven, direct-drive inertial confinement fusion (ICF) is accomplished by near-uniform illumination of spherical fuel-bearing targets with high-power laser beams.^{1–3} A goal of ICF is to achieve thermonuclear ignition and gain, which requires symmetric compression of the fuel to high temperatures (≥ 4 keV) and high areal densities (≥ 0.3 g/cm²). Both target imperfections and departures from symmetric laser illumination contribute to degradation of target performance. Low-mode ($\ell \leq 10$) perturbations of the intensity, generally due to beam-to-beam variations, can cause distortions of the core at stagnation; whereas small-scale imperfections in the target layers and in the single-beam intensity profiles contribute to higher-mode ($\ell \geq 10$) perturbations, which lead to Rayleigh–Taylor unstable growth, target breakup, and mixing of material from the shell and from the gas fill. Both can degrade target performance by reducing the peak temperature and areal density of the final fuel region.

Direct-drive ICF implosion experiments are currently being performed on LLE’s OMEGA laser system.⁴ The goal of these experiments is to attain near-ignition conditions in the compressed fuel region. Implosion experiments are being performed with both surrogate cryogenic targets^{5,6} (where the shell acts as the main fuel layer) and actual cryogenic targets⁷ (where the shell is principally solid fusion fuel). The cryogenic targets are being prepared by the newly implemented Cryogenic Target Handling System⁸ using D₂ as the fuel layer. The eventual goal is to demonstrate optimized implosions of cryogenic DT-fuel targets. Studies of the performance of surrogate fuel targets have shown that the smoothness of the individual beams has a measurable effect on target performance;^{5,6} however, the effect of beam balance on the target performance has not been quantified.⁶

This article presents a method that measures the beam-to-beam intensity variations at the target and then uses these measurements to correct the beam intensities, thereby minimizing the variations. The beam-to-beam UV intensity variations at the target are inferred from measurements of the x-ray

flux produced by each of the 60 beams of OMEGA seen separated on a 4-mm-diam, Au-coated spherical “pointing” target. Up to eight x-ray pinhole camera (XPHC) images are electronically recorded per shot from which variations in intensity are determined, taking into account view-angle effects and x-ray conversion efficiency dependence on intensity. The observed variations are then used to correct the beam intensities to produce more-uniform irradiation (or enhanced beam balance). The enhanced beam balance condition is in contrast to the standard beam balance condition arrived at by balancing the output of the laser as measured by 60 cross-calibrated full-beam calorimeters. As applied to imploding targets, the enhanced balance condition consistently yields improved symmetry of the imploding shell as observed by multiple-view x-ray imaging diagnostics. This is evidence of a more-uniform final fuel layer in the imploding target, an important goal for eventual attainment of ignition and gain.

Measurement of On-Target Intensity Using X-Ray Imaging

To accurately determine the intensity of a beam striking a laser target, it is necessary to be able to measure the full-beam intensity and/or energy before focusing and then to account for all losses incurred in transporting the beam to the target. In addition, the beam profile at its focus must be known. OMEGA uses distributed phase plates and spectrally dispersed frequency modulation to produce a time-averaged intensity pattern at the target, which is smoothed in space [smoothing by spectral dispersion (SSD)].⁹ The SSD version currently in use on OMEGA smooths the beam in two dimensions with an effective bandwidth of 1 THz and is enhanced by the use of polarization smoothing (PS).¹⁰ The smoothed beam instantaneously has a so-called super-Gaussian shape given by

$$I_{UV}(r) = I_{UV}(0) \times e^{-(r/\sigma_r)^\eta}, \quad (1)$$

where $I_{UV}(0)$ is the intensity at the beam peak, and r and σ_r are in units of distance from the beam center. Typical values for OMEGA 1-THz-SSD-with-PS beams are $\sigma_r = 300$ μm and $\eta = 2.5$.

Since the integral of Eq. (1) over time and space yields the beam energy, it is easy to see that for beams of equal size (i.e., equal σ_r and η) a measurement of the beam's peak intensity is sufficient to measure the beam energy. Here, advantage is being taken of the high UV-absorption efficiency of Au at high intensities (>90% for intensities below 10^{13} W/cm²).¹¹ Inverse-bremsstrahlung-heated Au plasmas reradiate most of their energy in the soft x-ray range (1 to 10 keV), making it possible to image the emission and, with knowledge of the x-ray conversion efficiency, to infer the UV intensity that produced the observed x-ray flux. Phenomenologically, the x-ray flux resulting from an incident intensity I_{UV} can be expressed as

$$I_x = C_{UV-x} \times I_{UV}^\gamma, \quad (2)$$

where C_{UV-x} is a constant dependent upon the x-ray band (energy range) and detection method utilized (see Subsection 3).

Spherical targets coated with Au have been used to verify beam alignment on OMEGA since target experimental operations began.¹² This method can determine the beam placement to an accuracy of $\sim 10 \mu\text{m}$. It has been noted for some time that although beam energies have been made to be nearly equal at the output of the laser, intensities on target appear to differ significantly. Figure 91.20 shows an x-ray image from a pointing target recorded by a charge-injection-device (CID), x-ray-sensitive camera¹³ at the image plane of an x-ray pinhole

camera. (The pinhole cameras use $10\text{-}\mu\text{m}$ -diam pinholes at a distance of 164 mm and a magnification of 4.0. The CID cameras have $38.5\text{-}\mu\text{m}$ -sq pixels, giving a resolution at the target of $\sim 12 \mu\text{m}$.) The pinholes themselves are covered with a $101.6\text{-}\mu\text{m}$ -thick Be foil with an additional $50.8 \mu\text{m}$ of Be between the pinhole and the detector acting as a vacuum window and a light shield for the camera. The camera sensitivity and window transmission provide for an effective energy band with a minimum of ~ 2 keV and falling sensitivity above 4 keV (see Ref. 13 for further details). Two of the beams at the center of the image have been highlighted (beams 4-2 and 4-4), and lineouts through the images are shown. Despite the fact that the beam energies are reported to be nearly equal, the peak x-ray intensities are seen to differ by a factor of ~ 2 . This suggests that either the reported energies are in error or other factors, such as beam size on target or unaccounted-for losses, differ significantly for these two beams. (These two beams were chosen since from this view the beams are at the same angle to the view direction normal; any angular effects on the observed intensity should therefore be equal.) The following method is suggested by images obtained on beam-pointing shots: Measure the beam intensities on target using a set of cross-calibrated x-ray cameras; correct the observed intensities for view-angle effects and conversion-efficiency dependence. The incident-beam-intensity variations can then be determined. Once these corrections are determined, the beam-to-beam intensity differences can then be reduced, resulting in more nearly spherical implosions. This technique and its application and results are the subject of the remainder of this article.

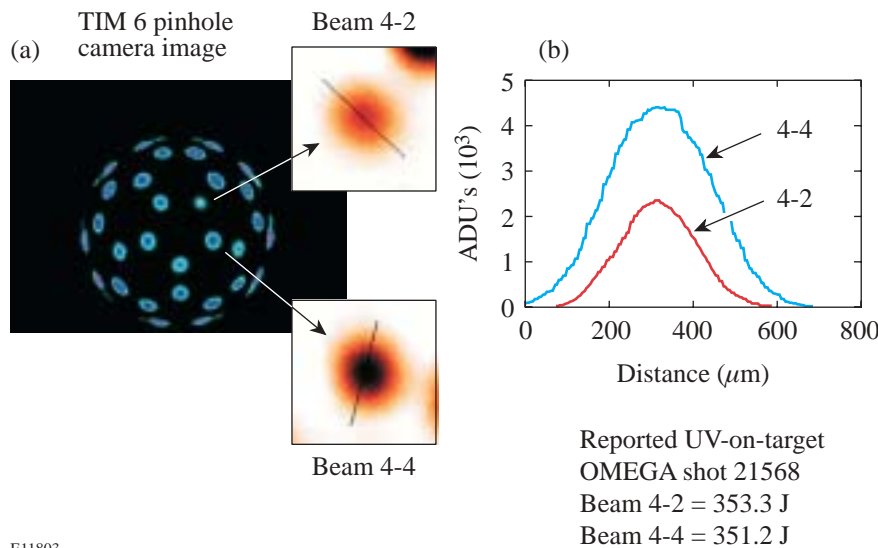


Figure 91.20

(a) TIM (ten-inch manipulator)-based pinhole camera image of a 4-mm-diam, Au-coated pointing target taken with a CID camera. Beams 4-2 and 4-4 are shown in enlarged insets. (b) Lineouts through the x-ray beam spots showing the detected intensities in analog-to-digital units (ADU's). Despite nearly equal reported energies, the peak x-ray intensities differ by about a factor of 2.

E11803

1. The View-Angle Effect on the Observed X-Ray Intensity

The effect of view angle on observed intensity has been determined by uniformly illuminating a 1-mm-diam, Au-coated sphere (Fig. 91.21) at an intensity equal to the mean intensity on a pointing shot ($\sim 10^{14}$ W/cm²). Since all beams now overlap, the individual beam energies are ~ 6 times lower. The azimuthally averaged radial lineout of the x-ray image [Fig. 91.21(b)] is seen to closely match that expected from an optically thin plasma shell, as characterized by

$$I_x(r) = I_x(0) \times (r_0/\Delta r) \times \left[\sqrt{(1 + \Delta r/r_0)^2 - (r/r_0)^2} - \sqrt{1 - (r/r_0)^2} \right], \quad (3)$$

where $I_x(0)$ is the intensity observed at the center of the image (face-on), r is the distance in the target plane from the center of the image, r_0 is the plasma emission radius, and Δr is the plasma thickness. The profile of Fig. 91.21(b) is best fit by values of $r_0 = 500 \mu\text{m}$ and $\Delta r = 113 \mu\text{m}$.

2. Camera Cross-Calibration

Up to eight x-ray cameras are used on a pointing shot, producing different views of the beams on target. To compare beam images from two cameras, the view-angle effect must be removed, leaving only the difference in collection solid angle (pinhole area) and camera gain. Figure 91.22 shows one such comparison of beam peak intensities seen from two cameras after correcting for the view-angle effect using Eq. (3) and using the best-fit parameters as determined from the results shown in Fig. 91.21 ($\Delta r = 113 \mu\text{m}$, whereas $r_0 = 2 \text{ mm}$ for these

targets). The observed intensities follow a straight line with a zero intercept and a slope equal to the ratio of the sensitivity of the two cameras.

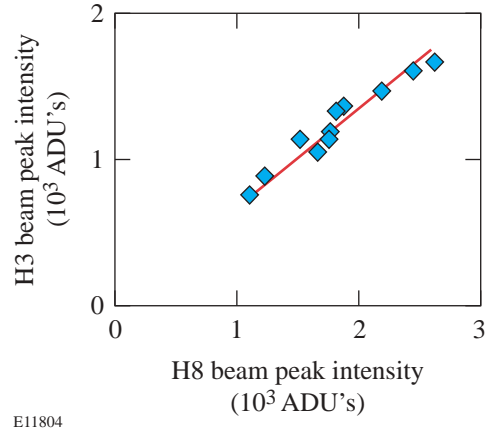


Figure 91.22

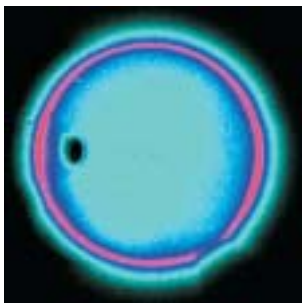
View-angle-corrected beam peak intensities as viewed by two x-ray pinhole cameras. The straight-line correlation demonstrates the validity of the view-angle correction and determines the cross-calibration factor for the two cameras.

3. Conversion-Efficiency Dependence and Determination of On-Target Beam-to-Beam Variation

An estimate of the power-law conversion of UV to x rays was determined by varying a single-beam energy, yielding a value of γ in Eq. (2) of ~ 3.7 . This preliminary value was then used when fitting values of the observed beam shapes. Combining Eqs. (1) and (2) yields

$$I_x(r) = I_x(0) \times \left[e^{-(r/\sigma_r)^\eta} \right]^\gamma, \quad (4)$$

(a) CID image (H6 view)



E11296

(b) Radial profile

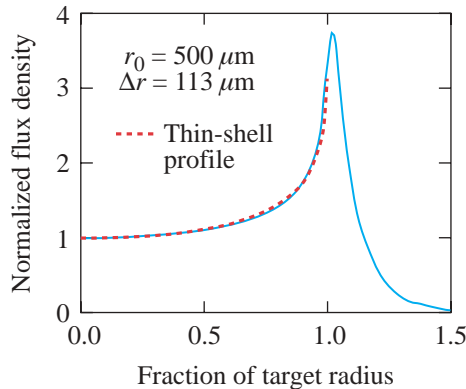


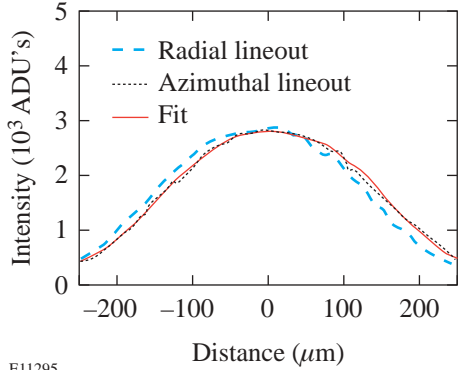
Figure 91.21

(a) An x-ray pinhole camera image of a uniformly illuminated, 1-mm-diam, Au-coated sphere used to determine the angular effect on the observed surface flux density. (b) The azimuthally averaged radial profile of the uniformity target. Regions of the target not covered by gold (at points of support during coating) were excluded from the azimuthal averaging.

where

$$I_x(0) = C_{UV-x} \times [I_{UV}(0)]^\gamma \tag{5}$$

Figure 91.23 shows a fit of a single beam (4-4) to Eq. (4). The peak values are determined in this manner for every beam by using up to eight pinhole cameras.



E11295

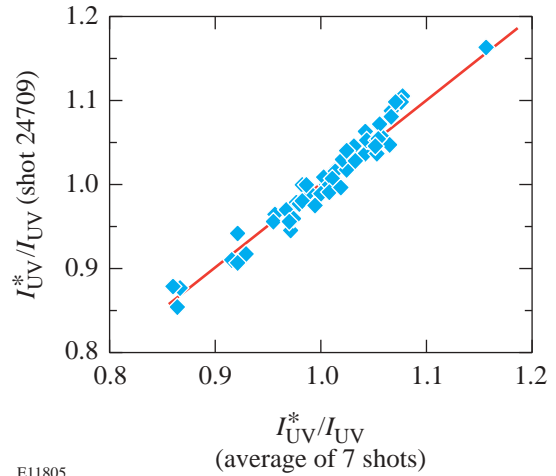
Figure 91.23
Fit to a single-beam x-ray intensity profile using a super-Gaussian with power-law x-ray conversion efficiency [Eq. (4)].

With a set of cross-calibrated cameras, variations from beam to beam can be determined for all 60 beams of OMEGA. During laser system operation, some beam-energy variation occurs due to variations in amplification and input beam (driver line) energy. System calorimeters [e.g., high-energy diodes (HED’s)] are used to account for these variations. If beam-energy variations are accounted for by variations in the HED-measured beam energies, then beam-to-beam variations not due to beam-energy variations should remain the same and show up as differences on target. This is seen in a plot of the ratio of the normalized inferred peak UV intensity I_{UV}^* derived from x-ray imaging to the normalized HED determined UV intensity I_{UV} for all 60 beams on one shot as compared with the average of the same for seven shots (Fig. 91.24). The values are seen to be stable despite large variations in beam energy. Using the average values of these ratios, R_i is given by

$$R_i = I_{UV_i}^* / E_{UV_i}^* \tag{6}$$

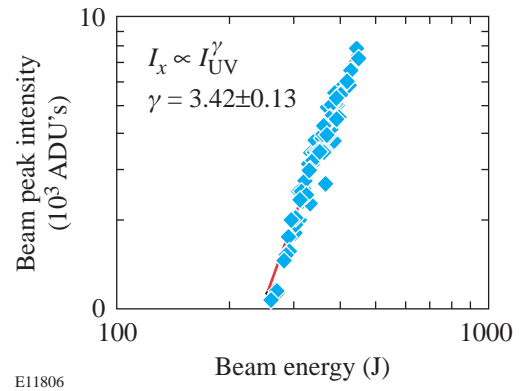
where $I_{UV_i}^*$ is the normalized x-ray-inferred UV peak intensity and $E_{UV_i}^*$ is the HED-determined normalized UV energy on

target (both for the i th beam). Applying these corrections to the HED-measured energies allows for a more accurate determination of the power-law conversion parameter γ [Eq. (4)]. A best-fit value of $\gamma = 3.42 \pm 0.13$ is seen to fit the observed x-ray to UV variation (Fig. 91.25).



E11805

Figure 91.24
Values of the ratios of the normalized x-ray-inferred beam peak intensities to the normalized HED-inferred beam energies for all 60 beams determined from one pointing shot versus the same values averaged over seven shots. Each data point represents a different beam. The beam energies were purposely varied from ~250 to 440 J, resulting in little change in these ratios despite nearly 100% changes in the peak x-ray intensity.



E11806

Figure 91.25
The observed peak x-ray intensities corrected for view-angle effect as a function of the corrected beam energies. The dependence follows a power law of $\gamma = 3.42 \pm 0.13$.

Enhanced On-Target Beam Balance

In the standard balance technique, the gains in the amplifiers by stage, and the losses by stage (primarily in the split regions), are adjusted to produce equal beam energies at the system output calorimeters. The UV energies on target are inferred from continuous-wave (cw) laser measurements of the losses incurred in each beam by the mirrors, lenses, diffracting optics, vacuum windows, and debris shields from the system output calorimeters to the target (i.e., from the transport to the target). Variations of these losses are kept to a minimum by replacement of the poorest-performing elements. In contrast, the enhanced balance technique uses the measured x-ray intensities at the target to determine the gain of the last IR amplifier required to produce equal intensities (x-ray and, hence, by inference UV also) at the target. An algorithm has been developed by which a beam's desired UV energy output can be achieved with a variation in the capacitor-bank voltage of the final disk amplifier.

Using the measured values of R_i , it is possible to further minimize on-target variations by iteration. From Eq. (6) it follows that

$$I_{UVi}^* = R_i \times E_{UVi}^* \quad (7)$$

The normalized beam energies are varied to attempt to make all values of I_{UVi}^* equal to 1. The adjustments are made by changing the capacitor bank voltage of the last amplifier and by observing the resultant change in output energy. The response follows the equation

$$E_{UV} = E_{IR} \times G_{amp}(V_{bank}) \times \epsilon_{UV}, \quad (8)$$

where E_{UV} is the inferred UV energy, E_{IR} is the input IR energy, G_{amp} is the gain of the laser amplifier for a capacitor bank voltage of V_{bank} , and ϵ_{UV} is the efficiency of the UV conversion crystals, which is also a function of G_{amp} and E_{IR} .

Figure 91.26 shows a comparison of a standard balance pointing shot (in which IR variations are minimized) to an enhanced balance pointing shot (in which peak-intensity variations are minimized). The standard balance shot [Fig. 91.26(a)] has a small variation in the HED-determined energies [$\sigma_{rms}(E_{UV}) = 2.8\%$], but a large variation in the inferred normalized UV beam peak intensities [$\sigma_{rms}(I_{UV}^*) = 6.6\%$]. Conversely, the enhanced balance shot [Fig. 91.26(b)] has a larger HED-determined variation [$\sigma_{rms}(E_{UV}) = 6.0\%$], but a

smaller variation in the inferred normalized UV beam peak intensities [$\sigma_{rms}(I_{UV}^*) = 2.2\%$]. The beam-to-beam variations have been reduced by about a factor of 3.

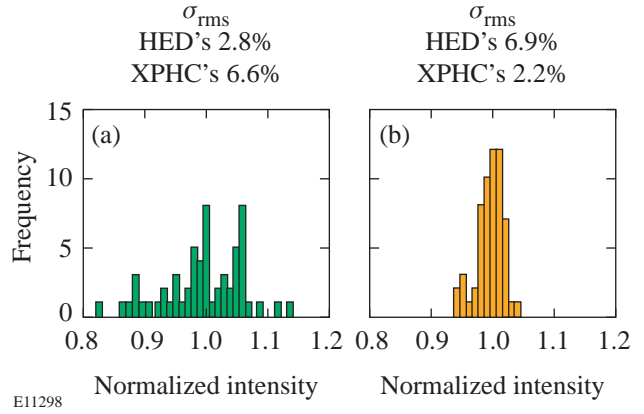


Figure 91.26

The inferred UV beam peak intensity distribution for all 60 beams of OMEGA determined on (a) a standard balance pointing shot and (b) an enhanced balance pointing shot.

Enhanced-Balance Implosion Experiments

With the enhanced-balance-correction constants R_i determined, the beam peak intensities can be inferred from the HED-determined beam energies corrected by the enhanced-correction constants R_i . Figure 91.27 shows x-ray microscope images of a set of implosions performed with standard balance and enhanced balance. Three pairs of targets were used. All were 930- μm -diam, 18.5- μm -thick CH shells filled with 15, 7, and 3 atm of D_2 gas, respectively. A clear difference is seen in the shape of the core apparently due to the change in direct-drive illumination uniformity. [The two cases had average values of $\sigma_{rms}(I_{UV}^*) = 6.0\%$ for the standard balance condition and 2.2% for the enhanced balance condition.] Figure 91.28 shows another comparison of core shape for a different shell thickness (27 μm) and fill pressure (20 atm D_2). All enhanced balance implosions show more-symmetric cores; however, small-scale structure is common to both cases.

Analysis of the angular dependence of the illumination uniformity demonstrates the effect on the implosion. The calculated overlap intensity shown in Fig. 91.29 is displayed in an Aitoff projection for the standard-balance, 15-atm-filled case (shot 24119, see Fig. 91.27). The overlap intensity calculation assumes HED-measured beam energies corrected for by

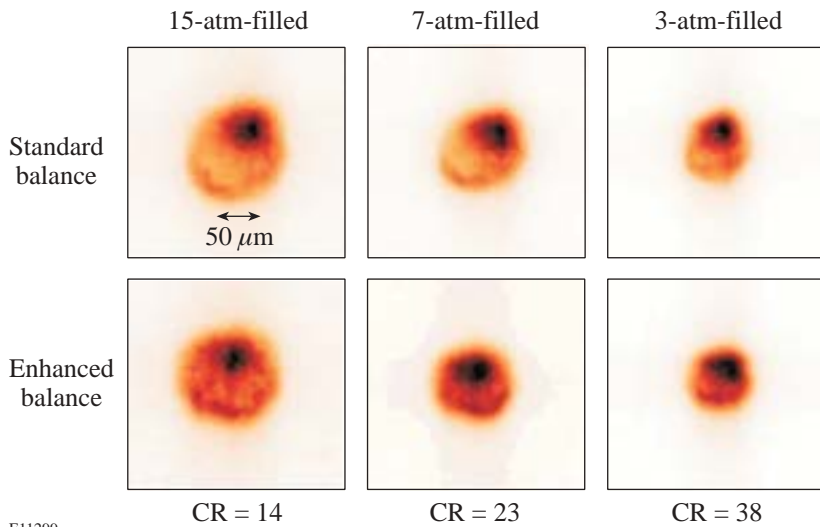
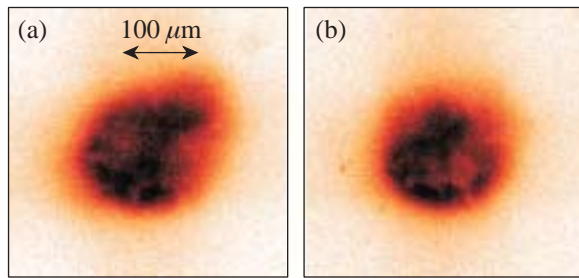


Figure 91.27 Direct-drive implosion experiments performed on OMEGA with 18.5- μm -thick CH shells filled with 15, 7, and 3 atm of D_2 gas. All shots were with ~ 23 kJ of UV on target in a 1-ns square pulse, using 1-THz SSD with PS. The enhanced balance implosions show a more-uniform spherical stagnation region. The calculated convergence ratios for these implosions (initial fuel-shell interface radius divided by final radius, CR) are indicated.

E11299

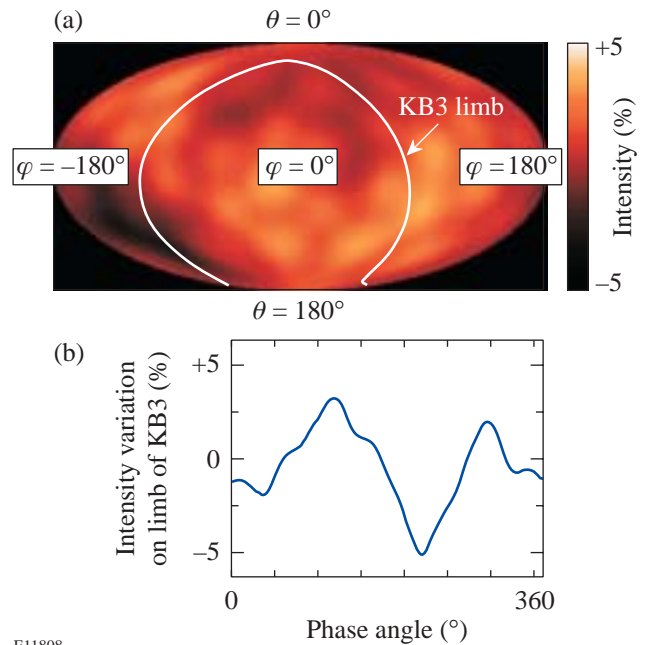
the enhanced balance analysis [Eq. (7)] with all beams having the same super-Gaussian profile ($r_0 = 300 \mu\text{m}$ and $\eta = 2.5$). Absorption is modeled by a simple cosine dependence on the angle the rays make with the target normal. The individual peaks seen are at the overlap of five or six beams and are due to the imperfect overlap of the OMEGA beams with the given target size, number of beams, and beam shape ($\sim 1.5\%$ peak to valley for perfect beam balance). Also shown is a lineout through the computed intensity pattern as would impinge on the limb of the target as seen from the x-ray microscope. The intensity pattern has an $\sim 7\%$ peak-to-valley variation with two minima at 40° and 220° and maxima at 120° and 290° , where

the angle referred to is clockwise with respect to the vertical. After applying enhanced balance, the intensity variations due to beam balance are reduced to less than 2%.



E11807

Figure 91.28 Comparison of KB (Kirkpatrick-Baez) microscope-imaged implosion cores for a pair of 27- μm -thick CH shells filled with 20 atm of D_2 , (a) with standard balance and (b) with enhanced balance. The enhanced balance implosion again shows a more spherically shaped core.



E11808

Figure 91.29 (a) The calculated overlap intensity on a standard balance implosion (OMEGA shot 24119) presented as an Aitoff projection of the entire spherical surface. The measurements from the pointing shots infer a peak to valley of 7%. (b) The lineout through the limb of the target as seen from the KB microscope used in Figs. 91.27 and 91.28.

An *ORCHID*¹⁴ 2-D hydrocode simulation was performed using the calculated intensity on the target limb from phase angle 40° to 220° for the axisymmetric laser illumination. Radiation transport is not included in this simulation. The effect of radiation losses, however, was accounted for by lowering the effective incident intensity. By its nature, a 2-D simulation can only simulate axisymmetric flow. Figure 91.30 shows the result of the simulation near the time of maximum shell compression showing a slightly distorted core with an ellipticity $e = 1.08$. Shown as an inset is the observed x-ray image with the axis of the minima in the calculated intensity indicated. The ellipticity of the core image and the simulation are in good agreement, confirming that the main effect is explained by a measurable beam imbalance. Correcting the beam imbalance nearly removes the residual ellipticity as a result of the more-uniform illumination by the 60 beams of OMEGA.

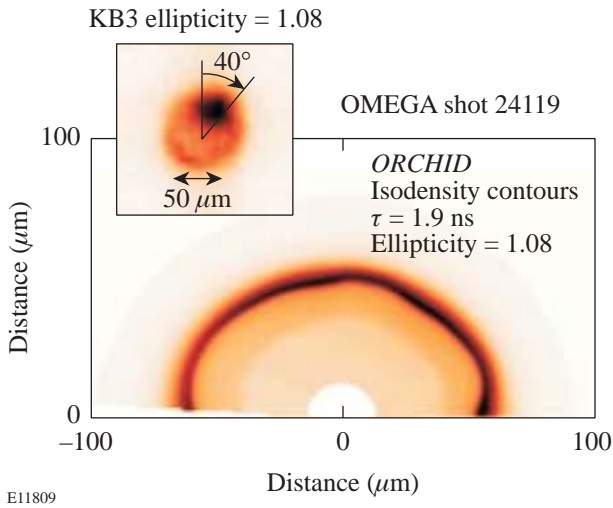


Figure 91.30
Isodensity contours from an *ORCHID* 2-D hydrocode simulation of the implosion of an 18.5- μm -thick, 15-atm-filled CH shell (OMEGA shot 24119). The time of this snapshot is 1.9 ns from the start of the laser pulse (near the time of maximum shell compression). The input intensities used were those calculated for this experiment and occurring on the limb of the target as observed from the KB microscope. The corresponding image is shown as an inset with the symmetry axis of the 2-D simulation indicated.

The symmetry of the implosions appears to correlate with the beam balance. To determine the effects on other measures of target performance, a series of implosion experiments were performed with 1-THz SSD smoothing with PS and 1-ns square pulses. The targets ranged from 18 to 25 μm in thickness

and were filled with 3 or 15 atm of D_2 gas. Figure 91.31(a) shows the ratio of the measured D-D neutron yield to the *LILAC* hydrocode¹⁵-predicted yield [yield over calculated (YOC)] for these experiments. This measure of target performance is used as a means of comparison to account for differences in energy on target and shell-thickness differences from shot to shot. The enhanced balance target implosions were performed with slightly less energy (typically 21 kJ on enhanced balance shots and 23 kJ on standard balance shots) since after correction for imbalance, some beams could not be raised to sufficiently high levels, necessitating all others to be lowered. The results are seen to follow the included trend lines (dashed) with little obvious difference due to balance condition. Figure 91.31(b) shows the measured ratio of D-T neutron secondary yield to D-D neutron primary yield in these same experiments. [The only difference between the two balance conditions is the apparent larger variation in the standard balance values of the 15-atm-filled target implosions. Despite a definite change to more-symmetric shell stagnations, the primary and secondary neutron yield measurements indicate little dependence of target performance on balance condition (at least

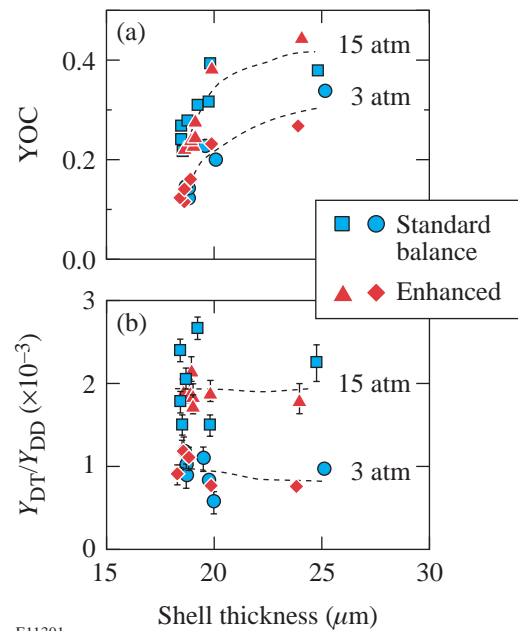


Figure 91.31
Measurements of the fusion yield's dependence on balance condition from a set of 3- and 15-atm- D_2 -filled CH shell implosions: (a) the ratio of the measured to the simulated primary D-D neutron yield; (b) the ratio of the measured secondary DT neutron yield to the measured primary D-D neutron yield.

with these measurements).] Whereas, it has been shown in past experiments that these measurements show a dependence on single-beam smoothing.^{5,6,10}

Additional measurements of the directional dependence of the total ρR at the time of peak fusion production have recently been reported by Séguin *et al.*¹⁶ Their measurements are derived from the slowing down of 14.7-MeV D-He³ fusion reaction-generated protons observed from different directions around the target. They find that the observed ρR asymmetries are significantly different for the two balance conditions reported in this work (standard and enhanced). Although asymmetries still exist, they appear to be lower when the optimum x-ray-inferred enhanced balance condition is imposed.

Conclusions

A method for determining and optimizing the beam-to-beam intensity variation of the 60 beams of the OMEGA laser system, as configured for direct-drive illumination (with 1-THz SSD and polarization smoothing), has been developed. This method infers the beam-to-beam energy balance by direct observation of x rays emitted by Au plasmas produced by OMEGA's focused high-power laser beams. The UV energy balance is determined from the observed x-ray balance by taking into account x-ray conversion efficiency and view-angle effects in a semi-empirical manner. Optimized or enhanced balance is achieved by removing the precisely determined beam-to-beam energy variation by adjusting the gain of the last amplifier. The method has achieved a three-fold reduction in the beam imbalance, from an inferred level of ~6% (rms) to ~2% (rms).

Direct-drive implosions with enhanced beam balance consistently show more spherically shaped stagnation cores. A 2-D hydrocode simulation of an uncorrected (standard balance) implosion shows that the magnitude and direction of the resulting core distortion are consistent with arising from beam imbalance. In contrast there is little effect on the YOC ratio or fuel areal density.

The small differences in beam-to-beam energy (<10%) have not been explained by repeated measurements of transport losses in the mirrors, lenses, diffracting optics, and windows. It is likely that the differences are due to scattering losses not accounted for by the spatially integrating techniques employed to measure transport and can be determined only by a technique, such as described in this work, that measures the intensity at the target with calibrated imaging diagnostics.

ACKNOWLEDGMENT

This work was supported by the U.S. Department of Energy Office of Inertial Confinement Fusion under Cooperative Agreement No. DE-FC03-92SF19460 and the University of Rochester. The support of DOE does not constitute an endorsement by DOE of the views expressed in this article.

REFERENCES

1. J. Nuckolls *et al.*, *Nature* **239**, 139 (1972).
2. J. D. Lindl, *Inertial Confinement Fusion: The Quest for Ignition and Energy Gain Using Indirect Drive* (Springer-Verlag, New York, 1998), Chap. 6, pp. 61–82.
3. S. E. Bodner, D. G. Colombant, J. H. Gardner, R. H. Lehmberg, S. P. Obenschain, L. Phillips, A. J. Schmitt, J. D. Sethian, R. L. McCrory, W. Seka, C. P. Verdon, J. P. Knauer, B. B. Afeyan, and H. T. Powell, *Phys. Plasmas* **5**, 1901 (1998).
4. T. R. Boehly, D. L. Brown, R. S. Craxton, R. L. Keck, J. P. Knauer, J. H. Kelly, T. J. Kessler, S. A. Kumpan, S. J. Loucks, S. A. Letzring, F. J. Marshall, R. L. McCrory, S. F. B. Morse, W. Seka, J. M. Soures, and C. P. Verdon, *Opt. Commun.* **133**, 495 (1997).
5. F. J. Marshall, J. A. Delettrez, V. Yu. Glebov, R. P. J. Town, B. Yaakobi, R. L. Kremens, and M. Cable, *Phys. Plasmas* **7**, 1006 (2000).
6. F. J. Marshall, J. A. Delettrez, R. Epstein, V. Yu. Glebov, D. R. Harding, P. W. McKenty, D. D. Meyerhofer, P. B. Radha, W. Seka, S. Skupsky, V. A. Smalyuk, J. M. Soures, C. Stoeckl, R. P. Town, B. Yaakobi, C. K. Li, F. H. Séguin, D. G. Hicks, and R. D. Petrasso, *Phys. Plasmas* **7**, 2108 (2000).
7. C. Stoeckl, C. Chiritescu, J. A. Delettrez, R. Epstein, V. Yu. Glebov, D. R. Harding, R. L. Keck, S. J. Loucks, L. D. Lund, R. L. McCrory, P. W. McKenty, F. J. Marshall, D. D. Meyerhofer, S. F. B. Morse, S. P. Regan, P. B. Radha, S. Roberts, T. C. Sangster, W. Seka, S. Skupsky, V. A. Smalyuk, C. Sorce, J. M. Soures, R. P. J. Town, J. A. Frenje, C. K. Li, R. D. Petrasso, F. H. Séguin, K. Fletcher, S. Padalino, C. Freeman, N. Izumi, R. Lerche, and T. W. Phillips, *Phys. Plasmas* **9**, 2195 (2002).
8. Laboratory for Laser Energetics LLE Review **81**, 6, NTIS document No. DOE/SF/19460-335 (1999). Copies may be obtained from the National Technical Information Service, Springfield, VA 22161.
9. S. Skupsky, R. W. Short, T. Kessler, R. S. Craxton, S. Letzring, and J. M. Soures, *J. Appl. Phys.* **66**, 3456 (1989).
10. D. D. Meyerhofer, J. A. Delettrez, R. Epstein, V. Yu. Glebov, V. N. Goncharov, R. L. Keck, R. L. McCrory, P. W. McKenty, F. J. Marshall, P. B. Radha, S. P. Regan, S. Roberts, W. Seka, S. Skupsky, V. A. Smalyuk, C. Sorce, C. Stoeckl, J. M. Soures, R. P. J. Town, B. Yaakobi, J. D. Zuegel, J. Frenje, C. K. Li, R. D. Petrasso, D. G. Hicks, F. H. Séguin, K. Fletcher, S. Padalino, M. R. Freeman, N. Izumi, R. Lerche, T. W. Phillips, and T. C. Sangster, *Phys. Plasmas* **8**, 2251 (2001).
11. P. D. Goldstone, J. A. Cobble, A. Hauer, G. Stradling, W. C. Mead, S. R. Goldman, S. Coggeshall, M. C. Richardson, P. A. Jaanimagi, O. Barnouin, R. Marjoribanks, B. Yaakobi, F. J. Marshall, P. Audebert, and J. Knauer, in *X Rays from Laser Plasmas*, edited by M. C. Richardson (SPIE, Bellingham, WA, 1987), Vol. 831, pp. 54–61.

12. J. M. Soures, R. L. McCrory, C. P. Verdon, A. Babushkin, R. E. Bahr, T. R. Boehly, R. Boni, D. K. Bradley, D. L. Brown, R. S. Craxton, J. A. Delettrez, W. R. Donaldson, R. Epstein, P. A. Jaanimagi, S. D. Jacobs, K. Kearney, R. L. Keck, J. H. Kelly, T. J. Kessler, R. L. Kremens, J. P. Knauer, S. A. Kumpan, S. A. Letzring, D. J. Lonobile, S. J. Loucks, L. D. Lund, F. J. Marshall, P. W. McKenty, D. D. Meyerhofer, S. F. B. Morse, A. Okishev, S. Papernov, G. Pien, W. Seka, R. Short, M. J. Shoup III, M. Skeldon, S. Skupsky, A. W. Schmid, D. J. Smith, S. Swales, M. Wittman, and B. Yaakobi, *Phys. Plasmas* **3**, 2108 (1996).
13. F. J. Marshall, T. Ohki, D. McInnis, Z. Ninkov, and J. Carbone, *Rev. Sci. Instrum.* **72**, 713 (2001).
14. R. L. McCrory and C. P. Verdon, in *Inertial Confinement Fusion*, edited by A. Caruso and E. Sindoni (Editrice Compositori, Bologna, Italy, 1989), pp. 83–124.
15. M. C. Richardson, P. W. McKenty, F. J. Marshall, C. P. Verdon, J. M. Soures, R. L. McCrory, O. Barnouin, R. S. Craxton, J. Delettrez, R. L. Hutchison, P. A. Jaanimagi, R. Keck, T. Kessler, H. Kim, S. A. Letzring, D. M. Roback, W. Seka, S. Skupsky, B. Yaakobi, S. M. Lane, and S. Prussin, in *Laser Interaction and Related Plasma Phenomena*, edited by H. Hora and G. H. Miley (Plenum Publishing, New York, 1986), Vol. 7, pp. 421–448.
16. F. H. Séguin, C. K. Li, J. A. Frenje, S. Kurebayashi, R. D. Petrasso, F. J. Marshall, D. D. Meyerhofer, J. M. Soures, T. C. Sangster, C. Stoeckl, J. A. Delettrez, P. B. Radha, V. A. Smalyuk, and S. Roberts, *Phys. Plasmas* **9**, 3558 (2002).

Effects of Textures on Hydrogen Diffusion in Nickel

Introduction

The transition metal–hydrogen systems have been intensively researched for many years because of the various applications of these systems. A large hydrogen solubility in some transition metals allows their use for safe and high-capacity hydrogen storage.^{1,2} At the other end of the spectrum, hydrogen ingress at low concentrations can induce mechanical degradation of nickel and nickel alloys and compromise the intended application of the metal.^{1,3} An understanding of hydrogen adsorption/desorption characteristics on, and hydrogen mobility in, the metals is needed to predict the hydrogen impact on the metal systems.

Both deuterium and tritium are used as fuel for inertial confinement fusion (ICF) energy. In ICF applications, both adsorption on surfaces and permeation through metals are of importance. Hydrogen adsorption and desorption processes intimately control the degree to which surfaces become contaminated and subsequently the extent to which these surfaces can be decontaminated. In general, the smaller the adsorption rate, the shorter the residence time on a surface, and the simpler the structure of the oxide on a surface, the less susceptible that surface is to tritium contamination for a given set of exposure conditions. Contamination can proceed by simple condensation on a surface followed by absorption into the subsurface structure and by beta-activated radical surface reactions that capture mobile tritium atoms on surfaces into more tightly bound tritium-bearing complexes that are difficult to remove.

Surface tritium can also be absorbed into the metal and permeate to the opposite side, from where it can escape the process loop or contaminate a coolant circuit. For example, a nickel-alloy vessel with 1/32-in.-thick walls filled with tritium gas at 1 atm and room temperature will permeate 0.3 pCi/s/cm² in steady state, a tolerable release rate in part because the time to attain steady state is 6.3 years. At 300°C, however, this container will reach steady-state permeation within 1.6 h and release tritium at 0.8 μCi/s/cm². Such releases are unacceptably high and require intervention to preclude unacceptable releases to the environment or accumulation in cooling cir-

cuits. Permeation-resistant barriers, engineered composites, and low-absorption-coated, textured surfaces can offer relief from these emissions.

Hydrogen molecules dissociate on metal surfaces, dissolve atomically into the substructure, and interact with the microstructure of the metals. The interaction depends not only on the hydrogen concentration in the bulk but also on the prevalent microstructure; i.e., the mixture of crystal defects, grain boundaries, grain size, grain orientation, and phase composition present within the metal matrix. The density and blend of these features depends on the manufacturing and operating history of the metal.

For example, electrodeposition is the preferred approach to fabricate nickel membranes in industry. The texture of the nickel membranes can be controlled by the deposition parameters. Since hydrogen permeation in single-crystal metals is anisotropic, textured polycrystalline metals may exhibit different permeation properties for different textures. While an earlier study⁴ has shown that texture can influence hydrogen adsorption and diffusion in metals, to date there has been no systematic investigation of the effect of textures on hydrogen permeation through nickel. In this article, the relationship between hydrogen permeation and grain orientation in nickel membranes is studied. To this end, the following section outlines the experimental procedures used to prepare and characterize the nickel membranes and to measure the permeability of the membrane. Subsequent sections describe the details of the microstructure and its influence on permeation.

Experimental Procedure

Nickel membranes were electroplated in a Watt's bath at 50°C. The electrolyte comprised 300 g/l of NiSO₄ • 6H₂O, 35 g/l of NiCl₂ • 6H₂O, and 35 g/l of H₃CO₃ to make a pH-3 liquid. The electroplating current density was controlled galvanostatically between 0.1 to 0.8 A/cm². The anode was pure nickel. A titanium cathode substrate was chosen to support the nickel film during deposition because the nickel membranes could be easily peeled off. The substrate surface

was mechanically polished to minimize imprinting the substrate grain structure on the growing nickel film. Additionally, film thickness usually exceeded $50\ \mu\text{m}$ to further minimize imprinting the substrate orientation on the film's texture in preference for that favored by the electrodeposition parameters. The nickel deposits were then removed from the substrates to measure their grain orientation without any interference from the substrate. The permeability of these membranes were subsequently studied in an electrochemical cell.

The membrane surface texture was measured with a Siemens x-ray diffractometer outfitted with a molybdenum target. Maps of the orientation of the (100), (110), and (111) directions were measured in 5° polar and radial steps up to a maximum tilt of 80° . Orientation distribution functions (ODF) were calculated from these maps, also known as pole figures, according to the procedure described by Bunge⁵ with the aid of the software TexTool 3.0.

Hydrogen permeation was measured electrochemically with the aid of two cells separated by the nickel membrane of interest using the configuration shown in the Fig. 91.32. Hydrogen was injected into the membrane on the upstream side at a fixed rate, and the extraction rate was measured on the downstream side.

The electrolyte in both cells was 0.1 N NaOH to yield a pH 13 solution. On the exit (anode) side, a separate Ni/NiO electrode served as a saturated calomel electrode to maintain the membrane at a constant potential of 0.3 V relative to the anode. Prior to any measurements, both compartments were deoxygenated by bubbling nitrogen gas through the solutions. The measurements were carried out at 22°C . Before charging the membrane, an anodic potential 0.3 V was applied for 24 h to extract any residual hydrogen from the membrane and to reduce the background permeation current density. A graphite

cathode on the entry side was polarized galvanostatically to ensure that the singly charged ionic hydrogen flux impinging on the upstream surface was constant and fixed at a current density of $0.1\ \text{mA}/\text{cm}^2$. At this current density, the hydrogen flux reaching the membrane is 6×10^{14} particles/ $\text{s}\cdot\text{cm}^2$. Permeant hydrogen is collected downstream of the membrane as the anodic current flows between the membrane and the anode. Sometime after the initiation of a cathodic current, an anodic current appears downstream and grows in strength to a maximum value. At this time, the hydrogen concentration gradient across the membrane thickness is linear, being highest at the entry side and nearly zero at the exit side. The time integral of the permeation current becomes constant once the linear concentration gradient is established within the membrane. Extrapolating the straight portion of the time-integrated curve back to the time axis yields a unique value known as the lag time (t_L). This time is related to the hydrogen diffusion coefficient (D) for the material⁶ by the relation

$$t_L = \frac{x^2}{2D}, \quad (1)$$

where x is the membrane thickness.

The concentration of adsorbed hydrogen on the upstream surface reflects the dynamic equilibrium between particles arriving from the electrolyte and particles disappearing into the metal. If the arrival flux rate far exceeds the absorption flux rate, hydrogen bubbles form on the upstream surface. Hydrogen transport through the metal is the rate-limiting step. If the absorption rate exceeds the arrival rate, the permeant flux is limited by the hydrogen arrival rate at the surface rather than by the adsorption rate into the metal. In this work, hydrogen transport through the metal is the rate-limiting step. In this case, steady-state permeation is described by Fick's First Law, and the concentration of absorbed hydrogen on the input

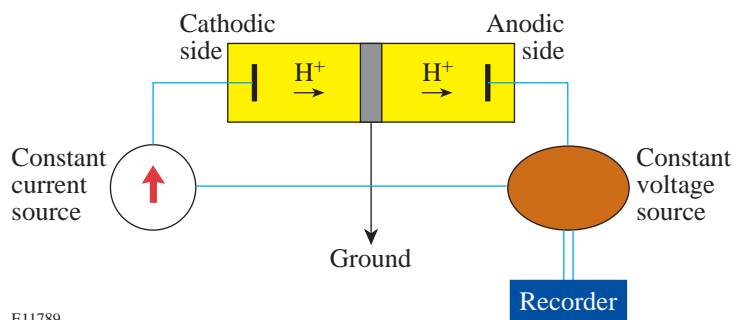


Figure 91.32
Schematic layout of the electrolytic permeation facility.

surface, C_0 , is uniquely related to the steady-state anodic current density I_{ss} by the relation

$$C_0 = \frac{I_{ss}x}{FD}, \quad (2)$$

where F is the Faraday constant (= 96,485 Coul/g-atm).

Results and Discussion

1. Microstructure and Texture

The microstructure across the cross section of each nickel deposit comprised three distinct zones. Grains in the vicinity of the film–substrate interface were equiaxed and fine. Immediately above this layer, the structure began to change from equiaxed grains to columnar grains. Beyond that and for the remainder of the film up to the nickel–air interface, the grains were columnar and orientated perpendicular to the substrate for most electroplating conditions.

The orientation of grains, i.e., the texture of the surface, was measured by Bragg diffraction to generate the ODF's. Figure 91.33 illustrates the ODF of the titanium substrate used in this work. This ODF is typical of a cold-rolled titanium plate.⁷ A typical ODF for a nickel membrane electrodeposited for the present work is presented in Fig. 91.34. Inspection of these two distribution functions indicates that there has been no textural imprinting by the substrate on the nickel deposit. The nickel texture has been determined solely by the deposition parameters.

Either (100) or (110) fiber textures can be obtained by changing the deposition conditions. At low current density, the (100) fiber texture is preferred. At high current density, the (110) fiber texture dominates. The (111) texture can be derived by annealing deposits with strong $\langle 100 \rangle$ texture at 800°C for 1 h.⁸

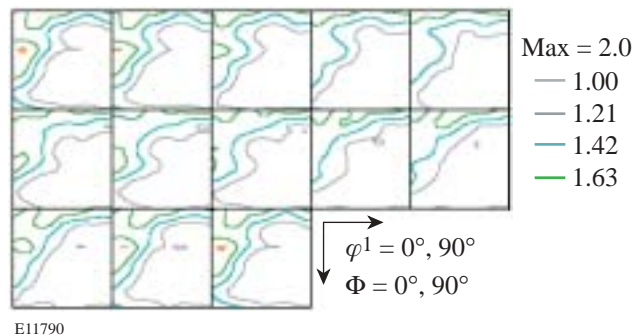


Figure 91.33
Orientation distribution function of the titanium substrate.

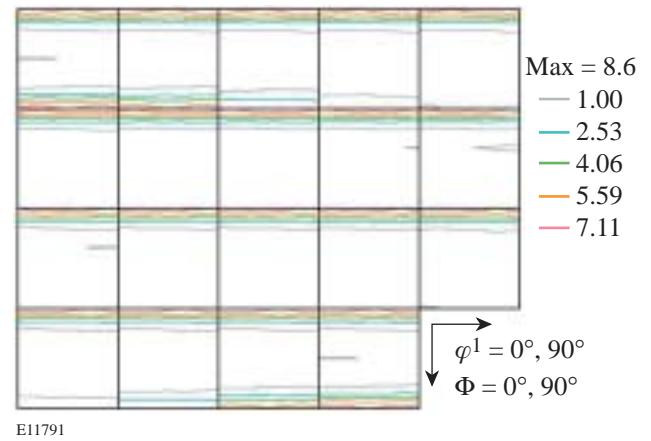


Figure 91.34
Orientation distribution function of nickel deposit.

2. Hydrogen Permeation and Analysis

The temporal behavior of hydrogen permeation through nickel with different textures is shown in Fig. 91.35. The permeation behavior for a nickel sample without any dominant texture has been included for reference. In all cases, the permeation current increases smoothly with increasing charging time to a maximum constant value. There are significant differences, however, among the textured and nontextured membranes. Hydrogen transport through (111) texture is faster than for any of the other textures. The time to attain steady-state permeation is longest in (110) texture nickel. Compared to the sample without any dominant texture, the response time for surfaces with a dominant texture is rapid.

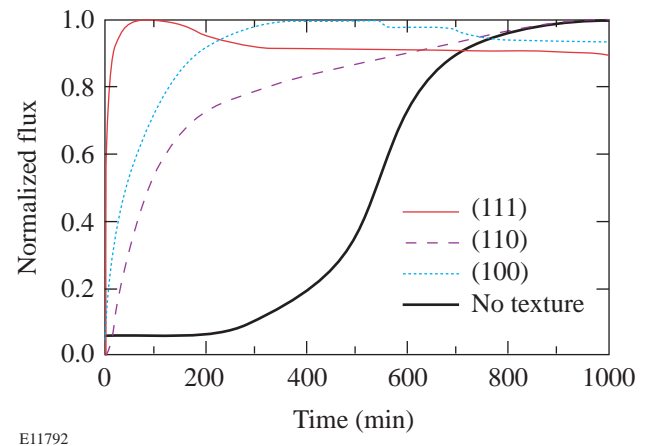


Figure 91.35
Temporal evolution of hydrogen permeation through nickel membrane with differing textures and for a sample without any dominant texture.

Hydrogen diffusivity and near-surface hydrogen concentration have been calculated using Eqs. (1) and (2) for the various nickel membranes and are listed in Table 91.III. Diffusion coefficients for (100) and (110) single-crystal samples have been provided for comparison. The coefficients are seen to increase as one moves toward more-open crystal structures, i.e., from (100) to (110) and then to (111) textured samples. The sample without any dominant texture exhibits the lowest diffusion coefficient of all the samples investigated. Diffusion coefficients for polycrystalline nickel membranes with dominant (100) and (110) textures are respectively higher than for (100) and (110) single-crystal membranes, but both exhibit the same trend when moving toward more-open structures, i.e., from (100) to (110) textures.

The near-surface concentration (C_0) of hydrogen in the sample without any dominant texture is the highest. The concentrations in (111) and (110) textured cases are the lowest of the samples studied and lie within experimental error of each other. This table suggests that the near-surface hydrogen concentration on the upstream side of the membrane is depleted by rapid transport through the membrane. The higher the diffusivity, the lower the subsurface hydrogen concentration.

Hydrogen permeation through a metal membrane in an electrochemical environment involves three steps: hydrogen atom absorption, diffusion across the membrane, and desorption. The molecular dissociation and the atomic association steps on the upstream and downstream sides of the membrane respectively that are normally associated with gas-phase hy-

drogen permeation are not present in this case because the hydrogen arrives and leaves the membrane as ions in the electrolyte. Hydrogen transport is characterized by three interaction energies: absorption, diffusion, and desorption. Typically adsorption and desorption energies are the same for polycrystalline metals without any dominant texture. The diffusion energy tends to be governed by bulk microstructural features, such as grain orientation, grain boundary density, and trap density. Both activation energies can influence the total hydrogen permeation flux and the temporal evolution of that flux.

Hydrogen adsorption energies differ for various crystal planes.¹²⁻¹⁴ These have been measured for the three low-index planes: (100), (110), and (111) of nickel.¹² The net adsorption energy of a surface can be estimated from weight-averaged linear combinations of adsorption energies on low-index planes and the preponderance of those planes on a specific surface. Typically, the results are displayed on an inverse pole figure to account for the distribution of the low-index planes in a selected direction in the specimen relative to the crystal axes. Crystals in face-centered cubic metals such as nickel possess higher degrees of symmetry, and the three low-index planes, (100), (110), and (111), are adequate to uniquely specify a surface orientation. Consequently only the unit stereographic triangle needs to be shown. Figure 91.36 displays the net surface adsorption energy dependence of hydrogen on nickel. This figure shows that the adsorption energy is highest for (100) and lowest for (111). Hydrogen is expected to adsorb more easily through (111) planes than either (100) or

Table 91.III: Hydrogen permeation data for nickel with different textural surfaces.

Membrane Surface Structure		D (10^{-9} cm ² /s) ±5%	C_0 (mmol/cm ³) ±10%
Polycrystalline Ni	No texture	2.6	0.38
	(100)	3.4	0.18
	(110)	6.5	0.12
	(111)	8.5	0.13
Single-Crystal Ni	(100)	0.56 (Ref. 9)	
		0.51 (Ref. 10)	
	(110)	0.62 (Ref. 11)	

(110) planes. As a consequence, hydrogen ingress and transport through nickel can be tailored by altering the surface orientation of crystals to favor or suppress the (111) plane.

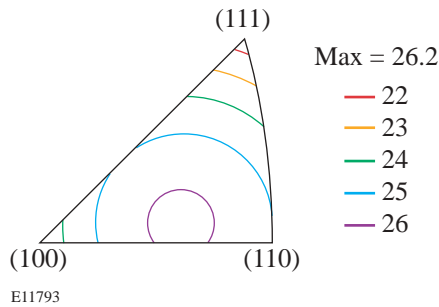


Figure 91.36
Hydrogen absorption energies for the three low-index planes in nickel.

Diffusivity can also be modulated by orientation.^{9–11} Table 91.III indicates that hydrogen transport is more rapid in single crystals via (110) than (100) orientations. Polycrystalline membranes are combinations of many single crystals with different orientations. Texturing a polycrystalline membrane provides a method for selecting a dominant orientation with the intent of enhancing or suppressing hydrogen adsorptions and subsequent transport. Hydrogen transport can be modulated by textural control in addition to the bulk microstructural features discussed earlier.

Conclusions

Nickel membranes with differing textures have been grown and analyzed. Deposition parameters that influence the texture during the growing process have been identified. These protocols were implemented to construct membranes for permeation experiments. Electrolytic permeation has been used to study the impact of texture on hydrogen permeation through nickel.

Four conclusions can be derived from this work: First, textured nickel films can be grown on titanium without textural imprinting from the substrate. Plating current density has a strong influence on texture forms of nickel deposits. At low current density, the (100) fiber texture is the dominant component; at high current density, the (110) fiber texture dominates. Annealing at 800°C for 1 h, (100) texture converts to (111) texture. Second, hydrogen permeation through nickel membranes depends on texture. Diffusion coefficients increase as one moves from (100) to (110) to (111) textured samples. The diffusion coefficient of a sample without a

dominant texture is smaller than for textured samples. Diffusion coefficients of polycrystalline textured membranes are higher than similar single-crystal membranes, but both sets of membranes exhibit similar trends in behavior. Third, adsorption energies for different orientations have been calculated by using the weight-averaged combinations of the absorption energies for the three basic planes in nickel: (100), (110), and (111). Absorption energies for different orientations are presented. Finally, hydrogen transport in the bulk is expected to depend on texture in addition to the microstructural features such as grain size, traps, and grain boundary density typically discussed in the literature.

ACKNOWLEDGMENT

This research was supported by the Natural Sciences and Engineering Research Council of Canada (NSERC) under CRD Grant # CRDPJ 207805-97 and Ontario Power Technologies.

REFERENCES

1. H. Wipf and R. G. Barnes, *Hydrogen in Metals III: Properties and Applications*, Topics in Applied Physics, Vol. 73 (Springer, Berlin, 1997).
2. K. Hong, *J. Alloys Compd.* **321**, 307 (2001).
3. R. M. Latanision and M. Kurkela, *Corrosion* **39**, 174 (1983).
4. Y. Cao, J. A. Spunar, and W. T. Shmayda, "Microstructure Control Factors of Hydrogen Diffusion Through Palladium and Pd-Ag Membranes," to be published in *Defect and Diffusion Forum*.
5. H.-J. Bunge, *Texture Analysis in Materials Science: Mathematical Methods* (Butterworths, London, 1982).
6. M. A. V. Devanathan and Z. Stachurski, *Proc. R. Soc. Lond. A, Math. Phys. Sci.* **270**, 90 (1962).
7. H. Inoue and N. Inakazu, in *Eighth International Conference on Textures of Materials (ICOTOM 8)*, edited by J. S. Kallend and G. Gottstein (The Metallurgical Society, Warrendale, PA, 1988), pp. 997–1004.
8. F. Czerwinski and J. A. Szpunar, *Corros. Sci.* **41**, 729 (1999).
9. A. M. Brass and A. Chanfreau, *Acta Mater.* **44**, 3823 (1996).
10. Y. Ebisuzaki, W. J. Kass, and M. O'Keefe, *J. Chem. Phys.* **46**, 1378 (1967).
11. A. M. Brass, A. Chanfreau, and J. Chene, in *Hydrogen Effects on Materials Behavior*, edited by N. R. Moody and A. W. Thompson (Minerals, Metals, and Materials Society, Warrendale, PA, 1990), pp. 19–31.
12. G. Kresse and J. Hafner, *Surf. Sci.* **459**, 287 (2000).
13. K. Christmann *et al.*, *J. Chem. Phys.* **70**, 4168 (1979).
14. G. Kresse, *Phys. Rev. B, Condens. Matter* **62**, 8295 (2000).

Superconducting Properties of MgB₂ Thin Films Prepared on Flexible Plastic Substrates

The recent discovery of superconductivity at 39 K in hexagonal magnesium diborides¹ has stimulated very intensive investigations of the fundamental mechanism of superconductivity in MgB₂ as well as the possible practical applications of this new superconductor. In comparison with high-temperature cuprates, MgB₂ superconductors have more than two-times-lower anisotropy, significantly larger coherence length, and higher transparency of grain boundaries to the current flow. At the same time, when compared to conventional metallic superconductors (including Nb₃Sn or NbN), they have at least two-times-higher critical temperature T_c and energy gap, as well as higher critical current density J_c . As a result, MgB₂ superconductors are expected to play an important role for high-current, high-field applications, as well as in cryoelectronics, where they might be the material-of-choice for above-300-GHz clock-rate digital electronics. In addition, MgB₂ devices could operate in simple cryocoolers.

The availability of high-quality superconducting thin films with single-crystal-like transport properties² is the key to realization of practical MgB₂ cryoelectronic devices. Films with high values of T_c and J_c have been prepared on SrTiO₃, Al₂O₃, Si, SiC, and other substrates by various deposition techniques.^{3–8} All of the above procedures required post-annealing at temperatures higher than 600°C, and the superconducting properties of the resulting films depended very strongly on the conditions of their annealing. The best reported MgB₂ thin films are characterized by $T_c \approx 39$ K and $J_c > 10^7$ A/cm² at 4.2 K and 5×10^5 A/cm² at 30 K, both at zero external magnetic field.⁹ Preparation of MgB₂ thin films on unconventional substrates, such as stainless steel¹⁰ or plastic foils, is also desirable. MgB₂-on-steel films are interesting for the preparation of low-magnetic shielding and antennas, while plastic foils are very attractive for their bending and shaping abilities.

In this article, we present the preparation and superconducting properties of MgB₂ thin films fabricated on flexible substrates (Kapton-E polyamide foil), using three specially designed, rapid annealing processes. Flexible plastic substrates introduce a number of novel aspects to superconducting

technology, such as the ability to cut the final structures into desired shapes for, as an example, magnetic shielding. They are also unbreakable and can be rolled into small superconducting coils or form flexible microwave or high-speed digital microstrips and coplanar transmission lines.

Kapton-E foils up to 20×20 cm² (limited in size by our deposition apparatus) were cleaned in acetone, ultrasonically washed in ethanol, and air-dried before being placed in our vacuum chamber. Mg-B precursor films 100 nm to 200 nm thick with a nominal composition of 1:2 were prepared on the unheated foil by simultaneous evaporation of Mg (purity 99.8%) and B (purity 99.9%) from separate W and Ta resistive heaters at a vacuum of 8×10^{-4} Pa. After deposition, the Mg-B films were *ex-situ* annealed in a special low-temperature process to avoid overheating the Kapton foil, which had to be kept below its 300°C deformation temperature.

Several rapid annealing procedures have been implemented. Initially, the Mg-B films were placed inside a quartz tube on a thick sapphire plate and introduced for 10 to 300 s into a preheated furnace. The furnace temperature varied from 350°C to 500°C, and the Ar atmosphere could be changed from 3 kPa to 100 kPa in a flow regime. In another approach, the Mg-B films were placed “face down” on a resistive heater and annealed at 500°C to 600°C in pure Ar for 60 to 180 s. For overheating protection, the foil was covered with a sapphire plate and a large Cu block on top. After annealing, the samples were cooled down in approximately 30 s to room temperature. Both of the above annealing methods resulted in superconducting MgB₂ with $T_{c,on}$ up to 33 K and a transition temperature $\Delta T_c \approx 10$ K. The highest $T_{c,on}$ was obtained after annealing for 180 s at 500°C on a resistive heater. Unfortunately, under such conditions, the color of the Kapton foil changed from yellow to black and it partially lost its flexibility. The maximal J_c was only about 500 A/cm² at 4.2 K, suggesting that the damaged foil stressed the MgB₂ film.

Much better results were obtained using the third annealing method; thus, the remainder of this work will be devoted to

those films. The Mg-B thin films were radiatively heated with halogen lamps in vacuum; simultaneously, the substrate side of our samples was placed on an external water-cooled radiator to protect the plastic foil. The distance between the samples and the halogen source was 7 cm, and the vacuum chamber was pumped down to a base pressure of 1×10^{-2} Pa to minimize the oxygen content and other gas impurities during annealing. The foil temperature was controlled by a thermocouple located very close to its surface. The duration of the annealing process was 60 to 180 s, and the temperature at the film surface varied from 300°C to 650°C. After annealing, the vacuum chamber was filled with Ar and the films were cooled to room temperature in 20 to 30 s. Even for the highest Mg-B annealing temperature, the Kapton was always kept below 300°C, no deformation or change of color was observed, and the resulting MgB_2 samples were fully flexible.

Figure 91.37 shows the surfaces and the critical temperature parameters of three films annealed under different condi-

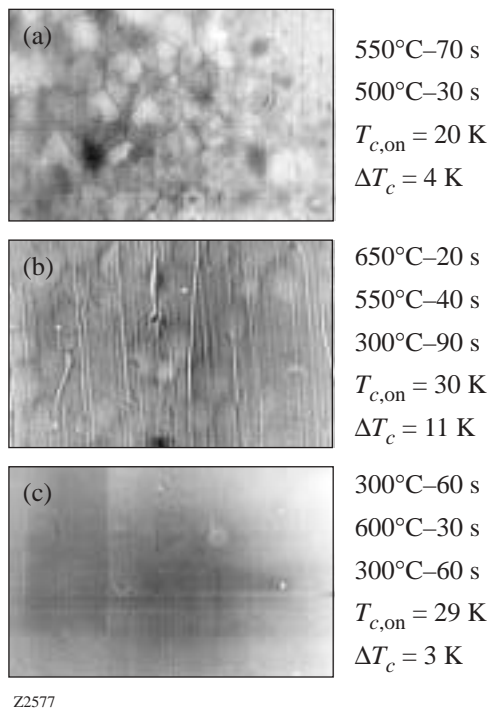


Figure 91.37 Scanning-electron-microscope pictures of three MgB_2 thin films annealed under different conditions in the halogen lamp process. Each picture is identified by the film-annealing temperatures and times, and the resulting $T_{c,on}$ and ΔT_c . The optimal conditions correspond to the film shown in panel (c).

tions. For samples annealed for at least 1 min at film surface temperatures of 550°C to 650°C, the film morphology exhibited domains or lamellar structures [Figs. 91.37(a) and 91.37(b), respectively] and their maximal $T_{c,on}$ was only 20 K and 30 K, respectively. The film presented in Fig. 91.37(b) showed signs of heat-induced substrate damage and its ΔT_c was very wide. After extensive trial-and-error studies, we realized that the best annealing conditions consisted of pre-heating at 300°C and only very brief, 30-s heating at 600°C, followed by post-heating for 60 s again at 300°C. The films produced in this manner were characterized by very smooth surfaces [Fig. 91.37(c)], without domains, cracks, or lamellar structures. X-ray diffraction exhibited no diffraction peaks, indicating an amorphous phase analogous to that of similar post-annealed MgB_2 films prepared on Si and sapphire substrates from Mg-B precursors.⁶

The homogeneity of our thin films was studied by Auger spectroscopy. The Auger spectra (Fig. 91.38) show a strong non-stoichiometry of Mg and B on the film surface, as well as an enhanced content of oxygen and presence of carbon. The damaged surface layer was only ~ 20 nm thick, however, as estimated by the rate of Mg-B etching and scanning electron microscopy studies. The bulk of the film had a uniform 1:2 stoichiometry ratio, with only small oxygen content, apparently from the residual oxygen in the annealing vacuum chamber.

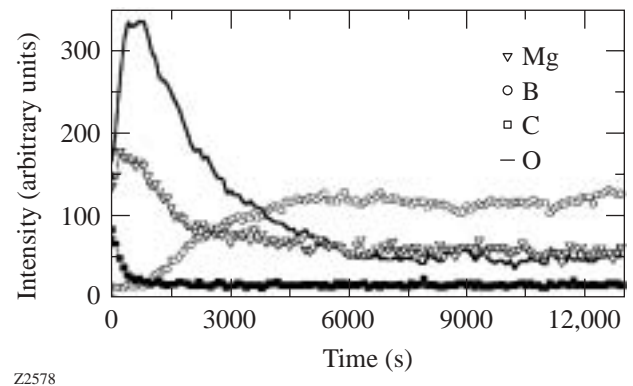
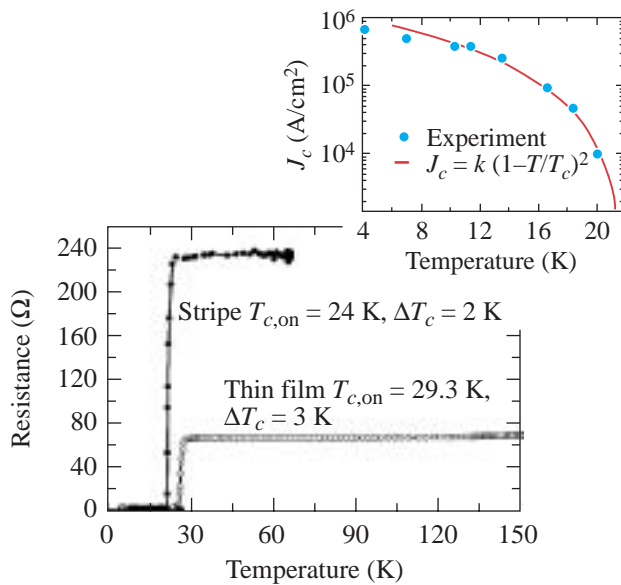


Figure 91.38 The depth profile of an optimally annealed [Fig. 91.37(c)] MgB_2 film, obtained from the Auger measurement.

The films prepared according to the annealing recipe shown in Fig. 91.37(c) also had the best superconducting properties. The maximal $T_{c,on}$ obtained was 29.3 K, as shown in Fig. 91.39, where we plotted the resistive superconducting transitions for both the stripe cut from a film by scissors and the one patterned by photolithography and Ar-ion etching. The

cut stripe was approximately 1 mm wide and its superconducting properties are representative of our plain MgB_2 films, while the patterned bridge was $10\ \mu\text{m}$ wide and $120\ \mu\text{m}$ long. We note that Ar-ion etching resulted in a slight reduction of $T_{c,on}$; at the same time, however, ΔT_c was decreased to 2 K. The patterned microbridge was also used for J_c measurements. The inset in Fig. 91.39 shows the J_c dependence on temperature, together with the fit based on $J_c(T) = k(1-T/T_c)^\alpha$, where k is a constant and α is a fitting parameter. The fit shown in Fig. 91.39 was obtained for $\alpha = 2$ and indicates that our film is granular with a network of superconductor-normal metal-superconductor (SNS) weak links.^{11,12} At 4.2 K, J_c reached a value $>7 \times 10^5\ \text{A/cm}^2$.



Z2579

Figure 91.39

Resistance versus temperature characteristics of an optimally annealed MgB_2 film (open circles) and the photolithographically patterned MgB_2 microbridge (closed circles). The inset shows the $J_c(T)$ dependence measured for a small microbridge, together with the theoretical fit illustrating the SNS, weak-link dependence.

Conclusion

In conclusion, the preparation of superconducting MgB_2 thin films on flexible plastic foils has been presented. Our films were amorphous and exhibited a very smooth surface. The films were annealed under optimal conditions, using rapid radiative (halogen lamps) heating of Mg-B and simultaneous water-cooling of the Kapton foil, and were characterized by $T_{c,on}$ of about 29 K, ΔT_c of about 3 K, and $J_c > 7 \times 10^5\ \text{A/cm}^2$ at 4.2 K. The measured $J_c(T)$ characteristics indicated the

presence of a SNS weak-link network in the films. The Auger measurement showed that besides the $\sim 20\text{-nm}$ -thick film surface, the bulk of the film exhibited a fully stoichiometric composition of Mg and B. Finally, we note that our rapid annealing procedure prevented any substrate degradation and is suitable for high-temperature annealing of thin films prepared on substrates unstable at high temperatures.

ACKNOWLEDGMENT

The authors thank E. Dobrocka for help in x-ray diffraction, M. Zahoran for scanning electron microscopy, and M. Gregor for the Auger spectroscopy studies. This work was supported by the Slovak Grant Agency for Science, Grants No. 2/7072/2000 and 2/7199/2000, US NSF grant DMR-0073366, and by the NAS COBASE 2000 Program, supported by the contract INT-0002341 from NSF.

REFERENCES

1. J. Nagamatsu *et al.*, *Nature* **410**, 63 (2001).
2. M. Angst *et al.*, *Phys. Rev. Lett.* **88**, 167004 (2002).
3. C. B. Eom *et al.*, *Nature* **411**, 558 (2001).
4. H. Y. Zhai *et al.*, *J. Mater. Res.* **16**, 2759 (2001).
5. D. H. A. Blank *et al.*, *Appl. Phys. Lett.* **79**, 394 (2001).
6. W. N. Kang *et al.*, *Science* **292**, 1521 (2001).
7. A. Plecenik *et al.*, *Physica C* **363**, 224 (2001).
8. X. H. Zeng *et al.*, *Appl. Phys. Lett.* **79**, 1840 (2001).
9. H.-J. Kim *et al.*, *Phys. Rev. Lett.* **87**, 087002 (2001).
10. A. H. Li *et al.*, *Physica C* **361**, 73 (2001).
11. V. Ambegaokar and A. Baratoff, *Phys. Rev. Lett.* **10**, 486 (1963).
12. P. G. de Gennes, *Rev. Mod. Phys.* **36**, 225 (1964).

Time-Resolved Areal-Density Measurements with Proton Spectroscopy in Spherical Implosions

The goal of the inertial confinement fusion (ICF)^{1,2} implosion is to achieve high-enough temperature and compression of the fuel to sustain thermonuclear burn. The burn begins with spark ignition of the central hot spot² that is created as a result of shock heating and target compression. The burn wave then propagates into the higher-density regions of the compressed shell, releasing energy through the products of thermonuclear reactions.² The combination of high temperature and high density–radius product (called areal density or ρR) of the compressed target is necessary to ignite the target and achieve high gain.¹ In the direct-drive ignition target design³ for the National Ignition Facility (NIF),² a 3.4-mm-diam, 350- μm -thick cryogenic deuterium–tritium (DT) shell is imploded with 192 overlapped laser beams with a total energy of 1.5 MJ. The hot-spot areal density must be $\sim 300 \text{ mg/cm}^2$ at a temperature exceeding $\sim 10 \text{ keV}$ to ignite. The expected neutron yield of 2.5×10^{19} (corresponding to a gain of ~ 45) will be achieved at a fuel temperature of $\sim 30 \text{ keV}$ and a target areal density of $\sim 1200 \text{ mg/cm}^2$ at peak compression. Areal densities measured so far in cryogenic implosions^{4–7} are far below the values necessary for ignition because far-lower laser energy is used and the unstable growth of target perturbations inhibits achieving the desired compression. In recent implosions on the 60-beam, 351-nm OMEGA laser system, areal densities of $\sim 40 \text{ mg/cm}^2$ have been achieved with cryogenic D_2 targets and laser energies of $\sim 23 \text{ kJ}$.⁷

Because of the technical complexity associated with cryogenic equipment, most ICF implosions use plastic or glass shells filled with different gases, allowing a large variety of diagnostics to be used in experiments. Indirect-drive implosions on the Nova laser achieved $\sim 15 \text{ mg/cm}^2$ of gas and $\sim 70 \text{ mg/cm}^2$ of shell areal densities, respectively.⁸ Recent studies on OMEGA reported up to $\sim 15 \text{ mg/cm}^2$ of gas and $\sim 60 \text{ mg/cm}^2$ of shell areal densities measured with charged-particle diagnostics.⁹ Measurements using shell absorption of x rays emitted from the hot core reported¹⁰ shell areal densities up to $\sim 100 \text{ mg/cm}^2$. The highest reported values of areal densities, up to $\sim 1 \text{ g/cm}^2$, are from implosions on the GEKKO XII laser system.¹¹

To date, all reported values of target compression are time averaged over the neutron and charged-particle production. During this time, the target areal density is expected to grow by an order of magnitude or more. Time-integrated particle spectra (used to measure average areal densities) clearly show signatures of time evolution. For example, in OMEGA experiments with 24- μm -thick shells filled with 18 atm of D^3He gas, primary proton spectra have two distinctive features from shock and compression phases of implosion.¹² These features are produced when target areal densities differ by a factor of ~ 10 , with a corresponding time difference of $\sim 500 \text{ ps}$. This article describes experiments where the measured neutron production histories combined with primary 14.7-MeV proton spectra of D^3He fuel allows the first determination of areal-density *growth* during the time of neutron production up to peak compression. These measurements become possible when all other aspects contributing to the shape of the proton spectrum, such as geometrical broadening from the finite size of the proton-production region, broadening from small-scale target nonuniformities, and ion temperature broadening, are taken into account. In this article we not only present for the first time target-areal-density evolution, a fundamental quantity for ICF, but also provide areal-density growth measurements for the study of unstable growth of target perturbations, an area of the utmost importance to the success of ICF.

The experiment consisted of two direct-drive implosions on the 60-beam OMEGA laser system.¹³ The targets were $\sim 950\text{-}\mu\text{m}$ -initial-diam, 20- μm -thick plastic CH shells filled with 18 atm (shot 25220) and 4 atm (shot 25219) of D^3He gas. Neutron-production histories from the reaction $\text{D} + \text{D} \rightarrow {}^3\text{He}(0.82 \text{ MeV}) + n(2.45 \text{ MeV})$ were measured with the neutron temporal diagnostic (NTD).¹⁴ Proton spectra from the reaction $\text{D} + {}^3\text{He} \rightarrow {}^4\text{He}(3.6 \text{ MeV}) + p(14.7 \text{ MeV})$ have been measured with seven wedged-range filters (WRF's)¹⁵ to ensure approximately uniform coverage of the target. The shapes of the time-integrated proton spectra depend primarily on the evolution of the target areal density and the temporal history of proton production (which is approximately proportional to the measured neutron-production history). Impl-

sions of targets with an equivalent mass of D₂ and DT fuels provide values of neutron yield and ion temperature (measured using scintillator detectors), neutron burn width (using the neutron bang-time detector),¹⁴ and average fuel areal density (from detection of knock-on deuterons),⁹ which together are used to estimate sizes of particle production and fuel regions at peak neutron production. These sizes are required to determine the extent of geometrical and temperature broadening contributions to the shapes of proton spectra. Results from equivalent implosions with shells having titanium-doped layers provide measurements of areal-density modulations (by means of differential imaging),¹⁶ which also contribute to the widths of the proton spectra. The targets were imploded with a 1-ns square pulse with a total on-target energy of ~23 kJ. All laser beams were smoothed with distributed phase plates,¹⁷ 1-THz, two-dimensional smoothing by spectral dispersion,¹⁸ and polarization smoothing¹⁹ using birefringent wedges. The average beam-to-beam energy imbalance was about 3% to 4%.

Figure 91.40 shows the results of a simulation of shot 21240, which had a 12-atm-D³He fill, performed with the 1-D hydrocode *LILAC*;²⁰ these results were used to develop and test a fitting method to determine the areal-density evolution. Protons born in nuclear reactions [Fig. 91.40(a)] are slowed down by the plasma of the gas fuel and plastic shell [the simulated areal-density evolution is shown by a solid curve in

Fig. 91.40(b)] on the way out from the target core to the detector. The energies of protons leaving the target are calculated using the Bethe–Bloch stopping power²¹ relation, which depends very weakly on the plasma density and temperature. The slowing-down curve shown in Fig. 91.40(c) has been calculated for a fully ionized CH plasma with an electron density of 10²⁵ cm⁻³ (corresponding to plastic density of ~35 g/cm³) and a temperature of 0.5 keV. The proton spectrum [Fig. 91.40(d), solid line] represents the integral of the protons born and slowed down by the target. The resulting proton spectrum is additionally broadened by the core ion temperature of 3.4 keV and geometrical effects, discussed below.

The areal-density evolution is inferred by fitting a constructed spectrum $P_c(E)$ to the measured $P_m(E)$ proton spectrum. The spectrum $P_c(E)$ is constructed using the measured neutron-production rate (assumed to be proportional to the proton-production rate) and the target areal density ρR_t , assumed to have a Lorentzian form as a function of time t :

$$\rho R_t(t) = C_0 / \left[(t - C_1)^2 + (C_2/2)^2 \right].$$

The best fit is achieved using a χ^2 minimization of the deviation between $P_c(E)$ and $P_m(E)$ by varying three fitting parameters C_0 , C_1 , and C_2 . The sensitivity and systematic errors of

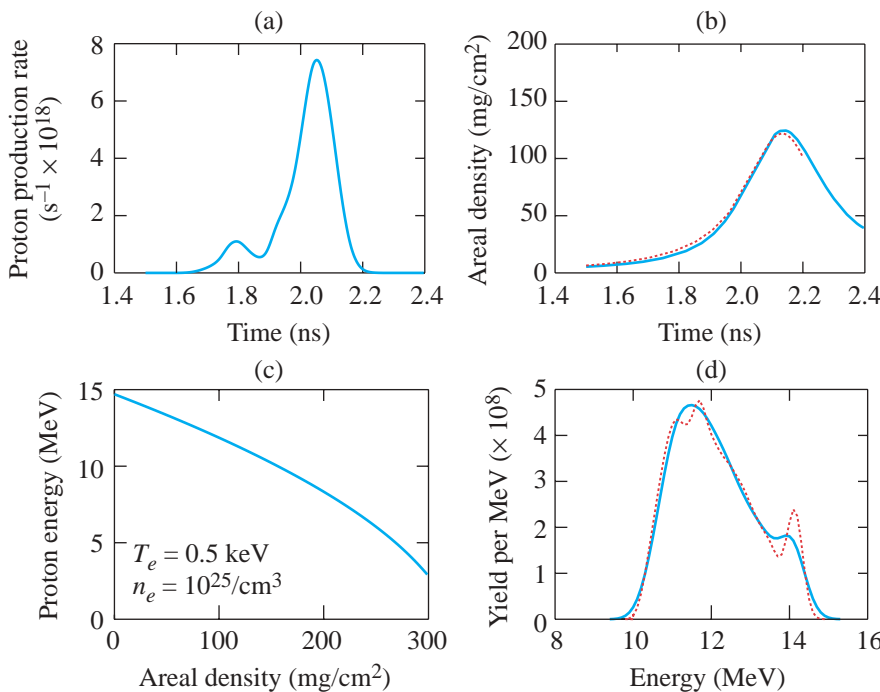


Figure 91.40
The results of 1-D *LILAC* simulations (solid lines) and the calculated fit (dashed lines) for shot 21240: (a) the proton-production history; (b) the target-areal-density evolution; (c) the proton energy versus target areal density calculated using Bethe–Bloch stopping power for an electron density of 10²⁵/cm³ and a temperature of 0.5 keV; and (d) the proton energy spectra.

E11659

this method have been tested with the simulation results shown in Fig. 91.40 by comparing the fit with the simulated areal-density evolution. The dashed lines in Figs. 91.40(b) and 91.40(d) show that a good fit for the yield is achieved when the fitted areal-density evolution is very close to the actual. This method is very sensitive because even small (10% at $\sim 100 \text{ mg/cm}^2$) variations in areal density result in sizable deviations ($\sim 0.5 \text{ MeV}$) in the proton spectrum. The fitting assumes that the ion temperature, size of the core, shell, production region, and stopping power do not change in time. The uncertainties of these approximations are included in the systematic errors discussed below.

Geometrical broadening effects are described schematically in Fig. 91.41(a), and the resulting broadening shapes are shown in Fig. 91.41(b). In these calculations the gas fuel occupies a spherical region of radius R_2 and a proton-producing

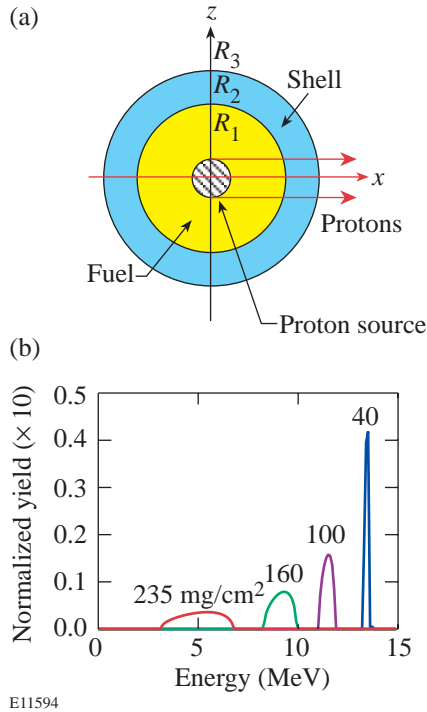


Figure 91.41
The geometrical broadening effects. Panel (a) shows the target schematic. The proton-production region has a radius of R_1 , the gas fuel has a radius of R_2 , and the shell has a thickness of $R_3 - R_2$. The protons travel to a distant detector in the direction of the x axis. Panel (b) shows the geometrically broadened shapes, as normalized 14.7-MeV proton spectra after passing through shells with areal densities of 40, 100, 160, and 235 mg/cm^2 , calculated for $R_1 = 27 \mu\text{m}$, $R_2 = 33 \mu\text{m}$, and $R_3 = 63 \mu\text{m}$.

region of radius R_1 . On the way to the distant detector, protons lose their energy primarily in the shell of thickness $R_3 - R_2$. Protons that are born on the x axis (which passes through the core center and the detector) always leave the target in a direction normal to the shell, while protons that are born off this axis penetrate the shell at some angle to the shell normal. As a result, even for an undistorted shell, the protons reaching the detector will have an energy spectrum broader than that originally emitted from the production region since the amount of proton energy loss depends on the path length in the shell. Figure 91.41(b) shows spectra of monoenergetic protons after passing a uniform shell of various areal densities for a target with $R_1 = 27 \mu\text{m}$, $R_2 = 33 \mu\text{m}$, and $R_3 = 63 \mu\text{m}$, taken from the *LILAC* simulation presented in Fig. 91.40. The number of protons reaching the detector in the x direction as a function of coordinate z ($0 \leq z \leq R_1$) have the distribution

$$F(z) = Cz\sqrt{R_1^2 - z^2},$$

where C is a constant derived using the target geometry shown in Fig. 91.41(a). The effective areal density seen by the protons going to the detector as a function of z is

$$\rho R_{\text{eff}}(z) = \rho \left(\sqrt{R_3^2 - z^2} - \sqrt{R_2^2 - z^2} \right).$$

Substituting z for ρR_{eff} in the expression for $F(z)$ and converting areal density to proton energy using Fig. 91.40(c) results in the geometrically broadened shapes shown in Fig. 91.41(b). The original monoenergetic proton spectrum shifts to lower proton energies and broadens as a result of geometrical effects. For each shot, the parameters R_1 , R_2 , and R_3 have been calculated using experimental results from a large number of shots with fills having an equivalent mass of D_2 and DT . For example, in implosions with 15-atm- D_2 fuel (mass equivalent to 18 atm of D^3He), $R_2 = 36 \mu\text{m}$ has been calculated using conservation of fuel mass ($8.3 \times 10^{-7} \text{ g}$) and measured fuel areal density ($\sim 15 \text{ mg/cm}^2$). In order to match the experimental neutron yield of $\sim 1.6 \times 10^{11}$, the particle-production volume must have $R_1 = 22 \mu\text{m}$ with a measured ion temperature of $\sim 3.7 \text{ keV}$ and a neutron burn width of $\sim 170 \text{ ps}$. In an implosion with 3-atm- D_2 fuel (mass equivalent to 4 atm of D^3He), radii of $R_1 = 25 \mu\text{m}$ and $R_2 = 32 \mu\text{m}$ were calculated based on the fuel mass of $1.67 \times 10^{-7} \text{ g}$, fuel areal density of $\sim 4 \text{ mg/cm}^2$, neutron yield of $\sim 6.6 \times 10^{10}$, ion temperature of $\sim 5 \text{ keV}$, and neutron burn width of $\sim 150 \text{ ps}$. The shell thickness $R_3 - R_2$, the most-insensitive parameter on fitting results, has been taken to be $30 \mu\text{m}$ for both types of implosions.

Figure 91.42 shows the proton spectrum fitting results for shot 25220 with 18 atm of D^3He gas for seven detectors, which provided approximately uniform coverage of the shell. Inferred areal-density time histories for all seven directions are shown by the solid lines in Fig. 91.42(h) together with the neutron-production history (dotted line). The additional small effect of short-scale (with mode number $\ell > 6$) areal-density nonuniformities on proton spectrum broadening has been corrected by reducing the areal density shown in Fig. 91.42 by 7% with the uncertainty ranging from 0% to 15% included in the error bars: Differential imaging measurements¹⁶ of inner-shell, titanium-doped layers show areal-density perturbation levels of $\sim 15\%$ at peak neutron production. In the whole shell these values are about $\sim 7\%$, as calculated by 2-D simulations,¹⁶ because the whole shell is more uniform than the inner layer, which is unstable during the deceleration phase of the implosion. The constant correction due to this effect is a good approximation (even though the measured shell modulations grow throughout the implosion) since its contribution to spectral broadening is maximum at peak neutron production and lower at peak compression because of lower amount of protons contributing to it. In experiments, $\sim 70\%$ of total proton spectrum width is due to the areal-density evolution, $\sim 20\%$ is due

to geometrical effects, and the remaining $\sim 10\%$ is due to temperature, short-scale (with mode number $\ell > 6$) areal-density perturbations, and instrumental broadening. A discussion of the experimental error analysis is presented in Appendix A.

Figure 91.43 summarizes the results for shots with (a) 18-atm- and (b) 4-atm- D^3He fills and compares them with 1-D *LILAC* predictions. The more-stable 18-atm-fill shot has a measured peak areal density of $109 \pm 14 \text{ mg/cm}^2$ (thick solid line), which is close to the 1-D simulation result (thin solid line); however, the more-unstable 4-atm shot has a measured peak areal density of $123 \pm 16 \text{ mg/cm}^2$, much lower than the 1-D simulation result of 230 mg/cm^2 . During neutron production (from 1.6 to 2.0 ns), the areal density grows by a factor of ~ 8 in the 4-atm shot. At peak compression, the areal-density asymmetries with low mode numbers $\ell \leq 6$ are $\sim 10\%$ and $\sim 20\%$ for 18-atm- and 4-atm-fill targets, respectively, as estimated from the measured values in the seven detectors. The measured peak areal density is only about 10% higher for the 4-atm-fill target than that of the 18-atm-fill target. This is consistent with core sizes of $R_2 = 32 \text{ }\mu\text{m}$ and $36 \text{ }\mu\text{m}$, respectively, estimated using neutron and particle measurements.

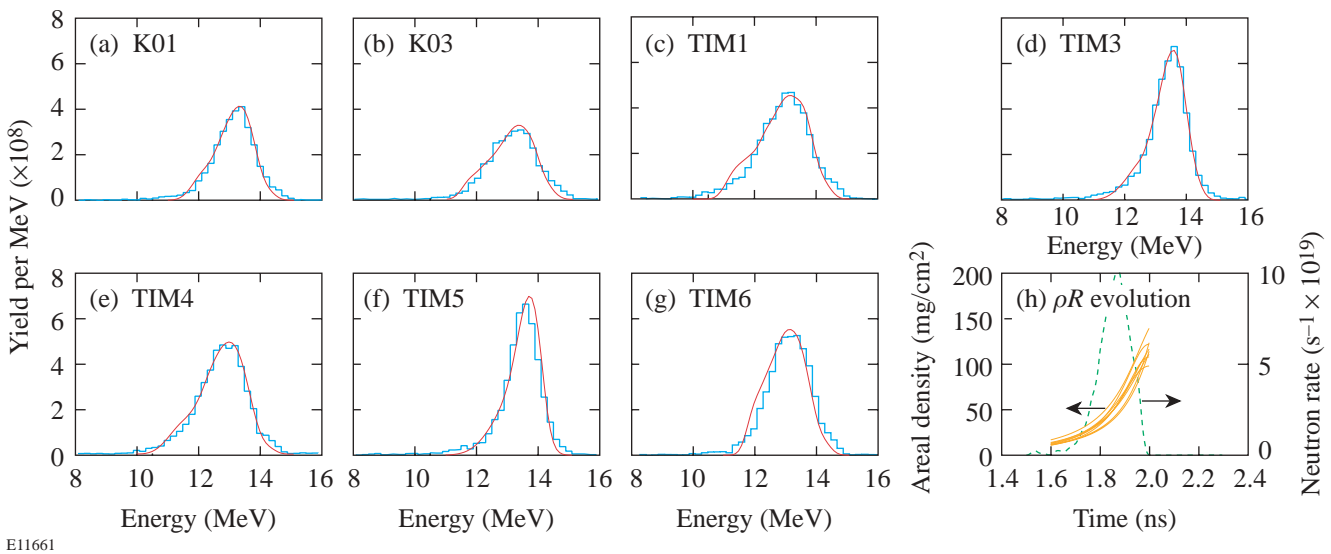


Figure 91.42

The proton spectra and fitting results (smooth solid lines) for shot 25220 with 18 atm of D^3He gas [(a)–(g)]. (h) Also shown is the inferred areal-density evolution in seven directions (solid lines) and the neutron-production history (dotted line) for this shot.

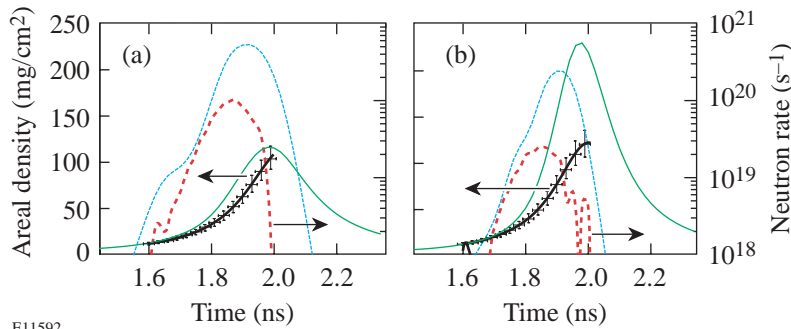


Figure 91.43

The measured (thick) and simulated (thin) target areal-density evolutions (solid) and neutron-production histories (dashed) for shots with (a) 18-atm and (b) 4-atm gas fills.

E11592

In conclusion, the target areal density grows by a factor of ~ 8 during the time of neutron production (~ 400 ps) before reaching 123 ± 16 mg/cm² at peak compression in the shot with a 20- μ m-thick plastic CH target filled with 4 atm of D³He fuel. This value is lower by a factor of ~ 2 than the 1-D simulation result of 230 mg/cm². For the more-stable, 18-atm-fill target, the target areal density reaches 109 ± 14 mg/cm² at peak compression, close to the 1-D prediction of 115 mg/cm².

ACKNOWLEDGMENT

This work was supported by the U.S. Department of Energy Office of Inertial Confinement Fusion under Cooperative Agreement No. DE-FC03-92SF19460, the University of Rochester, and the New York State Energy Research and Development Authority. The support of DOE does not constitute an endorsement by DOE of the views expressed in this article.

Appendix A

The errors in the areal-density evolution measurements include systematic errors calculated from the sensitivity analysis of the fitting results and statistical errors of measured proton spectra. The biggest systematic error is the uncertainty in plasma conditions that affect proton stopping power. The relevant error is about ± 0.5 MeV at a proton energy of 10 MeV, which translates to an areal-density uncertainty of $\pm 10\%$ at 100 mg/cm². The use of neutron instead of proton-production history resulted in a 24-ps temporal shift of the areal-density evolution. The assumption that the proton-production size R_1 is constant during proton production gives an uncertainty of ± 0.3 MeV at 10 MeV, which translates to an areal-density uncertainty of $\pm 6\%$ at 100 mg/cm². The uncertainty in the other geometrical parameters R_2 and R_3 are negligibly small in the present analysis. The additional uncertainty due to possible ion-temperature evolution is also calculated to be negligible compared to other errors. The statistical errors due to the noise in the proton spectra, neutron-production history, and the errors in the fitting parameters C_0 , C_1 , and C_2 have been estimated to be ± 0.5 MeV at 10 MeV, which translates to an areal-

density uncertainty of $\pm 10\%$ at 100 mg/cm². Averaging over seven independent measurements makes them even smaller.

REFERENCES

1. J. Nuckolls *et al.*, *Nature* **239**, 139 (1972).
2. J. D. Lindl, *Phys. Plasmas* **2**, 3933 (1995).
3. P. W. McKenty, V. N. Goncharov, R. P. J. Town, S. Skupsky, R. Betti, and R. L. McCrory, *Phys. Plasmas* **8**, 2315 (2001).
4. R. R. Johnson *et al.*, *Phys. Rev. A* **41**, 1058 (1990).
5. F. J. Marshall, S. A. Letzring, C. P. Verdon, S. Skupsky, R. L. Keck, J. P. Knauer, R. L. Kremens, D. K. Bradley, T. Kessler, J. Delettrez, H. Kim, J. M. Soures, and R. L. McCrory, *Phys. Rev. A* **40**, 2547 (1989).
6. K. A. Tanaka *et al.*, *Phys. Plasmas* **2**, 2495 (1995).
7. C. Stoeckl, C. Chiritescu, J. A. Delettrez, R. Epstein, V. Yu. Glebov, D. R. Harding, R. L. Keck, S. J. Loucks, L. D. Lund, R. L. McCrory, P. W. McKenty, F. J. Marshall, D. D. Meyerhofer, S. F. B. Morse, S. P. Regan, P. B. Radha, S. Roberts, T. C. Sangster, W. Seka, S. Skupsky, V. A. Smalyuk, C. Sorce, J. M. Soures, R. P. J. Town, J. A. Frenje, C. K. Li, R. D. Petrasso, F. H. Séguin, K. Fletcher, S. Padalino, C. Freeman, N. Izumi, R. Lerche, and T. W. Phillips, *Phys. Plasmas* **9**, 2195 (2002).
8. M. D. Cable *et al.*, *Phys. Rev. Lett.* **73**, 2316 (1994).
9. C. K. Li, F. H. Séguin, D. G. Hicks, J. A. Frenje, K. M. Green, S. Kurebayashi, R. D. Petrasso, D. D. Meyerhofer, J. M. Soures, V. Yu. Glebov, R. L. Keck, P. B. Radha, S. Roberts, W. Seka, S. Skupsky, C. Stoeckl, and T. C. Sangster, *Phys. Plasmas* **8**, 4902 (2001).
10. F. J. Marshall, J. A. Delettrez, V. Yu. Glebov, R. P. J. Town, B. Yaakobi, R. L. Kremens, and M. Cable, *Phys. Plasmas* **7**, 1006 (2000).
11. H. Azechi *et al.*, *Laser Part. Beams* **9**, 193 (1991).
12. R. D. Petrasso, F. H. Séguin, J. A. Frenje, C. K. Li, J. R. Rygg, B. E. Schwartz, S. Kurebayashi, P. B. Radha, C. Stoeckl, J. M. Soures, J. Delettrez, V. Yu. Glebov, D. D. Meyerhofer, and T. C. Sangster, "Measuring Implosion Dynamics through ρR Evolution in Inertial Confinement Fusion Experiments," submitted to *Phys. Rev. Lett.*

13. T. R. Boehly, D. L. Brown, R. S. Craxton, R. L. Keck, J. P. Knauer, J. H. Kelly, T. J. Kessler, S. A. Kumpan, S. J. Loucks, S. A. Letzring, F. J. Marshall, R. L. McCrory, S. F. B. Morse, W. Seka, J. M. Soures, and C. P. Verdon, *Opt. Commun.* **133**, 495 (1997).
14. R. A. Lerche, D. W. Phillion, and G. L. Tietbohl, *Rev. Sci. Instrum.* **66**, 933 (1995).
15. F. H. Séguin, C. K. Li, D. G. Hicks, J. A. Frenje, K. M. Green, R. D. Petrasso, J. M. Soures, D. D. Meyerhofer, V. Yu. Glebov, C. Stoeckl, P. B. Radha, S. Roberts, C. Sorce, T. C. Sangster, M. D. Cable, S. Padalino, and K. Fletcher, *Phys. Plasmas* **9**, 2725 (2002).
16. V. A. Smalyuk, J. A. Delettrez, V. N. Goncharov, F. J. Marshall, D. D. Meyerhofer, S. P. Regan, T. C. Sangster, R. P. J. Town, and B. Yaakobi, *Phys. Plasmas* **9**, 2738 (2002).
17. Y. Lin, T. J. Kessler, and G. N. Lawrence, *Opt. Lett.* **20**, 764 (1995).
18. S. P. Regan, J. A. Marozas, J. H. Kelly, T. R. Boehly, W. R. Donaldson, P. A. Jaanimagi, R. L. Keck, T. J. Kessler, D. D. Meyerhofer, W. Seka, S. Skupsky, and V. A. Smalyuk, *J. Opt. Soc. Am. B* **17**, 1483 (2000).
19. T. R. Boehly, V. A. Smalyuk, D. D. Meyerhofer, J. P. Knauer, D. K. Bradley, R. S. Craxton, M. J. Guardalben, S. Skupsky, and T. J. Kessler, *J. Appl. Phys.* **85**, 3444 (1999).
20. J. Delettrez, R. Epstein, M. C. Richardson, P. A. Jaanimagi, and B. L. Henke, *Phys. Rev. A* **36**, 3926 (1987).
21. T. A. Mehlhorn, *J. Appl. Phys.* **52**, 6522 (1981).

Multipolar Interband Absorption in a Semiconductor Quantum Dot: Electric Quadrupole Enhancement

Introduction

A quantum dot is an artificially created semiconductor structure in the size range of 5 to 100 nm. As a whole, it behaves like an atom since the quantum effects of the confined electrons are enlarged with respect to the interactions of the electrons inside each atom. Since the conception of quantum dots in the early 1980s, the study of their physical properties continues to be a very active field of research. Quantum dots can now be synthesized by various methods and have a multitude of potential technological applications, which include lasers with high optical gain and narrow bandwidth, and wavelength tunability.¹ Also, dipole–dipole interaction between neighboring quantum dots is being explored for applications in quantum computing.² Furthermore, quantum dots are potential single-photon sources, which may be used to create nonclassical electromagnetic states.³

Near-field optical techniques have extended the range of optical measurements beyond the diffraction limit and stimulated interests in many disciplines, especially material sciences and biological sciences.^{4,5} Spatial resolution is increased by accessing evanescent modes in the electromagnetic field. These modes are characterized by high spatial frequencies and therefore enable the probing of subwavelength structures. Near-field optical techniques have also been employed to study the optical properties and dynamics of charge carriers in artificial nanostructures such as quantum wells, quantum wires, and quantum dots (see, for example, Refs. 6–8).

Nanostructures interacting with optical near fields do not necessarily behave in the same way as nanostructures interacting with far-field radiation. In Ref. 9, for example, the response of a quantum well when excited by the diffracted field of an aperture enhances quadrupole transitions, giving rise to a modified absorption spectrum of the quantum well. Furthermore, absorption properties may also be modified due to nonlocal spatial dispersion as described in Ref. 10. Recently, Knorr *et al.* formulated a general theoretical, self-consistent multipolar formalism for solids. This formalism can even be extended to account for delocalized charges.¹¹ The spectral

response originating from the interaction between semiconductor quantum dots and the optical field generated by a small aperture has been discussed in Refs. 12–14. References 13 and 14 account for the highly inhomogeneous excitation field produced by the subwavelength aperture.

This article focuses on the interaction of a spherical semiconductor quantum dot with a highly confined optical near field. It has been shown that such fields can be generated near laser-illuminated, sharp-pointed tips.^{15–17} Here, we adopt this geometry and approximate the fields near the tip by an oscillating electric dipole oriented along the tip axis. In Ref. 18, it has been demonstrated that this is a reasonable approximation and that the dipole moment can be related to the computationally determined field-enhancement factor. Furthermore, our analysis relies only on the field distribution and not on the actual enhancement factor. We will consider a spherical quantum dot in the strong-confinement limit.

The interaction between a quantum dot and the optical near field is described semiclassically using the multipolar expansion. For far-field excitation, the first term in this expansion, the electric dipole term, gives rise to a response that is considerably stronger than the response produced by subsequent terms. This is due to the fact that the physical dimension of the quantum dot is much smaller than the wavelength of optical radiation and also due to the weak spatial variation of the exciting far field. The spatial variations of optical near fields, however, are much stronger, and, as a consequence, it is expected that the contribution of higher terms in the multipolar expansion cannot *a priori* be neglected. In this article, the strength of electric quadrupole absorption compared with the strength of the electric dipole absorption will be analyzed. This study is motivated by two basic questions: (1) To what extent are standard selection rules modified by higher-order multipolar transitions in confined optical fields? and (2) Can optical resolution be improved by selectively exciting higher-order multipole transitions? To keep the analysis as simple as possible, we will neglect the Coulomb interaction between hole and electron as well as the spin of these particles.

The article is organized as follows: In the next section, the semiclassical multipolar Hamiltonian formalism is presented. In the same section, the wave functions for the hole and the electron in an ideal spherical quantum dot are reviewed, and the field operator representation is outlined. In subsequent sections, the absorption rate in the electric dipole approximation is discussed, and the absorption rate arising from the electric quadrupole term in the multipolar expansion is derived. The theory is applied to a quantum dot near a laser-illuminated metal tip. Approximated parameters for GaAs are used to estimate the absorption rate for electric dipole transitions and electric quadrupole transitions. In the last section, results are discussed and conclusions and future work are presented.

Preliminary Concepts

1. The Multipolar Hamiltonian

A semiclassical approach is used to describe the interaction of a quantum dot with the electromagnetic field. In this approach, the electromagnetic field obeys the Maxwell equations, and the Hamiltonian of the system (\hat{H}) can be separated into two contributions as

$$\hat{H} = \hat{H}_0 + \hat{H}_I, \quad (1)$$

where \hat{H}_0 and \hat{H}_I are the unperturbed Hamiltonian (absence of fields) and the interaction Hamiltonian, respectively. In the Coulomb gauge, they are defined as

$$\hat{H}_0 = \frac{1}{2m} \hat{\mathbf{p}}^2 + V(\mathbf{r}), \quad (2)$$

$$\hat{H}_I = -\frac{e}{m} \hat{\mathbf{p}} \cdot \mathbf{A}(\mathbf{r}, t) + \frac{e^2}{2m} \mathbf{A}^2(\mathbf{r}, t) + e\phi(\mathbf{r}, t), \quad (3)$$

where $V(\mathbf{r})$ is the potential energy, $\hat{\mathbf{p}}$ is the canonical momentum, $\mathbf{A}(\mathbf{r}, t)$ is the vector potential, and $\phi(\mathbf{r}, t)$ is the scalar potential. The multipolar Hamiltonian is obtained by using the canonical transformation $\hat{U} = \exp(iz/\hbar)$ in which z is given by^{19,20}

$$z = \int \tilde{\mathbf{P}}(\mathbf{r}) \cdot \mathbf{A}(\mathbf{r}, t) d^3r \equiv 0, \quad (4)$$

where $\tilde{\mathbf{P}}(\mathbf{r})$ is the polarization. If the vector potential $\mathbf{A}(\mathbf{r}, t)$ and the scalar potential $\phi(\mathbf{r}, t)$ are expanded in a Taylor series

with respect to a reference charge distribution at \mathbf{R} as follows:

$$\mathbf{A}(\mathbf{r}, t) = \sum_{n=0}^{\infty} \frac{1}{(n+2)n!} [(\mathbf{r}-\mathbf{R}) \cdot \nabla]^n \mathbf{B}(\mathbf{R}, t) \cdot (\mathbf{r}-\mathbf{R}), \quad (5)$$

$$\phi(\mathbf{r}, t) = \sum_{n=0}^{\infty} \frac{-1}{(n+1)!} (\mathbf{r}-\mathbf{R}) [(\mathbf{r}-\mathbf{R}) \cdot \nabla]^n \cdot \mathbf{E}(\mathbf{R}, t), \quad (6)$$

then this choice of $\mathbf{A}(\mathbf{r}, t)$ and $\phi(\mathbf{r}, t)$ satisfies condition (4). By substituting Eqs. (5) and (6) into Eq. (3), we obtain

$$\hat{H}_I = \hat{H}^E + \hat{H}^M + \hat{H}^Q + \dots \quad (7)$$

Here \hat{H}^E , \hat{H}^M , and \hat{H}^Q are the first three terms of the multipolar expansion, namely, the electric dipole, the magnetic dipole, and the electric quadrupole, respectively, which are defined as

$$\hat{H}^E = -\mathbf{d} \cdot \mathbf{E}(\mathbf{r}, t) \Big|_{\mathbf{r}=\mathbf{R}}, \quad (8a)$$

$$\hat{H}^M = -\mathbf{m} \cdot \mathbf{B}(\mathbf{r}, t) \Big|_{\mathbf{r}=\mathbf{R}}, \quad (8b)$$

$$\hat{H}^Q = -\nabla_1 \cdot \vec{\mathbf{Q}} \mathbf{E}(\mathbf{r}_1, t) \Big|_{\mathbf{r}_1=\mathbf{R}}, \quad (8c)$$

where \mathbf{d} , \mathbf{m} , and $\vec{\mathbf{Q}}$ are the electric dipole moment, the magnetic dipole moment, and the electric quadrupole moment, respectively, with respect to a reference charge distribution at \mathbf{R} . The nabla operator ∇_1 acts only on the spatial coordinates \mathbf{r}_1 of the electric field. It is important to mention that \mathbf{m} depends on the canonical momentum. For weak fields, however, the canonical momentum can be approximated as the mechanical momentum.

2. The Quantum Dot Wave Functions (Strong Confinement)

We assume that a spherical quantum dot is made of a direct band-gap semiconductor for which the bulk electric dipole transitions are allowed between the valence band and the conduction band. In a generic manner, we assume that the valence band has p -like character and the conduction band has s -like character. The latter assumption is commonly encountered for several semiconductors such as the GaAs. We consider that an electron and a hole are completely confined in a sphere with radius a by the potential energy

$$V(r) = \begin{cases} 0 & r \leq a, \\ \infty & r > a, \end{cases} \quad (9)$$

where r is the radial coordinate. Also, we assume that the electron (hole) has the same effective mass m_e (m_h) as in the bulk material. This consideration is valid if the volume of the sphere is much larger than the volume of a primitive cell in the crystal. Strong confinement is achieved if the Bohr radii of electron (b_e) and hole (b_h) are much larger than the radius of the quantum dot a . By assuming the aforementioned conditions, the wave function of the electron in the conduction band can be expressed as

$$\Psi^e(\mathbf{r}) = \frac{1}{\sqrt{V_0}} u_{c,0}(\mathbf{r}) \zeta^e(\mathbf{r}). \quad (10)$$

Here $u_{c,0}(\mathbf{r})$ is the conduction-band Bloch function (with lattice periodicity) having the corresponding eigenvalue $k=0$, and V_0 is the volume of the *unit cell*. Similarly, the corresponding wave function for the hole in the valence band is

$$\Psi^h(\mathbf{r}) = \frac{1}{\sqrt{V_0}} u_{v,0}(\mathbf{r}) \zeta^h(\mathbf{r}), \quad (11)$$

with $u_{v,0}(\mathbf{r})$ being the valence-band Bloch function with eigenvalue $k=0$. $\zeta^e(\mathbf{r})$ and $\zeta^h(\mathbf{r})$ are the envelope functions, which vary spatially much slower than $u_{v,0}(\mathbf{r})$ and $u_{c,0}(\mathbf{r})$. Roughly, the energy difference between adjacent electron {hole} energy levels is

$$\left(\frac{\hbar^2}{m_e a^2} \right) \left[\frac{\hbar^2}{(m_h a^2)} \right].$$

If this energy difference is much larger than the Coulomb interaction $e^2 / (4\pi\epsilon_0 \epsilon a^2)$, the electron-hole interaction can be neglected. Under this assumption, the envelope function $\zeta^{e(h)}(\mathbf{r})$ for the electron (hole) satisfies the time-independent Schrödinger equation in which the potential energy is given by Eq. (9). The solution in spherical coordinates (r, θ, ϕ) is given by

$$\zeta_{n,l,m}^{e(h)}(r, \theta, \phi) = \Lambda_{nl}(r) Y_{l,m}(\theta, \phi). \quad (12)$$

Here $Y_{l,m}(\theta, \phi)$ is the spherical harmonics and the radial function $\Lambda_{nl}(r)$ is

$$\Lambda_{nl}(r) = \sqrt{\frac{2}{a^3}} \frac{1}{j_{l+1}(\beta_{nl})} j_l\left(\beta_{nl} \frac{r}{a}\right). \quad (13)$$

j_l is the l^{th} -order spherical Bessel function, β_{nl} is the n^{th} root of j_l , i.e., $j_l(\beta_{nl}) = 0$. The corresponding energy levels $\epsilon^{e,h}$ are found to be

$$\epsilon^e = \epsilon_g + \frac{\hbar^2}{2m_e} \left(\frac{\beta_{nl}}{a} \right)^2, \quad (14)$$

$$\epsilon^h = \frac{\hbar^2}{2m_h} \left(\frac{\beta_{nl}}{a} \right)^2, \quad (15)$$

where ϵ_g is the bulk energy band gap. Figure 91.44 shows the resulting level scheme. According to Eqs. (14) and (15), the energy is independent of the quantum number m , thus the energy level nl is $(2l+1)$ -fold degenerate.

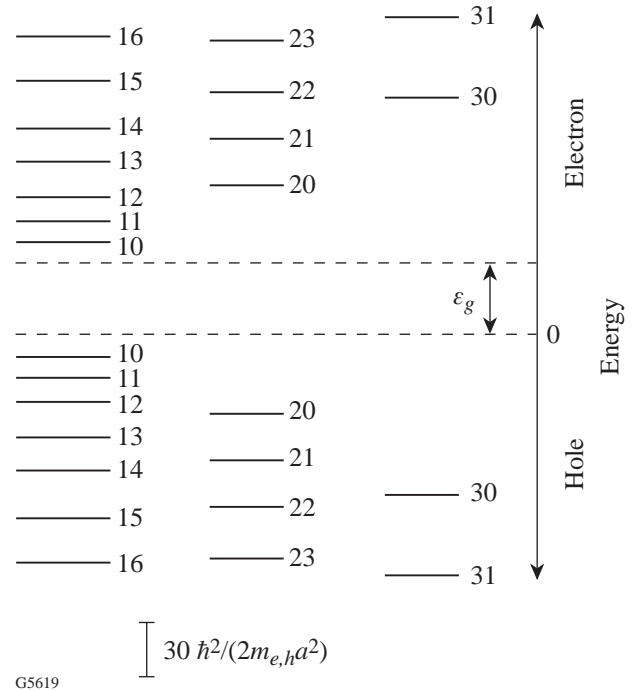


Figure 91.44
Energy level diagram of a spherical quantum dot according to Eqs. (14) and (15). Each energy level is characterized by the quantum numbers n and l , and its degeneracy corresponds to the quantum number m . Unlike the case of a hydrogen atom, the quantum number n does *not* restrict the number of suborbitals l .

3. Field Operator Representation

The annihilation carrier field operator $\hat{\Psi}$ can be expressed as a linear combination of hole creation operators in the valence band and electron annihilation operators in the conduction band, i.e.,^{21,22}

$$\hat{\Psi}(\mathbf{r}) = \sum_{n,l,m} \left[\frac{1}{\sqrt{V_0}} u_{c,0}(\mathbf{r}) \zeta_{nlm}^e(\mathbf{r}) \hat{f}_{nlm} + \frac{1}{\sqrt{V_0}} u_{v,0}(\mathbf{r}) \zeta_{nlm}^h(\mathbf{r}) \hat{g}_{nlm}^\dagger \right], \quad (16)$$

where \hat{f}_{nlm} is the annihilation operator for an electron in the conduction band with envelope function $\zeta_{nlm}^e(\mathbf{r})$. On the other hand, \hat{g}_{nlm}^\dagger is the creation operator for a hole in the valence band with envelope function $\zeta_{nlm}^h(\mathbf{r})$. The creation carrier field operator $\hat{\Psi}^\dagger$ is the adjoint of Eq. (16).

Absorption in the Electric Dipole Approximation

We consider a monochromatic electric field oscillating with frequency ω as

$$\mathbf{E}(\mathbf{r}, t) = \tilde{\mathbf{E}}(\mathbf{r}) e^{-i\omega t} + \text{c.c.} \quad (17)$$

Here $\tilde{\mathbf{E}}(\mathbf{r})$ is the spatial complex amplitude and ‘‘c.c.’’ means complex conjugate. By setting the origin O at the center of the quantum dot and using the rotating-wave approximation, the electric dipole transition rate α^E for photon absorption is^{21,22}

$$\alpha^E = K_e \sum_{nml} \sum_{rst} \tilde{\delta}_{nr} \tilde{\delta}_{ls} \tilde{\delta}_{mt} \delta \left[\hbar\omega - (\epsilon_{nl}^e + \epsilon_{rs}^h) \right], \quad (18)$$

where $\tilde{\delta}$ is the Kronecker delta, δ is the Dirac delta function, and K_e is the absorption strength given by

$$K_e = \frac{2\pi}{\hbar} e^2 |\tilde{\mathbf{E}}(\mathbf{0}) \cdot \mathbf{P}_{cv}|^2, \quad (19)$$

and

$$\mathbf{P}_{cv} = \frac{1}{V_0} \int_{\text{UC}} u_{c,0}^*(\mathbf{r}') \mathbf{r}' u_{v,0}(\mathbf{r}') d^3 r' = -\frac{\hbar}{m_0 \omega} \mathbf{m}_{cv}. \quad (20)$$

Here \mathbf{m}_{cv} is defined as

$$\mathbf{m}_{cv} \equiv \frac{1}{V_0} \int_{\text{UC}} u_{c,0}^*(\mathbf{r}') \nabla' u_{v,0}(\mathbf{r}') d^3 r', \quad (21)$$

with UC denoting the volume of the unit cell. In Eq. (20), we have used the fact that $\hat{\mathbf{r}} \equiv -i\hat{\mathbf{p}}/m_0\omega$ (m_0 and e are the rest mass and the charge of the electron, respectively). From Eq. (18), we notice that the absorption strength (K_e) depends *only* on the bulk material properties of the quantum dot. That is, it depends on the Bloch functions u_{c0} and u_{v0} and is not influenced by the envelope functions $\zeta_{nlm}^{e,h}(\mathbf{r})$. Also, Eq. (18) indicates that the allowed transitions are those for which electron and hole have the same quantum numbers, i.e.,

$$n = r \text{ and } l = s \text{ and } m = t.$$

These relationships define the selection rules for electric dipole transitions in a semiconductor quantum dot.

Absorption Arising from the Quadrupole Term

1. Electric Quadrupole Hamiltonian

The electric quadrupole interaction Hamiltonian \hat{H}^Q can be represented as

$$\hat{H}^Q = \int \hat{\Psi}^\dagger(\mathbf{r}) H^Q(\mathbf{r}) \Psi(\mathbf{r}) d^3 r, \quad (22)$$

$$H^Q(\mathbf{r}) = -\nabla_1 \cdot \vec{\mathbf{Q}}(\mathbf{r}) \mathbf{E}(\mathbf{r}_1, t) \Big|_{\mathbf{r}_1=0}, \quad (23)$$

where the $\vec{\mathbf{Q}}(\mathbf{r})$ is the quadrupole moment

$$\vec{\mathbf{Q}}(\mathbf{r}) = \frac{1}{2} \text{err}. \quad (24)$$

Here, and in the following, the subsequent listing of two vectors [as in Eq. (24)] denotes the outer product (dyadic product). The *interband* terms are found by substituting Eq. (16) and its adjoint into Eq. (22), thus

$$\begin{aligned} \hat{H}^Q = & -\nabla_1 \cdot \left[\sum_{nlm} \sum_{rst} \hat{f}_{nlm}^\dagger \hat{g}_{rst}^\dagger \int u_{c,0}^*(\mathbf{r}) \right. \\ & \times \zeta_{nlm}^{e*}(\mathbf{r}) \vec{\mathbf{Q}}(\mathbf{r}) u_{v,0}(\mathbf{r}) \zeta_{rst}^h(\mathbf{r}) d^3 r \left. \right] \\ & \times \mathbf{E}(\mathbf{r}_1, t) \Big|_{\mathbf{r}_1=0} + \text{h.c.}, \end{aligned} \quad (25)$$

where ‘‘h.c.’’ denotes the Hermitian conjugate. We calculate the integral of Eq. (25) by decomposing it into a sum of integrals over the volume occupied by each of the unit cells. By applying the coordinate transformation $\mathbf{r}' = \mathbf{r} - \mathbf{R}_q$, where \mathbf{R}_q is a translational lattice vector (the lattice remains unchanged when it is translated by \mathbf{R}_q), Eq. (25) becomes

$$\begin{aligned} \hat{H}^Q = & -\nabla_1 \cdot \left[e \sum_{nlm} \sum_{rst} \sum_q \hat{f}_{nlm}^\dagger \hat{g}_{rst}^\dagger \int_{\text{UC}} u_{c,0}^*(\mathbf{r}' + \mathbf{R}_q) \right. \\ & \times \zeta_{nlm}^{e*}(\mathbf{r}' + \mathbf{R}_q) \\ & \times \vec{\mathbf{Q}}(\mathbf{r}' + \mathbf{R}_q) u_{v,0}(\mathbf{r}' + \mathbf{R}_q) \\ & \left. \times \zeta_{rst}^h(\mathbf{r}' + \mathbf{R}_q) d^3 r' \right] \mathbf{E}(\mathbf{r}_1, t) \Big|_{\mathbf{r}_1=0} + \text{h.c.} \end{aligned} \quad (26)$$

Since $u_{i,0}(\mathbf{r}' + \mathbf{R}_q) = u_{i,0}(\mathbf{r}')$ ($i = c, v$), and the functions $\zeta_{nlm}^h(\mathbf{r}' + \mathbf{R}_q)$ and $\zeta_{nlm}^e(\mathbf{r}' + \mathbf{R}_q)$ are practically constant in each unit cell volume, Eq. (26) can be approximated as

$$\begin{aligned} \hat{H}^Q \approx & -\nabla_1 \cdot \left[e \sum_{nlm} \sum_{rst} \sum_q \hat{f}_{nlm}^\dagger \hat{g}_{rst}^\dagger \zeta_{nlm}^{e*}(\mathbf{R}_q) \zeta_{rst}^h(\mathbf{R}_q) \right. \\ & \left. \times \left(\frac{1}{2} \mathbf{R}_q \mathbf{P}_{cv} + \frac{1}{2} \mathbf{P}_{cv} \mathbf{R}_q + \vec{\mathbf{Q}}_{cv} \right) \right] \mathbf{E}(\mathbf{r}_1, t) \Big|_{\mathbf{r}_1=0} + \text{h.c.} \end{aligned} \quad (27)$$

Here \mathbf{P}_{cv} is given by Eq. (20), and $\vec{\mathbf{Q}}_{cv}$ is defined as

$$\vec{\mathbf{Q}}_{cv} = \frac{1}{2V_0} \int_{\text{UC}} u_{c,0}^*(\mathbf{r}') \mathbf{r}' \mathbf{r}' u_{v,0}(\mathbf{r}') d^3 r'. \quad (28)$$

The term containing $\mathbf{R}_q \mathbf{R}_q$ has vanished because of the orthogonality of the Bloch functions, i.e., $\langle u_{i,0} | u_{j,0} \rangle = \hat{\delta}_{ij}$; $j = c, v$. The $\vec{\mathbf{Q}}_{cv}$ vanishes since we are assuming that the valence band is p -like and the conduction band is s -like. Thus, using $\vec{\mathbf{Q}}_{cv} = 0$, and replacing $\sum_q \rightarrow \int dR$, Eq. (27) becomes

$$\begin{aligned} \hat{H}^Q = & -\nabla_1 \cdot \left[e \sum_{nlm} \sum_{rst} \hat{f}_{nlm}^\dagger \hat{g}_{rst}^\dagger \right. \\ & \left. \times \left(\frac{1}{2} \mathbf{P}_{cv} \mathbf{D}_{nmrst} + \frac{1}{2} \mathbf{D}_{nmrst} \mathbf{P}_{cv} \right) \right] \\ & \times \mathbf{E}(\mathbf{r}_1, t) \Big|_{\mathbf{r}_1=0} + \text{h.c.} \end{aligned} \quad (29)$$

Here \mathbf{D}_{nmrst} is defined as

$$\mathbf{D}_{nmrst} \equiv \int \zeta_{nlm}^{e*}(\mathbf{R}) \mathbf{R} \zeta_{rst}^h(\mathbf{R}) d^3 R, \quad (30)$$

with the integration running over the volume of the quantum dot. Equation (29) is the final expression for the electric quadrupole Hamiltonian \hat{H}^Q . The factor \mathbf{D}_{nmrst} depends only on the envelope functions. By using the definition of $\zeta_{nlm}^{e,h}(\mathbf{R})$ given by Eq. (12), \mathbf{D}_{nmrst} becomes

$$\begin{aligned}
 \mathbf{D}_{nmlrst} = & A_{nlrs} B_{lm} B_{st} \left\{ \frac{C_{st}}{2(2l+1)} [\mathbf{n}_x \pm i\mathbf{n}_y] \right. \\
 & \times \left\{ \tilde{\delta}_{(m+1)t} [\tilde{\delta}_{l(s-1)} + \tilde{\delta}_{l(s+1)}] \right. \\
 & + \tilde{\delta}_{(m-1)t} \left[(l-m+1)(l-m+2)\tilde{\delta}_{l(s-1)} \right. \\
 & \left. \left. - (l+m)(l+m-1)\tilde{\delta}_{l(s+1)} \right] \right\} \\
 & + \mathbf{n}_z C_{lm} \tilde{\delta}_{mt} \left[\frac{l+m+1}{2l+3} \tilde{\delta}_{l(s-1)} + \frac{l-m}{2l-1} \tilde{\delta}_{l(s+1)} \right] \left. \right\}, \quad (31)
 \end{aligned}$$

where the coefficients A_{nlrs} , B_{lm} , and C_{lm} are given by

$$A_{nlrs} \equiv 2\pi \int_0^a R^3 \Lambda_{nl}(R) \Lambda_{rs}(R) dR, \quad (32a)$$

$$B_{lm} \equiv \sqrt{\frac{(2l+1)(l-m)!}{4\pi(l+m)!}}, \quad (32b)$$

$$C_{lm} \equiv \frac{2(l+m)!}{(2l+1)(l-m)!}. \quad (32c)$$

2. Electric Quadrupole Selection Rules and Absorption Rate

Using again the Fermi Golden Rule, the electric quadrupole transition rate (α^Q) for photon absorption reads as

$$\alpha^Q = \frac{2\pi}{\hbar} \sum_{nlm} \sum_{rst} \left| \langle nml; rst | \hat{H}_{\text{int}}^Q | 0 \rangle \right|^2 \delta \left[\hbar\omega - (\varepsilon_{nl}^e + \varepsilon_{rs}^h) \right]. \quad (33)$$

Here $|0\rangle$ is the ground state of the quantum dot. By substituting Eq. (29) into Eq. (33), we obtain that the electric quadrupole transition rate

$$\begin{aligned}
 \alpha^Q = & \frac{2\pi}{\hbar} e^2 \\
 & \times \sum_{nlm} \sum_{rst} \left| \nabla_1 \cdot \left(\frac{1}{2} \mathbf{P}_{cv} \mathbf{D}_{nmlrst} + \frac{1}{2} \mathbf{D}_{nmlrst} \mathbf{P}_{cv} \right) \tilde{\mathbf{E}}(\mathbf{r}_1) \Big|_{\mathbf{r}_1=0} \right|^2 \\
 & \times \delta \left[\hbar\omega - (\varepsilon_{nl}^e + \varepsilon_{rs}^h) \right]. \quad (34)
 \end{aligned}$$

We find that the electric quadrupole absorption rate contains the dyadic product of \mathbf{P}_{cv} and \mathbf{D}_{nmlrst} and vice versa. While \mathbf{P}_{cv} depends on the bulk material properties, \mathbf{D}_{nmlrst} depends on the quantum dot properties [see Eqs. (20) and (31)]. This term implies that the allowed electric quadrupole transitions occur when the quantum numbers l, s, m , and t fulfill

$$m-t = \pm 1 \text{ and } l-s = \pm 1$$

or

$$m-t = 0 \text{ and } l-s = \pm 1.$$

These relationships form the selection rules for the electric quadrupole transitions in a semiconductor quantum dot. Figure 91.45 illustrates the first few allowed quadrupole transi-

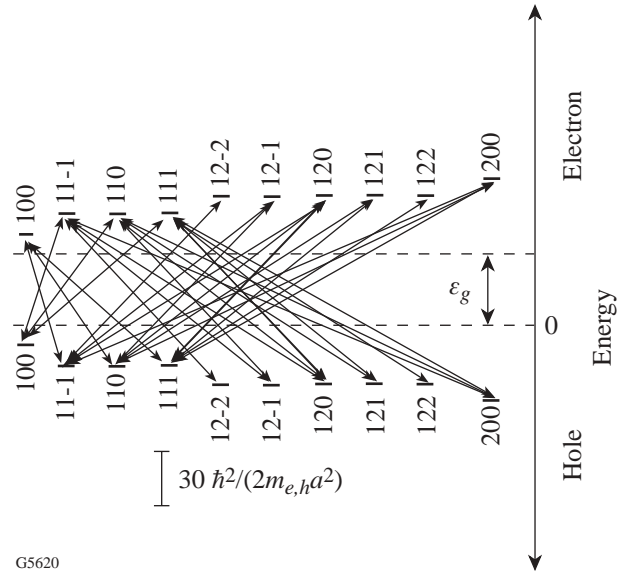


Figure 91.45

Diagram of the allowed electric quadrupole transitions in a spherical quantum dot. The energy levels are labeled by the quantum numbers nlm (electron) and rst (hole). The selection rules are $l-s = \pm 1$ and $(m-t = \pm 1$ or $m-t = 0)$. The allowed electric quadrupole transitions exclude the allowed electric dipole transitions.

tions. We find that the quadrupole selection rules exclude any electric dipole allowed transitions. This allows the electric quadrupole transitions to be spectroscopically separated from electric dipole transitions.

Absorption Rates in Strongly Confined Optical Fields

To compare the electric dipole and electric quadrupole absorption rates in strongly confined optical fields, we consider a quantum dot in the vicinity of a laser-illuminated metal tip. This situation is encountered in so-called “apertureless” schemes of near-field optical microscopy. Strongest light confinement is achieved when the metal tip is irradiated with light polarized along the tip axis. For this situation, Fig. 91.46(a) shows the field distribution ($|\mathbf{E}|^2$) rigorously calculated by the multiple multipole (MMP) method²³ near a gold tip with 10-nm end diameter and irradiated with $\lambda = 800$ -nm light.²⁴ In MMP, electromagnetic fields are represented by a series expansion of known analytical solutions of Maxwell equations. To determine the unknown coefficients in the series expansion, boundary conditions are imposed at discrete points on the interfaces between adjacent homogeneous domains. The calculated field distribution, for our particular geometry, can be well approximated by the field generated by an electric dipole aligned along the tip axis z and located at the origin of tip curvature. Figure 91.46(b) demonstrates the validity of this dipole approximation: the rigorously calculated field strength

($|\mathbf{E}|^2$) for the metal tip is plotted along the z axis (solid line) and compared with the corresponding field generated by the dipole (dashed line).¹⁸ The only adjustable parameter is the dipole moment \mathbf{p}_0 , which can be related to the computationally determined field enhancement factor. Because of this very good approximation, we simply replace the laser-illuminated metal tip by a dipole.

The electric field $\mathbf{E}(\mathbf{r})$ generated by an oscillating electric dipole with moment \mathbf{p}_0 located at \mathbf{r}_0 and oscillating at the angular frequency ω can be represented as

$$\tilde{\mathbf{E}}(\mathbf{r}) = \frac{k_0^2}{\epsilon_0} \vec{\mathbf{G}}(\mathbf{r}, \mathbf{r}_0, \omega) \mathbf{p}_0. \quad (35)$$

Here, $k_0 = \omega/c$ (c being the vacuum speed of light), and $\vec{\mathbf{G}}(\mathbf{r}, \mathbf{r}_0, \omega)$ is the free-space dyadic Green’s function.²⁵ We consider the situation depicted in Fig. 91.47, where a sharp metal tip illuminated with light polarized along the tip axis (z axis) is substituted by a dipole with magnitude p_0 and oriented in the z direction. The dipole is located at $\mathbf{r}_0 = z_0 \mathbf{n}_z$, and the quantum dot coordinates are $\mathbf{r} = x \mathbf{n}_x + y \mathbf{n}_y$. The quantum dot is scanned in the plane $z = 0$, while the position of the exciting dipole is kept fixed.

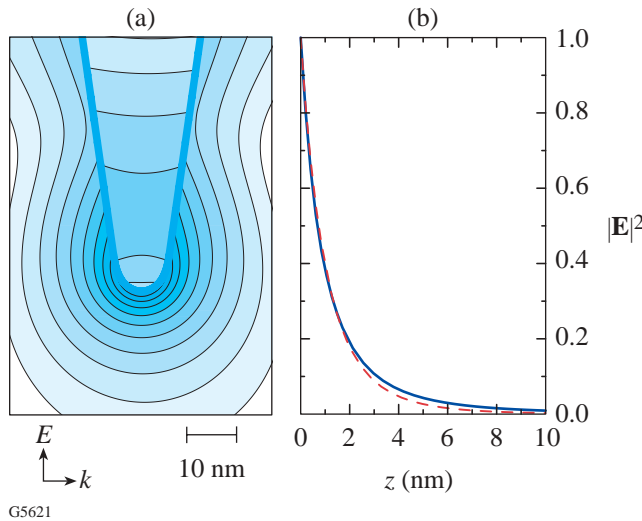


Figure 91.46
(a) Computed field distribution ($|\mathbf{E}|^2$) near a gold tip irradiated by a plane wave polarized along the tip axis. Logarithmic scaling with a factor of 2 between successive contour lines. (b) Comparison of the computed field ($|\mathbf{E}|^2$, solid curve) with the corresponding field of a dipole ($|\mathbf{E}|^2$, dashed curve) oriented along the tip axis and located inside the tip. Both fields are evaluated along the tip axis z with $z = 0$ coinciding with the tip surface.

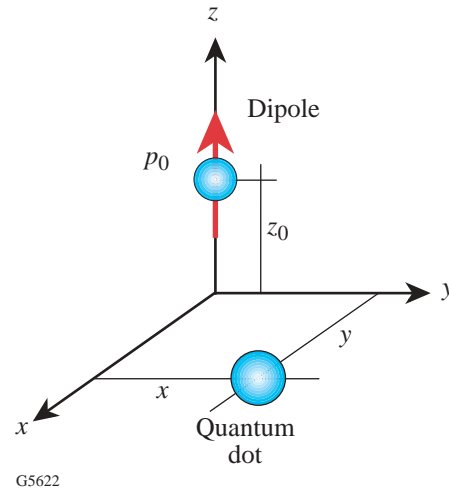


Figure 91.47
Simplified configuration of a quantum dot ($\mathbf{r} = x \mathbf{n}_x + y \mathbf{n}_y$) interacting with a laser-illuminated metal tip. The tip is replaced by a vertical dipole ($\mathbf{r}_0 = z_0 \mathbf{n}_z$) with moment p_0 and oriented along the z axis.

To calculate the electric quadrupole absorption rate (α^Q) and the electric dipole absorption rate (α^E), we consider Bloch functions for the valence band and conduction band that are similar to those of GaAs. If we ignore spin-orbit coupling and spin degeneracy, the p -like valence band is three-fold degenerate. The Bloch functions are calculated by using the empirical pseudopotential method with parameters taken from Ref. 26. GaAs has a lattice constant of $d = 0.565$ nm, and the effective masses of electron and hole are $m_e = 0.067 m_0$ and $m_h = 0.080 m_0$ (light hole), respectively. Inclusion of the heavy hole will only shift the hole energy levels, as long as the heavy-hole Bohr radius is larger than the quantum dot radius.

We consider the lowest-allowed electric dipole transition, i.e., the transition with the lowest-allowed energy difference between initial and final states. During this transition, an electron with quantum numbers (100) and a hole with quantum numbers (100) are created. Since there is *no* preferential coordinate axis, we take the rotational average of Eq. (18). Also, by taking into account the degeneracy of the valence band (three-fold), the averaged electric dipole absorption rate becomes

$$\langle \alpha^E \rangle = \langle K_e \rangle \delta \left[\hbar\omega - (\varepsilon_{10}^e + \varepsilon_{10}^h) \right], \quad (36)$$

where

$$\langle K_e \rangle = \frac{2\pi}{\hbar} e^2 |\tilde{\mathbf{E}}(\mathbf{0})|^2 |\mathbf{P}|^2 \quad (37)$$

and

$$|\mathbf{P}| = |\mathbf{P}_{cv1}| = |\mathbf{P}_{cv2}| = |\mathbf{P}_{cv3}|. \quad (38)$$

By computing numerically the integral of Eq. (20) over a *unit cell* of the crystal, we obtain that $|\mathbf{P}| \approx 0.75 d$.

The lowest-energy-allowed electric quadrupole transition creates a hole with quantum numbers (110), (11-1), or (111) (three-fold degeneracy) and an electron with quantum numbers (100). Again, there is *no* preferential coordinate axis, so the rotational average of Eq. (34) has to be evaluated. Since the electric quadrupole moment is the dyadic product of two vectors with independent orientations, the rotational average of Eq. (34) is obtained in a straightforward manner. After evaluating the average and taking into account the degeneracy

of the valence band and the hole energy level, the averaged electric quadrupole absorption rate becomes

$$\langle \alpha^Q \rangle = \langle K^Q \rangle \delta \left[\hbar\omega - (\varepsilon_{10}^e + \varepsilon_{11}^h) \right]. \quad (39)$$

Here $\langle K^Q \rangle$ corresponds to

$$\langle K^Q \rangle = \frac{2\pi}{\hbar} \frac{e^2}{2} |\mathbf{P}|^2 |\mathbf{D}|^2 \times \sum_{i,j} \left[\left| \frac{\partial}{\partial x_i} \tilde{E}_j(\mathbf{0}) \right|^2 + \frac{\partial}{\partial x_i} \tilde{E}_j(\mathbf{0}) \frac{\partial}{\partial x_j} \tilde{E}_i^*(\mathbf{0}) \right]. \quad (40)$$

The i^{th} Cartesian coordinate is denoted by x_i and $\tilde{E}_i(\mathbf{r})$ is i^{th} Cartesian component of the electric field $\tilde{\mathbf{E}}_i(\mathbf{r})$. $|\mathbf{D}|$ corresponds to

$$|\mathbf{D}| = |\mathbf{D}_{10010}| = |\mathbf{D}_{100111}| = |\mathbf{D}_{10011-1}|. \quad (41)$$

The integration of Eq. (41) over the quantum dot volume renders a value $|\mathbf{D}| \approx 0.3 a$.

Discussion of the Near Field–Quantum Dot Interaction

We analyze absorption rates for quantum dots with the two different radii: $a = 5$ nm and $a = 10$ nm. For $a = 5$ nm, the electric quadrupole transition is excited at a wavelength of $\lambda \approx 500$ nm and the electric dipole transition at $\lambda \approx 550$ nm. On the other hand, the quadrupole transition for a quantum dot of radius $a = 10$ nm occurs at $\lambda \approx 615$ nm and the electric dipole transition at $\lambda \approx 630$ nm.

For a quantum dot that is just beneath the exciting dipole ($\mathbf{r} = \mathbf{0}$), Fig. 91.48 shows the ratio of the quadrupole absorption rate and the dipole absorption rate ($\langle \alpha^Q \rangle / \langle \alpha^E \rangle$) as a function of the normalized separation z_0 / λ . The vertical dashed line indicates the minimum physical distance between quantum dot and the dipole, i.e., the limit at which the tip and quantum dot would touch (we assume a tip radius of 5 nm).

For the quantum dot with radius $a = 5$ nm and an excitation wavelength of $\lambda = 550$ nm, the normalized minimum distance

is $z_0^{\min}/\lambda \approx 0.018$. Similarly, for the quantum dot with radius $a = 10$ nm and a wavelength of $\lambda = 630$ nm, the minimum distance is 15 nm, which corresponds to a normalized distance of $z_0^{\min}/\lambda \approx 0.024$. The important finding is that the ratio ($\langle\alpha^Q\rangle/\langle\alpha^E\rangle$) can be as high as 0.3 for a 5-nm quantum dot [see Fig. 91.48(a)] and even 0.6 for a 10-nm quantum dot [see Fig. 91.48(b)]. These values are roughly three orders of magnitude larger than those obtained by using far-field excitation [for plane wave excitation the ratio is of the order of $(a/\lambda)^2$]. Thus, we find that in the extreme near field ($z_0 < \lambda/10$), quadrupole transitions become important and the electric dipole approximation is not sufficiently accurate!

The plots in Figs. 91.49 and 91.50 are generated by scanning the quantum dot in the x - y plane while keeping the exciting dipole at the constant height z_0 . Figure 91.49 shows the electric dipole absorption rate $\langle\alpha^E\rangle$, whereas Fig. 91.50 shows the

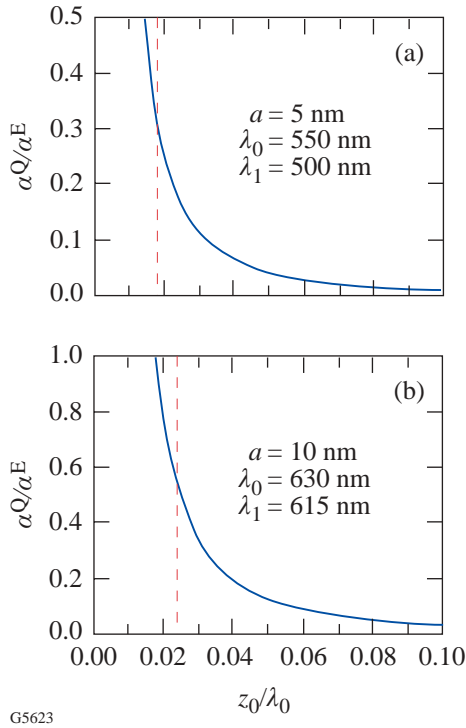


Figure 91.48
Ratio of the electric quadrupole absorption rate $\langle\alpha^Q\rangle$ and the electric dipole absorption rate $\langle\alpha^E\rangle$ as a function of the normalized distance (z_0/λ_0) between excitation dipole ($\mathbf{r}_0 = z_0\mathbf{n}_z$) and quantum dot center ($\mathbf{r} = \mathbf{0}$). The quantum dot radius is $a = 5$ nm in (a) and $a = 10$ nm in (b). The vertical dashed line indicates the minimum physical separation between the center of the quantum dot and the exciting dipole. This separation corresponds to $a_t + a$, where $a_t = 5$ nm is the radius of curvature of the metal tip.

electric quadrupole absorption rate $\langle\alpha^Q\rangle$. Both plots are symmetrical with respect to the z axis. In the case of $\langle\alpha^E\rangle$, this symmetry is generated by the dominant field component \tilde{E}_z , whereas in the case of $\langle\alpha^E\rangle$, the symmetry is due to the strong field gradient $\partial\tilde{E}_z/\partial z$. The electric dipole absorption rate is proportional to the square of the particle dipole moment p_0 and to the square of the lattice constant of the crystal d . On the other hand, the quadrupole absorption rate is also proportional to the square of (a/λ) . This is evident in Fig. 91.50 where the ratio a/λ in Fig. 91.50(b) is twice the ratio a/λ in Fig. 91.50(a). A comparison between the widths of the curves in Figs. 91.49 and 91.50 shows that *no* improvement of spatial resolution can be achieved by selectively probing optical quadrupole transitions!

Conclusions

As was mentioned above, laser-irradiated metal tips are used in near-field optical microscopy as miniature light sources.¹⁷ A strongly enhanced and localized optical field is created at the tip apex if proper polarization conditions are used. Using this technique, spectroscopic measurements with spatial resolutions of only 10 to 20 nm have been demonstrated.¹⁷ To date, this is the highest spatial resolution of any optical spectroscopic measurement. This technique will be

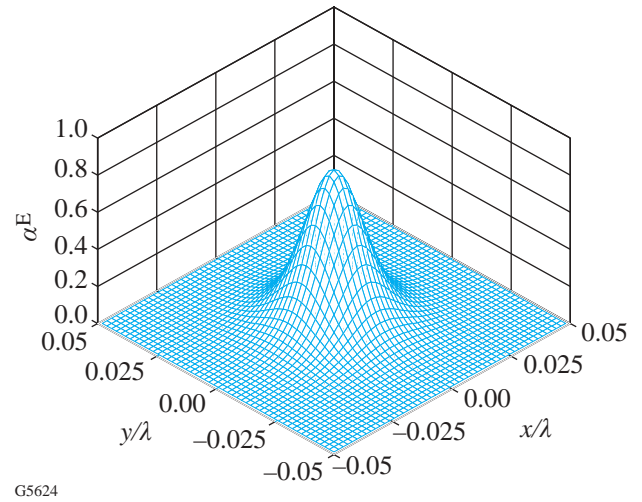


Figure 91.49
Electric dipole absorption rate $\langle\alpha^E\rangle$ as a function of the normalized lateral coordinates ($x/\lambda, y/\lambda$). The height of the excitation dipole is $z_0 = 0.025\lambda$. The vertical axis has units of $(2\pi^2)(edp_0/\epsilon_0)^2 [10^4/(\hbar\lambda^6)] \delta[\hbar\omega - (\epsilon_{10} + \epsilon_{10})]$. The symbols e, d , and p_0 denote the elementary charge, the lattice constant, and the dipole moment, respectively.

applied in our future investigations to experimentally verify the quadrupole transitions predicted in this work. Single CdSe quantum dots will be dispersed on a flat substrate, and the quantum dot luminescence will be recorded as a function of excitation wavelength and tip position.

In this work, higher-order multipole interactions between a semiconductor quantum dot and a strongly confined optical field have been analyzed. Expressions have been derived for the electric quadrupole interaction Hamiltonian, the associated absorption rate, and selection rules. It has been assumed that the quantum dot has a p -like valence band and an s -like conduction band. Also, the Bohr radii of electron and hole were assumed to be larger than the sphere radius (strong confinement limit), and *no* Coulomb interactions between hole and electron have been taken into account. Because of their different selection rules, electric dipole and electric quadrupole interband transitions can be separated and selectively excited. The electric quadrupole absorption strength depends on the bulk properties of the material (Bloch functions) as well as on the envelope functions (confinement functions). This differs from the electric dipole absorption strength, which depends only on the bulk properties of the semiconductor. When the quantum dot with radius a interacts with the confined optical

field produced by a sharply pointed tip, the ratio between the electric quadrupole absorption rate and the electric dipole absorption rate can be as high as 0.3 for $a = 5$ nm and even 0.6 for $a = 10$ nm. Electric quadrupole transitions cannot be ignored in the extreme near field, i.e., for separations between tip and quantum dot smaller than $\lambda/10$. The inclusion of electric quadrupole transitions modifies the absorption spectra of quantum dots in the extreme near field. We have shown, however, that *no* improvement in the spatial resolution can be achieved by selective probing of electric quadrupole transitions. Future studies will be directed at electric quadrupole excitonic interactions.

ACKNOWLEDGMENT

We wish to thank Stephan W. Koch and Andreas Knorr for valuable input to this work. This research was supported by the U.S. Department of Energy through grant DE-FG02-01ER15204 and by the Fulbright-CONACyT Fellowship (JZ-S).

REFERENCES

1. V. I. Klimov *et al.*, *Science* **290**, 314 (2000).
2. G. K. Brennen, I. H. Deutsch, and P. S. Jessen, *Phys. Rev. A, At. Mol. Opt. Phys.* **61**, 062309 (2000).
3. P. Michler *et al.*, *Science* **290**, 2282 (2000).

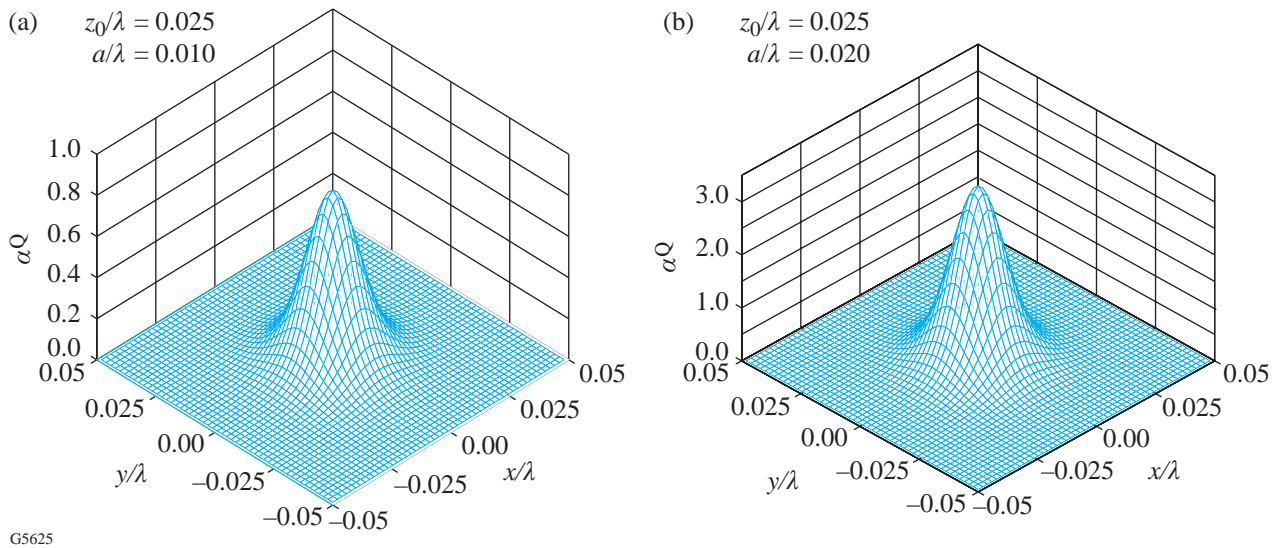


Figure 91.50

Electric dipole absorption rate $\langle \alpha^Q \rangle$ as a function of the normalized lateral coordinates $(x/\lambda, y/\lambda)$. The height of the excitation dipole is $z_0 = 0.025 \lambda$. The symbols e , d , and p_0 denote the elementary charge, the lattice constant, and the dipole moment, respectively. The quantum dot radius is $a = 0.01 \lambda$ in (a) and $a = 0.02 \lambda$ in (b). The width of the curve is roughly the same as in Fig. 91.49, which indicates that no improvement of resolution can be achieved by quadrupole transitions. The vertical axis has units of $(2\pi^5)(edp_0/\epsilon_0)^2 [10^4/(\hbar\lambda^6)] \delta[\hbar\omega - (\epsilon_{10} + \epsilon_{11})]$.

4. For a recent review, see R. C. Dunn, *Chem. Rev.* **99**, 2891 (1999).
5. N. Van Hulst, ed., *J. Microsc.* **202** (1, Pt. 1), 1 (2001).
6. R. D. Grober *et al.*, *Appl. Phys. Lett.* **64**, 1421 (1994).
7. J. Levy *et al.*, *Phys. Rev. Lett.* **76**, 1948 (1996).
8. A. Richter *et al.*, *Ultramicroscopy* **71**, 205 (1998).
9. A. von der Heydt *et al.*, *J. Chem. Phys.* **112**, 7831 (2000).
10. O. Mauritz *et al.*, *Phys. Rev. Lett.* **82**, 847 (1999).
11. A. Knorr, S. W. Koch, and W. W. Chow, *Opt. Commun.* **179**, 167 (2000).
12. B. Hanewinkel *et al.*, *Phys. Rev. B, Condens. Matter* **55**, 13,715 (1997).
13. G. W. Bryant, *Appl. Phys. Lett.* **72**, 768 (1998).
14. A. Chavez-Pirson and S. T. Chu, *Appl. Phys. Lett.* **74**, 1507 (1999).
15. H. F. Hamann *et al.*, *J. Chem. Phys.* **114**, 8596 (2001).
16. Y. C. Martin, H. F. Hamann, and H. K. Wickramasinghe, *J. Appl. Phys.* **89**, 5774 (2001).
17. E. J. Sanchez, L. Novotny, and X. S. Xie, *Phys. Rev. Lett.* **82**, 4014 (1999), and references therein.
18. L. Novotny, in *Near-Field Optics and Surface Plasmon Polaritons, Topics Appl. Phys.*, edited by S. Kawata (Springer-Verlag, Berlin, 2001), Vol. 81, pp. 123–141.
19. R. G. Woolley, *J. Phys. B, At. Mol. Phys.* **6**, L97 (1973).
20. L. D. Barron and C. G. Gray, *J. Phys. A, Math. Gen.* **6**, 59 (1973).
21. H. Haug and S. W. Koch, *Quantum Theory of the Optical and Electronic Properties of Semiconductors*, 2nd ed. (World Scientific, Singapore, 1993).
22. L. Banyai and S. W. Koch, *Semiconductor Quantum Dots*, World Scientific Series on Atomic, Molecular, and Optical Physics, Vol. 2 (World Scientific, Singapore, 1993).
23. C. Hafner, *The Generalized Multipole Technique for Computational Electromagnetics* (Artech House, Boston, 1990).
24. L. Novotny, R. X. Bian, and X. S. Xie, *Phys. Rev. Lett.* **79**, 645 (1997).
25. C. Tai, *Dyadic Green Functions in Electromagnetic Theory*, 2nd ed., IEEE Press Series on Electromagnetic Waves (IEEE Press, Piscataway, NJ, 1994).
26. P. Y. Yu and M. Cardona, *Fundamentals of Semiconductors: Physics and Materials Properties*, 1st ed., corr. print (Springer, Berlin, 1996).

Publications and Conference Presentations

Publications

- R. Betti, K. Anderson, V. N. Goncharov, R. L. McCrory, D. D. Meyerhofer, S. Skupsky, and R. P. J. Town, "Deceleration Phase of Inertial Confinement Fusion Implosions," *Phys. Plasmas* **9**, 2277 (2002).
- W. R. Donaldson, R. Boni, R. L. Keck, and P. A. Jaanimagi, "A Self-Calibrating, Multichannel Streak Camera for Inertial Confinement Fusion Applications," *Rev. Sci. Instrum.* **73**, 2606 (2002).
- L. T. Hudson, A. Hennis, R. D. Deslattes, J. F. Seely, G. E. Holland, R. Atkin, L. Marlin, D. D. Meyerhofer, and C. Stoeckl, "A High-Energy X-Ray Spectrometer Diagnostic for the OMEGA Laser," *Rev. Sci. Instrum.* **73**, 2270 (2002).
- R. L. Keck, W. R. Donaldson, V. Yu. Glebov, P. A. Jaanimagi, F. J. Marshall, P. W. McKenty, D. D. Meyerhofer, S. P. Regan, W. Seka, C. Stoeckl, and R. Boni, "Laser and X-Ray Irradiation Diagnostics That Have Paved the Path to Significantly Improved ICF Target Performance," in *Advanced Diagnostics for Magnetic and Inertial Fusion*, edited by P. E. Stott, A. Wootton, G. Gorini, E. Sindoni, and D. Batani (Kluwer Academic/Plenum Publishers, New York, 2002), pp. 181–188.
- S. V. Lebedev, J. P. Chittenden, F. N. Beg, S. N. Bland, A. Ciardi, D. Ampleford, S. Hughes, M. G. Haines, A. Frank, E. G. Blackman, and T. Gardiner, "Laboratory Astrophysics and Collimated Stellar Outflows: The Production of Radiatively Cooled Hypersonic Plasma Jets," *Astrophys. J.* **564**, 113 (2002).
- A. V. Okishev, D. Battaglia, I. Begishev, and J. D. Zuegel, "Highly Stable, Diode-Pumped, Cavity-Dumped Nd:YLF Regenerative Amplifier for the OMEGA Laser Fusion Facility," in *OSA TOPS Vol. 68, Advanced Solid-State Lasers*, edited by M. E. Fermann and L. R. Marshall (Optical Society of America, Washington, DC, 2002), pp. 418–422.
- A. V. Okishev, M. D. Skeldon, R. L. Keck, and W. Seka, "A New High-Bandwidth, All-Solid-State Pulse-Shaping System for the OMEGA Laser Facility," in *Laser Optics 2000: Ultrafast Optics and Superstrong Laser Fields*, edited by A. A. Andreev and V. E. Yashin (SPIE, Bellingham, WA, 2001), pp. 69–73.
- S. Papernov, A. W. Schmid, R. Krishnan, and L. Tsybeskov, "Using Colloidal Gold Nanoparticles for Studies of Laser Interaction with Defects in Thin Films," in *Laser-Induced Damage in Optical Materials: 2000*, edited by G. J. Exarhos, A. H. Guenther, M. R. Kozlowski, K. L. Lewis, and M. J. Soileau (SPIE, Bellingham, WA, 2001), pp. 146–154.
- P. B. Radha, J. A. Delettrez, R. Epstein, V. Yu. Glebov, R. L. Keck, R. L. McCrory, P. W. McKenty, D. D. Meyerhofer, F. J. Marshall, S. P. Regan, S. Roberts, T. C. Sangster, W. Seka, S. Skupsky, V. A. Smalyuk, C. Sorce, C. Stoeckl, J. M. Soures, R. P. J. Town, B. Yaakobi, J. A. Frenje, C. K. Li, R. D. Petrasso, F. H. Séguin, K. Fletcher, S. Padalino, C. Freeman, N. Izumi, R. A. Lerche, and T. W. Phillips, "Inference of Mix in Direct-Drive Implosions on OMEGA," *Phys. Plasmas* **9**, 2208 (2002) (invited).
- S. P. Regan, J. A. Delettrez, R. Epstein, P. A. Jaanimagi, B. Yaakobi, V. A. Smalyuk, F. J. Marshall, D. D. Meyerhofer, W. Seka, D. A. Haynes, Jr., I. E. Golovkin, and C. F. Hooper, Jr., "Characterization of Direct-Drive-Implosion Core Conditions on OMEGA with Time-Resolved Ar *K*-Shell Spectroscopy," *Phys. Plasmas* **9**, 1357 (2002).
- F. H. Séguin, C. K. Li, J. A. Frenje, D. G. Hicks, K. M. Green, S. Kurebayashi, R. D. Petrasso, J. M. Soures, D. D. Meyerhofer, V. Yu. Glebov, P. B. Radha, C. Stoeckl, S. Roberts, C. Sorce, T. C. Sangster, M. D. Cable, K. A. Fletcher, and S. Padalino, "Using Secondary-Proton Spectra to Study the Compression and Symmetry of Deuterium-Filled Targets at OMEGA," *Phys. Plasmas* **9**, 2725 (2002).

W. Seka, R. S. Craxton, R. L. Keck, J. P. Knauer, D. D. Meyerhofer, S. P. Regan, C. Stoeckl, B. Yaakobi, R. E. Bahr, D. Montgomery, H. Baldis, and R. Kirkwood, "Laser-Plasma Interaction Diagnostics for ICF Fusion Research," in *Advanced Diagnostics for Magnetic and Inertial Fusion*, edited by P. E. Stott, A. Wootton, G. Gorini, E. Sindoni, and D. Batani (Kluwer Academic/Plenum Publishers, New York, 2002), pp. 27–30.

A. D. Semenov, G. N. Gol'tsman, and R. Sobolewski, "Hot-Electron Effect in Superconductors and Its Applications for Radiation Sensors," *Supercond. Sci. Technol.* **15**, R1 (2002).

S. Skupsky, R. L. McCrory, R. E. Bahr, T. R. Boehly, T. J. B. Collins, R. S. Craxton, J. A. Delettrez, W. R. Donaldson, R. Epstein, V. N. Goncharov, R. Q. Gram, D. R. Harding, P. A. Jaanimagi, R. L. Keck, J. P. Knauer, S. J. Loucks, F. J. Marshall, P. W. McKenty, D. D. Meyerhofer, S. F. B. Morse, O. V. Gotchev, P. B. Radha, S. P. Regan, W. Seka, V. A. Smalyuk, J. M. Soures, C. Stoeckl, R. P. J. Town, M. D. Wittman, B. Yaakobi, J. D. Zuegel, R. D. Petrasso, J. A. Frenje, D. G. Hicks, C. K. Li, and F. H. Séguin, "OMEGA Experiments and Preparation for Direct-Drive Ignition on NIF," in *ECLIM 2000: 26th European Conference on Laser Interaction with Matter*, edited by M. Kálal, K. Rohlena, and M. Sinor (SPIE, Bellingham, WA, 2001), Vol. 4424, pp. 27–36.

V. A. Smalyuk, J. A. Delettrez, V. N. Goncharov, F. J. Marshall, D. D. Meyerhofer, S. P. Regan, T. C. Sangster, R. P. J. Town, and B. Yaakobi, "Rayleigh-Taylor Instability in the Deceleration Phase of Spherical Implosion Experiments," *Phys. Plasmas* **9**, 2738 (2002).

C. Stoeckl, C. Chiritescu, J. A. Delettrez, R. Epstein, V. Yu. Glebov, D. R. Harding, R. L. Keck, S. J. Loucks, L. D. Lund, R. L. McCrory, P. W. McKenty, F. J. Marshall, D. D. Meyerhofer, S. F. B. Morse, S. P. Regan, P. B. Radha, S. Roberts, T. C. Sangster, W. Seka, S. Skupsky, V. A. Smalyuk, C. Sorce, J. M. Soures, R. P. J. Town, J. A. Frenje, C. K. Li, R. D. Petrasso, F. H. Séguin, K. Fletcher, S. Padalino, C. Freeman, N. Izumi, R. A. Lerche, and T. W. Phillips, "First Results from Cryogenic-Target Implosions on OMEGA," *Phys. Plasmas* **9**, 2195 (2002) (invited).

C. Stoeckl, J. A. Delettrez, R. Epstein, V. Yu. Glebov, R. L. Keck, R. L. McCrory, P. W. McKenty, F. J. Marshall, D. D. Meyerhofer, P. B. Radha, S. P. Regan, S. Roberts, W. Seka, S. Skupsky, V. A. Smalyuk, C. Sorce, J. M. Soures, R. P. J. Town, B. Yaakobi, J. A. Frenje, C. K. Li, R. D. Petrasso, F. H. Séguin, K. Fletcher, S. Padalino, C. Freeman, N. Izumi, R. Lerche, T. W. Phillips, and T. C. Sangster, "Core Performance and Mix in Direct-Drive Spherical Implosions on OMEGA," in *Advanced Diagnostics for Magnetic and Inertial Fusion*, edited by P. E. Stott, A. Wootton, G. Gorini, E. Sindoni, and D. Batani (Kluwer Academic/Plenum Publishers, New York, 2002), pp. 19–26.

F.-Y. Tsai, E. L. Alfonso, S. H. Chen, D. R. Harding, and T. N. Blanton, "Effects of Processing Conditions on the Quality and Properties of Vapor-Deposited Polyimide Shells," *Fusion Sci. Technol.* **41**, 178 (2002).

A. Verevkin, J. Zhang, R. Sobolewski, A. Lipatov, O. Okunev, G. Chulkova, A. Korneev, K. Smirnov, and G. N. Gol'tsman, "Detection Efficiency of Large-Active-Area NbN Single-Photon Superconducting Detectors in the Ultraviolet in Near-Infrared Range," *Appl. Phys. Lett.* **80**, 4687 (2002).

Forthcoming Publications

A. Babushkin, M. J. Harvey, and M. D. Skeldon, "The Output Signal-to-Noise Ratio of a Nd:YLF Regenerative Amplifier," to be published in *Applied Optics*.

T. R. Boehly, T. J. B. Collins, O. Gotchev, T. J. Kessler, J. P. Knauer, T. C. Sangster, and D. D. Meyerhofer, "Observations of Modulated Shock Waves in Solid Targets Driven by Spatially Modulated Laser Beams," to be published in the *Journal of Applied Physics*.

H. Brunnader, W. T. Shmayda, D. R. Harding, L. D. Lund, and R. Janezic, "Advanced Tritium Recovery System," to be published in *Fusion Science and Technology*.

Y. Cao, H. Li, J. A. Szpunur and W. T. Shmayda, "Effects of Textures on Hydrogen Diffusion in Nickel," to be published in *Materials Science Forum*.

R. Epstein, J. A. Delettrez, V. Yu. Glebov, V. N. Goncharov, P. W. McKenty, P. B. Radha, S. Skupsky, V. A. Smalyuk, and C. Stoeckl, "One-Dimensional Simulation of the Effects of Unstable Mix on Neutron and Charged-Particle Yield from Laser-Driven Implosion Experiments," to be published in *Lasers and Particle Beams*.

S. D. Jacobs and L. L. Gregg, "Making Waves with the Optics Suitcase," to be published in *Optics and Photonics News*.

T. Z. Kosc, K. L. Marshall, S. D. Jacobs, J. C. Lambropoulos, and S. Faris, "Electric-Field-Induced Motion of Polymer Cholesteric Liquid Crystal Flakes in a Moderately Conductive Fluid," to be published in *Applied Optics*.

M. V. Kozlov and C. J. McKinstrie, "Sound Waves in One-Ion Plasmas," to be published in *Physics of Plasmas*.

M. V. Kozlov and C. J. McKinstrie, "Sound Waves in Two-Ion Plasmas," to be published in *Physics of Plasmas*.

P. Kús, A. Plecenik, L. Satrapinsky, Y. Xu, and R. Sobolewski, "Superconducting Properties of MgB₂ Thin Films Prepared on Flexible Substrates," to be published in *Applied Physics Letters*.

J. A. Marozas and J. D. Zuegel, "The Smoothing Performance of Ultrafast Pickets on the NIF," to be published in the *Journal of the Optical Society of America B*.

S. Papernov and A. W. Schmid, "Correlations Between Embedded Single Gold Nanoparticles in SiO₂ Thin Film and Nanoscale Crater Formation Induced by Pulsed-Laser Radiation," to be published in the *Journal of Applied Physics*.

S. P. Regan, J. A. Delettrez, F. J. Marshall, J. M. Soures, V. A. Smalyuk, B. Yaakobi, V. Yu. Glebov, P. A. Jaanimagi, D. D. Meyerhofer, P. B. Radha, W. Seka, S. Skupsky, C. Stoeckl, R. P. J. Town, D. A. Haynes, Jr., C. F. Hooper, Jr., C. K. Li, R. D. Petrasso, and F. H. Séguin, "Shell Mix in Compressed Core of Spherical Implosion," to be published in *Physical Review Letters*.

F. H. Séguin, C. K. Li, J. A. Frenje, S. Kurebayashi, R. D. Petrasso, F. J. Marshall, D. D. Meyerhofer, J. M. Soures, T. C. Sangster, C. Stoeckl, J. A. Delettrez, P. B. Radha, V. A. Smalyuk, and S. Roberts, "Measurements of ρR Asymmetries at Burn Time in Inertial Confinement Fusion Capsules," to be published in *Physics of Plasmas*.

C. R. Shmayda, W. T. Shmayda, and N. P. Kherani, "Monitoring Tritium Activity on Surfaces: Recent Developments," to be published in *Fusion Science and Technology*.

W. T. Shmayda, A. Bruggeman, J. Braet, and S. Vanderbiesen, "Treatment of Tritiated Solvents," to be published in *Fusion Science and Technology*.

W. T. Shmayda and R. D. Gallagher, "Recovery of Tritium from Pharmaceutical Mixed Waste Liquids," to be published in *Fusion Science and Technology*.

W. T. Shmayda, S. Zukotynski, D. Yeghikyan, and F. Gaspari, "Properties of Amorphous Carbon Films," to be published in *Fusion Science and Technology*.

R. W. Short and A. Simon, "Damping of Perturbations in Weakly Collisional Plasmas," to be published in *Physics of Plasmas*.

M. D. Skeldon, "An Optical-Pulse-Shaping System Based on an Electro-Optic Modulator Driven by an Aperture-Coupled-Stripline Electrical-Waveform Generator," to be published in the *Journal of the Optical Society of America B*.

C. Stoeckl, V. Yu. Glebov, J. D. Zuegel, and D. D. Meyerhofer, "Wide-Dynamic-Range 'Neutron Bang Time' Detector on OMEGA," to be published in the *Review of Scientific Instruments*.

A. Sunahara, J. A. Delettrez, C. Stoeckl, R. W. Short, and S. Skupsky, "Time-Dependent Electron-Thermal-Flux Inhibition in Direct-Drive Laser Implosion," to be published in *Physical Review Letters*.

R. P. J. Town, V. N. Goncharov, P. W. McKenty, J. A. Delettrez, R. Epstein, R. L. McCrory, P. B. Radha, S. Skupsky, V. Yu. Glebov, D. R. Harding, D. D. Meyerhofer, F. J. Marshall, S. P. Regan, W. Seka, V. A. Smalyuk, C. Stoeckl, J. M. Soures, B. Yaakobi, and J. D. Zuegel, "OMEGA Direct-Drive Cryogenic Target Physics," to be published in the proceedings of the 2nd International Conference on Inertial Fusion Sciences and Applications.

L. J. Waxer, J. H. Kelly, J. Rothenberg, A. Babushkin, C. Bibeau, A. Bayramian, and S. Payne, "Precision Spectral Sculpting for Narrowband Amplification of Broadband FM Pulses," to be published in *Optics Letters*.

B. Yaakobi, F. J. Marshall, T. R. Boehly, R. P. J. Town, and D. D. Meyerhofer, "EXAFS Experiments Using a Laser-Imploded Target as a Radiation Source," to be published in the *Journal of the Optical Society of America B*.

J. D. Zuegel and S. A. Letzring, "Bulk Microwave Phase Modulators for Smoothing by Spectral Dispersion," to be published in *Applied Optics*.

Conference Presentations

J. D. Kilkenny, R. L. McCrory, D. D. Meyerhofer, S. F. B. Morse, J. H. Kelly, T. J. Kessler, S. J. Loucks, P. W. McKenty, C. Stoeckl, R. P. J. Town, L. J. Waxer, and J. D. Zuegel, "OMEGA EP: Extended-Performance Capability for the OMEGA Laser System, Including Short-Pulse Capability," Workshop on Ultra-High Field Laser Physics, Chilton, Oxford, 10–12 April 2002.

The following presentations were made at the 2002 International Sherwood Fusion Theory Conference, Rochester, NY, 22–24 April 2002:

T. Gardiner and R. Betti, "Magnetohydrodynamic Equilibria with Pedestals Induced by Poloidal Flow."

L. Guazzotto and R. Betti, "Stabilization of the Resistive Wall Mode by Differentially Rotating Walls in a High- β Tokamak."

D. D. Meyerhofer, "Direct-Drive Inertial Confinement Fusion Research: Theory and Experiments."

R. W. Short, "Linear Undamped Waves in Near-Maxwellian Plasmas with Applications to Stimulated Raman Scattering in Laser-Produced Plasmas."

The following presentations were made at the CLEO/QELS 2002, Long Beach, CA, 19–24 May 2002:

S. G. Lukishova, R. W. Boyd, N. Lepeshkin, R. S. Bennik, and K. L. Marshall, "Feedback-Free Kaleidoscope of Patterns from Nanosecond Laser-Irradiated Nematic Liquid."

A. V. Okishev, D. Battaglia, I. Begishev, and J. Zuegel, "All Solid-State Diode-Pumped Regenerative Amplifier for the OMEGA Laser System."

L. J. Waxer, J. H. Kelly, J. A. Marozas, A. Babushkin, J. Rothenburg, C. Bibeau, A. Bayramian, R. Beach, and S. Payne, "Precision Spectral Shaping Applied to FM Pulses."

T. R. Boehly, T. J. B. Collins, D. D. Meyerhofer, D. K. Bradley, R. Cauble, P. M. Celliers, C. W. Collins, S. G. Glendinning, and D. G. Hicks, "Measurements of the Equation of State of Carbon Foams," International Conference on Warm, Dense Matter, Hamburg, Germany, 3–5 June 2002 (invited).

J. Li, W. R. Donaldson, and T. Y. Hsiang, "Packaging for a High-Speed Interdigitated GaN UV Photodetector," The 8th International Conference on Electronic Materials, IUMRS-ICEM2002, Xi'an, China, 10–14 June 2002.

S. G. Lukishova, R. W. Boyd, N. Lepeshkin, R. S. Bennink, and K. L. Marshall, "Feedback-Free Hexagon Pattern Formation with Nematic Liquid Crystals," IQEC 2002 International Quantum Electronics Conference, Moscow, Russia, 22–28 June 2002.

UNIVERSITY OF
ROCHESTER